Electron-initiated chemistry in polyatomic molecules

by

S. Tonzani

Laurea in Chemistry, Universita' di Perugia, Italy, 2001

A thesis submitted to the

Faculty of the Graduate School of the

University of Colorado in partial fulfillment

of the requirements for the degree of

Doctor of Philosophy

Chemical Physics

2006

This thesis entitled:
Electron-initiated chemistry in polyatomic molecules
written by S. Tonzani
has been approved for the program in Chemical Physics

_____

Chris H. Greene

_____

Robert Parson

Date _____

The final copy of this thesis has been examined by the signatories, and we find that
both the content and the form meet acceptable presentation standards of scholarly
work in the above mentioned discipline.

Tonzani, S. (Ph.D., Chemical Physics)

Electron-initiated chemistry in polyatomic molecules

Thesis directed by Prof. Chris H. Greene

We develop techniques to describe theoretically the process of electron collision with a polyatomic molecule and the interplay of many degrees of freedom in the evolution of the complex. In particular, we characterize resonant processes involving large molecules, believed to be important in radiation damage to nucleic acids. We also examine the electronic resonances in the DNA and RNA bases, and in the backbone constituents. Dissociative recombination reactions, in which a polyatomic ion recombines with an electron and quickly dissociates, are also considered. We elaborate a framework to describe the reaction mechanism and the role of the Rydberg states in the recombination, show results for HCO^+ and compare them with experimental data in order to resolve some of the existing controversies for this reaction.

Acknowledgements

The research work presented here is the result of a few years of my time, but also of the collaboration and efforts of many other people. I would like to acknowledge first of all my advisor Chris Greene, whom besides being a great scientist is a great person, and has been able to deal with me also at the beginning when I produced graphs very sparingly. He is also one of the few physicists I know that is not repelled by molecules of more than two atoms. Thanks also to Steve Leone for pointing me, when I arrived at JILA and I was TAing for him, towards Chris' group.

Throughout these years I have collaborated successfully with many people. I would like to thank in particular Robin Santra, from whom I learned a great deal about quantum chemistry and a lot of other stuff during his stay at JILA. Also my collaborators in the dissociative recombination project: Åsa Larson, Viatcheslav Kokoouline and Roman Čurik. I would also like to thank Åsa for my visit to Stockholm and Slava for my stay in Orlando. I would like to thank Jonathan Tennyson and his group in London for my visit there to learn the R-matrix code, and in general for useful discussions. Also I acknowledge the collaboration and discussions with Leon Sanche and Laurent Caron at the University of Sherbrooke and discussions with Paul Burrow. An advantage of working in the Greene group is the variety of science that I came in contact with, and I would like to thank all the other group members that have been here during my stay. A special thanks goes to some of my best friends during these years: Daniele Bortolotti and Josh Dunn, that besides being great for partying with, have also helped me innumerable

times with my work and to understand science beyond my area of expertise. Thanks also to Alessandro Volpi who showed me where JILA and Boulder were on the world map. Thanks also to all the people at JILA and in particular Peter Ruprecht without whom the computational work would have been a lot slower.

All of this would not have been possible without my family, it is hard to be half a world away from them. And thanks to Jennie who, among all the very good stuff these years in Colorado have brought me, is the very best.

Contents

Chapter

Tables

Table

Figures

Figure

Chapter 1

Introduction

It is an exciting time to work in the field of electronic collisions. This area of research has undergone a major change over the last ten years, mainly due to experimental breakthroughs that have opened the field to the exploration of complex chemical processes, both in the gas phase and in condensed phases. Electron-driven processes are in fact fundamental in many areas, from radiation damage to living tissue [24], to plasma etching and processing of semiconductors, lighting applications (and plasma TVs), scanning tunneling microscope (STM) [171] induced chemistry, chemistry of the atmosphere and interstellar clouds [125].

As it is possible to see, many of these processes are quite far from an electronic collision with a simple molecule in the gas phase, since they happen in complex environments like plasmas or condensed phases or biological cell environments. Nevertheless, the electron-molecule interaction drives all of them and its understanding is absolutely fundamental to developing a correct description of the process.

Traditionally the electron collision community has focused its efforts on an extremely narrow slice of this pie, that is to say gas phase processes involving small molecules (many diatomics) or atoms. Now, these are still interesting processes, but the wealth of possibilities that are rapidly opening up call for a broader spectrum of

investigation, and we will try to undertake this effort from a theory standpoint for a few of the areas cited above.

For the understanding of complex processes it is, again, fundamental to have the support of a theoretical description that can do what experiment often cannot, namely separate different contributions and find out which is the most important, in other words figuring out the mechanism. Unfortunately, this is a very hard task, in the sense that performing calculations involving continua interacting with large molecules is very much at the cutting-edge both of current theoretical approaches and of computational power. Moreover, the numerous advances in the very closely related field of quantum chemistry that deals with bound states, are very slowly being implemented in this field. In other words, there is not yet a "continuum Gaussian", referring to the famous suite [150] of *ab initio* quantum chemistry programs for bound states. Some groups, however, are expending significant effort in this direction, see Refs. [126, 136, 149, 206]. Since there is no "silver bullet", in most cases targeted approaches have to be applied to get the main physics of the process, even if they are somewhat coarse grained.

An entirely different set of problems is presented by the interaction of the metastable electron-molecule complex with its surrounding environment, in particular solvents (see Ref. [55] for a review on electron-initiated chemistry in water) and matrices in condensed environments and solids. In cluster environments (see for example studies of electron attachment to CO_2 clusters recently carried out [46, 177]) the continuum electron interaction with the solvent could also lead to interesting cage effects for the electrons as it happens for molecules [197]. This can lead to a vast array of effects (negative ion stabilization, resonant interactions, fast energy transfers) whose exploration has just started.

The experimental advances that have made possible the exploration of these new exciting areas of research are deserving of some comment. In the text we will talk frequently about storage ring experiments, see Ref. [105] for example, which allow the study of collisions between electrons and charged molecules in a controlled environment, and at very high energy resolution. These will be referred to in the dissociative recombination part of this thesis. Also thin film techniques [24] have allowed the study of processes that occur in condensed phase, often coupled with the precision and control that is possible using an STM (scanning tunneling microscopy) [171] to study processes at the atomic scale. In dissociative processes, COLTRIMS (cold target recoil ion momentum spectroscopy) and other momentum imaging techniques [103] have provided a more detailed picture of the Coulomb breakup of a system. The new and rapidly evolving field of high harmonic generation (HHG) from molecules and more generally the topic of ultrafast intense laser pulses that interact with molecules, have led to new techniques (like "orbital imaging" [86]) and the intriguing possibility of following the electronic dynamics (say, in a chemical reaction) as the nuclei move in a pump-probe experiment [13]. Molecular electronics is another fascinating subject of topical interest, where techniques used in electron scattering theory can be applied [38].

Many processes are possible, both during and after the period when an electron interacts with a molecule, and it is not possible to offer a comprehensive treatment of all of them. We will concentrate mainly on gas phase processes, even though many of our results will have relations to condensed phase experimental results. In the gas phase an electronic collision can produce elastic and inelastic scattering, vibrational or rotational excitation, and then dissociation (processes of dissociative attachment or recombination, depending on whether the target is a neutral or an ion), electron-impact ionization (so-

called e-2e processes), and energy transfers between different degrees of freedom which are extremely effective because unencumbered by selection rules as in photoabsorption. For example it is possible through electronic collisions to activate species that are not reactive as singlets but will be highly reactive in a triplet state. It is also possible to reach many dissociative states, giving these collisions a great energy efficiency in transferring energy to other degrees of freedom of the molecule, such as vibrations, also considering that the colliding electron is indistinguishable from the target electrons and thus will strongly couple to them.

We will focus here on some of these processes; our final goal is to treat electron scattering from a general polyatomic molecule and to describe processes that so far theory has not been able to tackle. Ch. 2 starts with a general introduction to electron scattering theory and illustrates the approximations contained in our methods [191, 192] and the other techniques by which we treat electronic dynamics. Then we will apply this description to many systems in Ch. 4 to test its capabilities and we will show its predictive power [192]. In particular we will then concentrate on the role of electronic resonances in radiation damage to nucleic acids in Ch. 5. This problem is important in view of its medical applications and it has raised a great deal of interest among both theorists [17] and experimentalists [2, 66, 152, 164]. Many groups around the world are working on explaining how low energy electrons below the DNA ionization threshold can lead to one or more strand breaks in the double helix structure of the nucleic acid, with obvious nefarious consequences such as mutations. We will try to give some contribution to this effort. Some of the material in Chapters 2 and 4 has been published in Ref. [192], whereas the majority of the material in Ch. 5 has been published in Refs. [194, 195] Another part of this thesis deals with dissociative recombination processes,

important in the description of the chemistry of interstellar clouds and in the elaboration of star formation models (see Ref. [125] and references therein). We will formulate our theoretical description in Ch. 3 and discuss corresponding results in Ch. 6 for the HCO^+ ion, which we have chosen for its abundance in interstellar clouds. Recombination of polyatomic ions is a very complicated process to treat since it involves a coupling of many electronic and vibrational degrees of freedom, and, since ions are involved as target states, the treatment of an infinite number of neutral molecule Rydberg states. Few such calculations have been performed to date, and we will show how our results [104, 130] compare with experiments in merged beams [144] and storage rings [56]. Rydberg states are highly excited states of atoms or molecules, in which the external electron roams far from the core and it looks a lot like a continuum electron, we will examine techniques to deal with the dynamics of these states such as quantum defect theory (QDT). We will show how Rydberg states can be important and even determinant in some DR reactions. We will also talk about symmetry-distortion effects such as Jahn-Teller [9] and Renner-Teller [155], vibronic couplings and conical intersections, and how they can provide a preferential pathway to fast dissociation. Some of the material in Chapters 3 and 6 has been published in Refs. [104, 130].

We will also consider, whenever possible, the outlook on new processes, the possible continuation of this work and the application of the techniques we developed here to look at a variety of processes in clusters, strong laser field, and more complex biological environments.

Atomic units (see Ref. [181]) will be used throughout this thesis, except where otherwise specified.

Chapter 2

Methods: Electron scattering

This chapter describes all the methods we use to tackle the electronic dynamics of a molecular system plus an external interacting electron. After a brief general introduction to electron-molecule scattering theory, Sec. 2.2 describes an electron scattering approach that will be applied to large molecular systems like the DNA bases in Ch. 5 and all the approximations that are contained in this framework. The following sections describe the methods we have employed for dealing with small molecules, also taking into account their vibrational degrees of freedom, like *ab initio* quantum chemistry calculations (Sec. 2.4.1) for Rydberg states and the R-matrix UK code of Sec. 2.4.2. Finally a brief account of quantum defect theory (QDT) ideas that have been used to treat the long-range dynamics of the electron-molecule interaction problem will be shown in Sec. 2.5, and the treatment of the electrostatic multipolar interaction at long range by various methods will be described.

2.1   Scattering theory

The interaction of an electron with a polyatomic molecule is modeled by the full Hamiltonian of the compound system:

$$\hat{H} = -\frac{1}{2}\sum_i \vec{\nabla}^2_{r_i} - \frac{1}{2}\sum_\alpha \frac{\vec{\nabla}^2_{R_\alpha}}{M_\alpha} - \sum_{i,\alpha} \frac{Z_\alpha}{\mid \vec{r}_i - \vec{R}_\alpha \mid} + \sum_{\alpha>\beta} \frac{Z_\alpha Z_\beta}{\mid \vec{R}_\alpha - \vec{R}_\beta \mid} + \sum_{j>l} \frac{1}{\mid \vec{r}_j - \vec{r}_l \mid}. \quad (2.1)$$

This operator contains both the nuclear and electronic degrees of freedom, indicated respectively with Greek and Latin indices. We will indicate in the following as "target" electrons the N bound electrons present in the molecule or molecular ion, while the scattered electron will be added to form an $N+1$ electrons compound system. Here we deal with the electronic problem alone, within the Born-Oppenheimer (BO) approximation, namely freezing the nuclei in some definite configuration (usually the equilibrium configuration) while solving for the electronic wavefunction. The treatment of vibrations can be carried out by repeating the electronic calculations for different values of the nuclear positions, followed by vibrational averaging or a vibrational frame transformation description. [47, 77]. Vibrational dynamics will be considered in more detail in Chapters 3 and 6 where we will show also how to include non-BO effects [95, 104].

In principle, even considering just the electronic degrees of freedom the problem is still a very complicated many-body interaction. The scattered electron is indistinguishable from the target electrons inside the molecule and it can in principle electronically excite the molecule. For this reason different approximations will be required to make the description of different processes feasible.

The final wavefunction of the system will have to obey scattering boundary conditions for the escaping electron, therefore at large distance from the molecule it should look like an incident plane wave plus a spherical scattered wave, in order to be able

to apply the usual formulas to calculate cross sections and scattering amplitudes, as described in many quantum mechanics textbooks, see for example Ref. [165]. This can be done by matching to a long-range analytical form, as we will see in Sec. 2.5.

At this point a comparison of the electron collision problem and the more traditional bound state problem is opportune. The continuum problem is more complicated because of the scattering boundary conditions that have to be imposed on the wavefunctions, but in principle the two are very similar many body problems. The quantum chemistry community has made tremendous advances in the past 20 years (coupled cluster theory, DFT, linear scaling methods and so on, see Ref. [181] for an introduction to the subject), and some of these are only now starting to be applied to the collision problem. It will be auspicious for the future to foster a closer collaboration between these two areas of research, especially as the interest in continuum processes involving large biomolecules and nanostructures continues to strengthen.

2.2   Approximations

The starting point of the approximation procedure is to develop an ansatz for the wavefunction of the total system. One of the simplest and most used methods is a close coupling expansion [10], in which the $N + 1$ electron wavefunction is expanded in eigenstates of the target multiplied by an unknown function for the scattering electron. Since usually the electronic excitations of the target are limited to the first few excited states, these expansions can be kept reasonably small, usually limited to a number of electronic target states of 10 or fewer. The unknown function that multiplies the target wavefunctions is a continuum orbital for the scattered electron. These terms in the expansion only represent channels that are open (this is not always true, e. g.

in quantum defect theory (MQDT) as we will see in Sec. 2.5), allowing one electron to escape to infinity. To describe closed channels another sum, this time over square integrable functions (L^2 functions) will have to be added to the wavefunction ansatz.

The close-coupling concept leads to a trial variational wavefunction that depends parametrically on the nuclear coordinates, and is an antisymmetrized product of the target and scattering electron wavefunctions:

$$\Psi_\gamma = \mathcal{A} \sum_{\gamma'} \Phi_{\gamma'}(x_1...x_N, R)\phi_{0,\gamma'}(x) + \sum_j \chi_j(x, x_1...x_N, R) \tag{2.2}$$

where x represents the spatial ($\vec{r}$) and spin (σ) coordinates of the scattering electron, $x_1...x_N$ are the coordinates of the target electrons, and R the nuclear coordinates. In Eq. 2.2, γ represents the set of quantum numbers that fully describe the state of the system, and the sum over γ' allows for different configurations of the compound system (target + scattered electron) to contribute. The second sum represents the antisymmetrized square integrable terms, which are also called polarization and correlation functions, because they allow in some sense a relaxation of the target electronic density under the action of the incoming electron, whereas the first sum would keep the target electrons strictly confined to their bound state basis set. In principle, the configuration state functions (CSF) that correspond to the Φ and χ in Eq. 2.2 contain spin degrees of freedom, and the total wavefunction has to be antisymmetric. Since we will be mostly dealing with closed-shell molecules the total spin state will be a singlet and we only write explicitly the spatial degrees of freedom. In the following, integrals imply a trace over the spin degrees of freedom, where appropriate. In the remainder of this thesis the x_i spatial and spin coordinates in Eq. 2.2 will be replaced by the spatial coordinates $\vec{r_i}$.

If only the ground state configuration γ' in this sum is retained, the approximation

made is called static exchange. We can obtain the static exchange equation for the scattered electron multiplying the Schrödinger equation from the left by the target wavefunction and integrating over the variables of the bound electrons:

$$\int d\vec{r_1}...d\vec{r_N}\Phi(\vec{r_1}...\vec{r_N})(\hat{H}-E)\mathcal{A}\Phi(\vec{r_1}...\vec{r_N})\phi_0(\vec{r}) \qquad (2.3)$$

This is valid for any form of the target wavefunction. In particular we consider a configuration-interaction (CI) type form:

$$\Phi(\vec{r_1}...\vec{r_N}) = \sum_i c_i\chi_i(\vec{r_1}...\vec{r_N}) \qquad (2.4)$$

where c_i are the CI coefficients and the χ_i is a Slater determinant. For closed shell target molecules, we can simplify this equation considerably since the scattering orbital will be forced to be orthogonal to the target orbitals for the Pauli exclusion principle. We then obtain

$$(-\frac{1}{2}\vec{\nabla}^2 + V_s - E)\phi_0(\vec{r}) = \sum_{i,j} c_ic_j \sum_{k=1}^N \phi_{ki}(\vec{r})\int d\vec{r'}\frac{\phi_{kj}^*(\vec{r'})\phi_0(\vec{r'})}{|\vec{r}-\vec{r'}|} \qquad (2.5)$$

where the ϕ_j $(j \geq 1)$ are the target molecular orbitals of a closed-shell molecule. The electrostatic potential V_s is the averaged Coulomb interaction of the scattered electron with all the other electrons and the nuclei

$$V_s(\vec{r}) = \sum_{i,j} c_ic_j \sum_{k=1}^N \int d\vec{r'}\frac{\phi_{ki}^*(\vec{r'})\phi_{kj}(\vec{r'})}{|\vec{r}-\vec{r'}|} - \sum_\alpha \frac{Z_\alpha}{|\vec{r}-\vec{R_\alpha}|}. \qquad (2.6)$$

The term on the right hand side of Eq. 2.5 is referred to as the exchange potential.

So far, we have presented the equations for static exchange calculations, which means complete neglect of correlations. We will see that, when we use a polarization potential, that term will contain a short range cutoff that can be interpreted as mimicking a correlation term. We deem it more appropriate to present here uncorrelated

equations, since this simplifies the derivation of the approximations that have been implemented here, and also because we never perform a CI calculation on the target + scattered electron system. For this reason it would not be pertinent to present fully correlated equations. Furthermore, it is possible to see that the static potential (and also the exchange potential in LDA approximation) depends only on the electron density, which allows us to treat the target molecule at a correlated level without changing the formalism, since this only amounts to changing the Hartree-Fock electron density to a correlated one. We will discuss the effect of this change in section 2.2.3. The methods we develop here have been published in Refs. [191, 192, 194] and the associated computer codes are available through the CPC library [1].

2.2.1 R-matrix method

The R-matrix method is a well-established tool for problems where the continuum portion of the spectrum of a Hamiltonian must be treated. In its usual implementation, it involves diagonalization of the (Bloch-modified) Hamiltonian operator in a box subject to some fixed boundary condition obeyed by the basis orbitals. The R-matrix box partitions the space into two regions. There is an internal reaction zone, within which all the short-range interactions are confined, and an external zone, where instead either no potential is present or else there is a long range Coulomb or dipole potential (or both), and the behavior of the solutions of the Schrödinger equation is very simple. In some studies, other long-range multipole potentials are included in the external zone. [12, 45] We use the R-matrix method in the eigenchannel form [74]. In this case we seek those stationary states for which the logarithmic derivative of the wavefunction at the surface of the R-matrix box is constant at every point. Refs. [48, 72, 109] derive a new

variational principle,

$$b \equiv -\frac{\partial \log{(r\Psi_\beta)}}{\partial r} = 2\frac{\int_V \Psi^*(E - \hat{H} - \hat{L})\Psi dV}{\int_V \Psi^*\delta(r - r_0)\Psi dV}, \tag{2.7}$$

for the logarithmic derivative of the wavefunction, starting from the Rayleigh-Ritz variational principle for the energy. If Ψ is discretized in some basis set inside a spherical box, within which all the short range dynamics is localized, this results in a generalized eigenvalue problem for b:

$$\underline{\Gamma}\vec{C} = 2(E\underline{O} - \underline{H} - \underline{L})\vec{C} = \underline{\Lambda}\vec{C}b \tag{2.8}$$

where $\underline{\Lambda}$ is the overlap of the basis functions calculated on the surface of the R-matrix box and $\hat{L}$ is the Bloch operator,defined as

$$\hat{L} = \frac{1}{2}\delta(r - r_0)\frac{\partial}{\partial r}r, \tag{2.9}$$

$\underline{O}$ is the volume overlap of the basis set and r_0 is the radius of the box. The eigenvector $\vec{C}$ represents the expansion coefficients of the basis set used. Both $\underline{\Gamma}$ and $\underline{\Lambda}$ are defined in appendix A for the finite element basis set used in this work. It is possible to partition the basis functions in two subspaces, closed and open, depending on whether their value at the surface of the box is zero or nonzero [74]. This allows us to reduce the burden of the solution of Eq. 2.8 to the easier task of solving a much smaller eigenvalue problem of type

$$\Omega\vec{C}_o = (\underline{\Gamma}_{oo} - \underline{\Gamma}_{oc}\underline{\Gamma}_{cc}^{-1}\underline{\Gamma}_{co})\vec{C}_o = \underline{\Lambda}_{oo}\vec{C}_o b \tag{2.10}$$

in the open functions subspace, in addition to the large auxiliary system of equations:

$$\underline{\Gamma}_{cc}\vec{C}_c = -\underline{\Gamma}_{co}\vec{C}_o \tag{2.11}$$

where the subscripts indicate the matrix blocks. At the boundary of the R-matrix box Ψ is matched to an external solution depending on the long range tail of the potential (Bessel functions for neutral molecules, Coulomb functions for molecular ions). This allows us to calculate the reaction matrix $\underline{K}$, from which the scattering matrix is derived as

$$\underline{S} = \frac{1 + i\underline{K}}{1 - i\underline{K}} \tag{2.12}$$

Scattering cross sections can then be calculated in the standard manner. One difference from the usual treatment performed in quantum mechanics textbooks [165] for spherically symmetric potentials, will be in this case the fact that we want to average over the molecular orientations. From the scattering matrix S, the total (elastic) integrated scattering cross section can be calculated as [41]:

$$\sigma = \frac{\pi}{2E} \sum_{lm,l'm'} \mid \delta_{ll'}\delta_{mm'} - S_{lm,l'm'} \mid^2 \tag{2.13}$$

where E is the energy of the incident electron and the S matrix indices are angular channels, since here we do not include any excited target states [41]. A similar treatment is possible in the case one wants to derive differential cross sections, and we can calculate them using this approach employing formulas 46-47 of Ref. [41], one example is given in Fig. 4.5.

2.2.2   Finite elements

The essence of the finite element method is the use of a basis set that is defined over small local regions. By this we mean that each basis function is nonzero only within a small region, and it has a simple polynomial form. By using many "sectors" or "elements" (the volume over which the local basis function is defined) though, it is

possible to reproduce very complex features of the solutions to the differential equation of interest. An introduction to these basis sets and their practical implementation can be seen in Refs. [19, 21]. We discretize Ψ using finite element polynomials in all three dimensions. The basis set is a direct product of 4 cubic Hermite polynomials defined locally in each sector for each dimension. The use of a spherical coordinate grid, in r, θ, ϕ makes the boundaries of the sectors simple and the three-dimensional integrals (the main bottleneck of these calculations) faster to calculate. The grid is represented in Fig. 2.1.

The finite element basis set is composed of piecewise polynomials, which provides advantages over a global basis representation. In particular one can treat potentials and wavefunctions of complicated form by simply reducing the size of the elements in which the polynomials are defined, in those areas where fine features arise. In our case the basis functions are third order Hermite polynomials, which allow us to achieve function and derivative continuity, while still permitting a simpler implementation compared to higher order polynomials. Each polynomial is defined in a hexahedral sector (a cube in the rescaled variables used for the evaluation of the integrals), and since the wavefunction is discretized in terms of finite elements in all three dimensions, the basis set is a direct product of 4 polynomials in each dimension per sector, which means 64 basis functions are defined in each sector.

In finite element analysis (FEA) the polynomials are matched with the ones in neighboring sectors to ensure functional and derivative continuity (and mixed derivative continuity also, in multidimensional FEA). Each sector has 8 physical nodes (at the edges of the cube) and the basis functions defined in the sector have coefficients (to be determined by the solution of the Schrödinger equation) that represent the value of the

wavefunction, or its derivatives, at the nodal point. In the language of finite element analysis, a node is the vertex of one of the sectors into which the three-dimensional space is divided. The matching at the boundary of each sector is imposed when assembling the global Hamiltonian matrix from the local ones. The global index of functions that correspond to the same node and quantity (e. g. derivative) in neighboring sectors has to be the same. Hence their matrix elements have to be summed together. Details of the procedure are given in Appendix A.

2.2.3   Potential and DFT

Using an approach derived from Refs. [42, 139], we approximate the exchange integral (that is nonlocal), by a local form using free electron gas (FEG) orbitals [93], i.e. plane waves, for the target molecule and using the first order Born approximation

$$\phi_0 = N e^{i\vec{k}\cdot\vec{r}} \tag{2.14}$$

for the scattered electron. The arbitrary normalization constant N is unimportant and it disappears as soon as we express the exchange functional as a product of a local exchange potential times the scattered wave. After these substitutions are made, it is possible to evaluate the integral on the right hand side of Eq. 2.5 analytically, obtaining a local potential of the form

$$V_{ex}(\vec{r}) = -\frac{2}{\pi} k_F F(\eta), \tag{2.15}$$

whereas the Fermi momentum k_F (the momentum of the electron that is at the top of the Fermi sea in a free electron gas) is:

$$k_F(\vec{r}) = [3\pi^2 \rho(\vec{r})]^{1/3}. \tag{2.16}$$

r (a.u.)
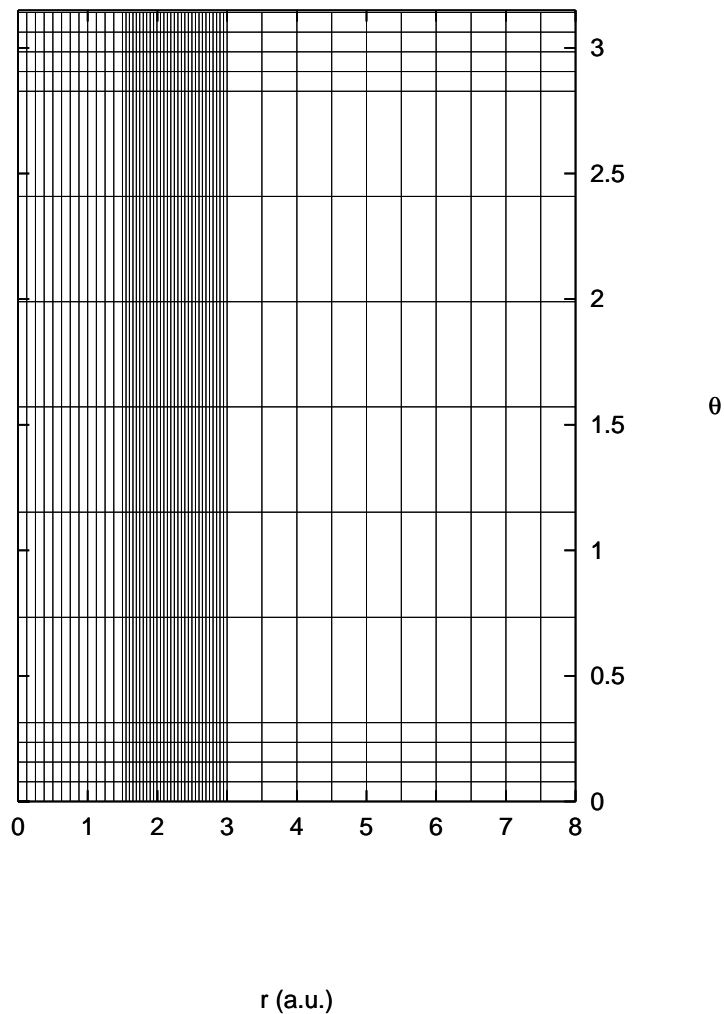
Figure 2.1: From this two dimensional cut in the radius r and the polar angle θ of the finite element grid (for a CO_2 target), the finer mesh is apparent near the oxygen nuclei localized at $r = 2.19$ a.u. and $\theta = 0$ and π respectively, while the carbon is located at the center of the grid $(r = 0)$. A drawback of this type of separable grid in spherical coordinates is that it is more fine than necessary at $1.5 < r < 3$ and $0.3 < \theta < 2.8$ radians. From Ref. [192].

The other functions present in Eq. 2.15 are

$$F(\eta) = \frac{1}{2} + \frac{1 - \eta^2}{4\eta} \log \left| \frac{1 + \eta}{1 - \eta} \right| \tag{2.17}$$

$$\eta = \frac{k}{k_F}, \tag{2.18}$$

where k is the modulus of the momentum of the scattered electron. It should be noticed that the exchange potential in Eq. 2.15 is energy dependent.

Many functionals of this form exist [139], with minor differences in the expression for k, the scattering electron wavenumber. The functional we have used most successfully is the Hara exchange [81] where

$$k = \sqrt{2(E + I) + k_F^2} \tag{2.19}$$

and I is the ionization energy of the molecule while E is the energy of the incident electron. This emerges from the assumption that the scattered electron and the electron in the highest energy bound state (the Fermi electron, which has momentum k_F) move in the same potential field; V_{ex} then depends only on $\vec{r}$, through the electron density $\rho(\vec{r})$, as a local potential, and on the energy, through the functional dependence of the momentum k as approximated in Eq. 2.19.

We have also experimented with other functional forms of the exchange interaction (still based on a FEG approximation). One in particular is the Slater exchange [173], derived by averaging the function $F(\eta)$ over the momenta of all the electrons up to the Fermi level, which has often been used to calculate bound states in atoms and molecules. However the results using Slater exchange are unsatisfactory for continuum scattering states, presumably owing to the neglect of the energy dependence in this model.

Since our main goal is to treat low energy scattering processes (0-10 eV) we linearize the energy dependence of the functional in Eq. 2.17, in order to calculate the

exchange potential matrix elements at all energies at once. For a molecule like CO_2, the matrix element calculation requires around 2 hours on an Alpha 500 Mhz workstation. The next step is the solution of the linear system and the determination of the scattering observables, which requires approximately 15 minutes per energy desired, for a basis set size of 33000. This step is trivially parallelizable, of course.

We have recently added to our computer code the capability to use a parameter-free correlation-polarization potential [35, 62], based on density functional theory (DFT) ideas. As shown in Ref. [102] the polarization-correlation contribution is physically related to the distortion-relaxation effect on the molecule generated by the incoming electron. This is extremely important for an accurate description of the scattering process. The long range part of this potential is a simple multipole expansion, of which we retain only the induced dipole polarization terms:

$$V_{pol} = -\frac{1}{2r^4}[\alpha_0 + \alpha_2 P_2(\cos\theta)] \qquad (2.20)$$

where α_0 and α_2 are the totally symmetric and nontotally symmetric components of the polarizability tensor, and are calculated *ab initio* using electronic structure codes. While the quadrupole term in the polarizability tensor has 5 components, we never resort to its full form, since we have verified numerically that the second term in the polarization potential ($\alpha_2 = 3\alpha_{zz} - \boldsymbol{Tr}(\alpha)$) is already not very important, and we omit it altogether when calculating scattering from larger molecules. To extract the molecular electron density, gradient, Laplacian, and the electrostatic potential needed to construct the scattering potentials, we use GAUSSIAN 98 [150], but MOLPRO [203] has the same capabilities and exploits the same file formats, as does PC-GAMESS [71]. The latter is also freely available.

In the volume where the electronic density of the target is not negligible, this potential is nonlocal. The interaction can be approximated again as a local potential, different forms of which have been suggested in the literature. The one we use is based on DFT (specifically on the LYP potential of Ref. [107]) and it has yielded reliable results in the work of Gianturco and coworkers [117]. This form makes use of the electron density, its gradient and Laplacian, which have to be calculated for each target molecule. The short and long range potentials are matched unambiguously at the innermost crossing point, whose radius is dependent on the angles.

A derivation of this short-range correlation-polarization potential can be sketched along the lines of Refs. [35, 62, 107]. We start by choosing a particular form for the correlated wavefunction for an N-electron system. Taking x_i to denote both the spin (σ_i) and spatial ($\vec{r}_i$) coordinates of the electron, this reads:

$$\Phi(x_1...x_N) = \Phi_{HF}(x_1...x_N) \prod_{i<j}^{N} [1 - \phi(\vec{r_i}, \vec{r_j})] \tag{2.21}$$

where

$$\phi(\vec{r_i}, \vec{r_j}) = e^{-\beta^2 r^2}[1 - \Theta(R)(1 + r/2)] \tag{2.22}$$

is a correlation function that obeys the cusp condition at the coalescence point. Here $R = \frac{1}{2} \mid \vec{r_i} + \vec{r_j} \mid$, and $r =\mid \vec{r_i} - \vec{r_j} \mid$. $\beta = q\rho^{1/3}$ can be related to the excluded volume (see Eq. 5 of Ref. [62]) and q has to be determined. The form chosen for the correlation function determines

$$P_2(\vec{r}_1, \vec{r}_2, \vec{r'}_1, \vec{r'}_2) = P_2^{HF}(\vec{r}_1, \vec{r}_2, \vec{r'}_1, \vec{r'}_2)[1 - \phi(\vec{r}_1, \vec{r}_2) - \phi(\vec{r'}_1, \vec{r'}_2) - \phi(\vec{r}_1, \vec{r}_2)\phi(\vec{r'}_1, \vec{r'}_2)]$$

$$\tag{2.23}$$

for the second-order (or two-electron) density matrix traced over spin, where P_2^{HF} is the second-order Hartree-Fock density matrix. Making now the approximation that

$P_1(\vec{r}_1, \vec{r'}_1) = P_1^{HF}(\vec{r}_1, \vec{r'}_1)$ for the first order (or one-electron) density matrix, the correlation energy is derived as

$$E_c = \frac{1}{2} \int P_2^{HF}(\vec{r}_1, \vec{r}_2)[\phi(\vec{r}_1, \vec{r}_2)^2 - 2\phi(\vec{r}_1, \vec{r}_2)]\frac{1}{r_{12}} dr_1 dr_2 \qquad (2.24)$$

and Θ becomes a function only of β (see Ref.[35]). The correlation energy is finally recovered by expanding $P_2^{HF}(\vec{r}_1, \vec{r}_2)$ to second order in the interparticle coordinate. At this point though, the correlation energy involves a gradient of $P_2^{HF}(\vec{r}_1, \vec{r}_2)$. Through some further work, Lee Yang and Parr [107] recovered a final expression that is only a function of the one-electron density, and therefore more akin to the spirit of DFT. Essentially the steps required involve first expressing the second-order Hartree-Fock density matrix in terms of the first order one (see Eq. 4 of Ref. [107]) and secondly expressing the gradient in terms of the Hartree-Fock local kinetic energy. This finally gives an expression like Eq. 10 in Ref. [107]. At this point, to obtain the correlation potentials we use, it is necessary to perform a functional derivative of the correlation energy with respect to the electron density:

$$V_c = \frac{\partial}{\partial\rho} E_c = -a(F'\rho + F) - abC_F\rho^{5/3}(G'\rho + \frac{8}{3}G)$$
$$-\frac{ab}{4}[G''\rho \mid \nabla\rho \mid^2 + G'(3 \mid \nabla\rho \mid^2 + 2\rho\nabla^2\rho) + 4G\nabla^2\rho]$$
$$-\frac{ab}{72}[3G''\rho \mid \nabla\rho \mid^2 + G'(5 \mid \nabla\rho \mid^2 + 6\rho\nabla^2\rho) + 4G\nabla^2\rho] \qquad (2.25)$$

$$F = (1 + d\rho^{-1/3})^{-1}$$

$$G = F^{-5/3}e^{c\rho^{-1/3}} \qquad (2.26)$$

$$C_F = \frac{3}{10}(3\pi^2)^{2/3}$$

for closed shell molecules, these expressions are identical to the ones in Ref. [62] and are shown here for completeness. The parameters a, b, c, d are chosen by a fitting procedure

to the helium atom, and were shown to be effective in predicting energy correlations for atoms and molecules [35, 107]. Note that it is possible to include rigorously the polarization-correlation physics in an effective potential approach as in Ref. [128].

All the information needed to construct the local potential described in Eqs. 2.25-2.27 can be extracted from standard *ab initio* quantum chemistry codes; in this work we have used GAUSSIAN 98. The electrostatic potential and the electron density (needed to construct the exchange functional) for the target molecule are calculated on a uniform cubic grid at a CI (singles and doubles) level for the molecules presented here. The difference in using an electrostatic potential and density calculated at the RHF level or at the CI level for CO_2 at its equilibrium geometry amounts roughly to a difference of 10% in the calculated eigenphase sum and overall magnitude of the elastic cross sections. These calculations usually require a minimal amount of time, of the order of ten minutes per nuclear geometry for CO_2 on the aforementioned computational platform. The potentials are then interpolated on the three-dimensional quadrature grid using fifth order splines. We avoid interpolating over the nuclear singularities by premultiplying the potential at each grid point by the product of the distances of the point from all the atoms, then performing the interpolation over this quantity that does not possess Coulomb singularities any longer.

2.3   Photoionization

The relationship between electron scattering and photoionization is a close one [41]. The scattering wavefunction relative to a photoionization process is essentially the time-reverse of the one for the scattering of an electron with a positive ion [74]. Thus it is useful to examine the resonant structures of the electron with the ionic state, since
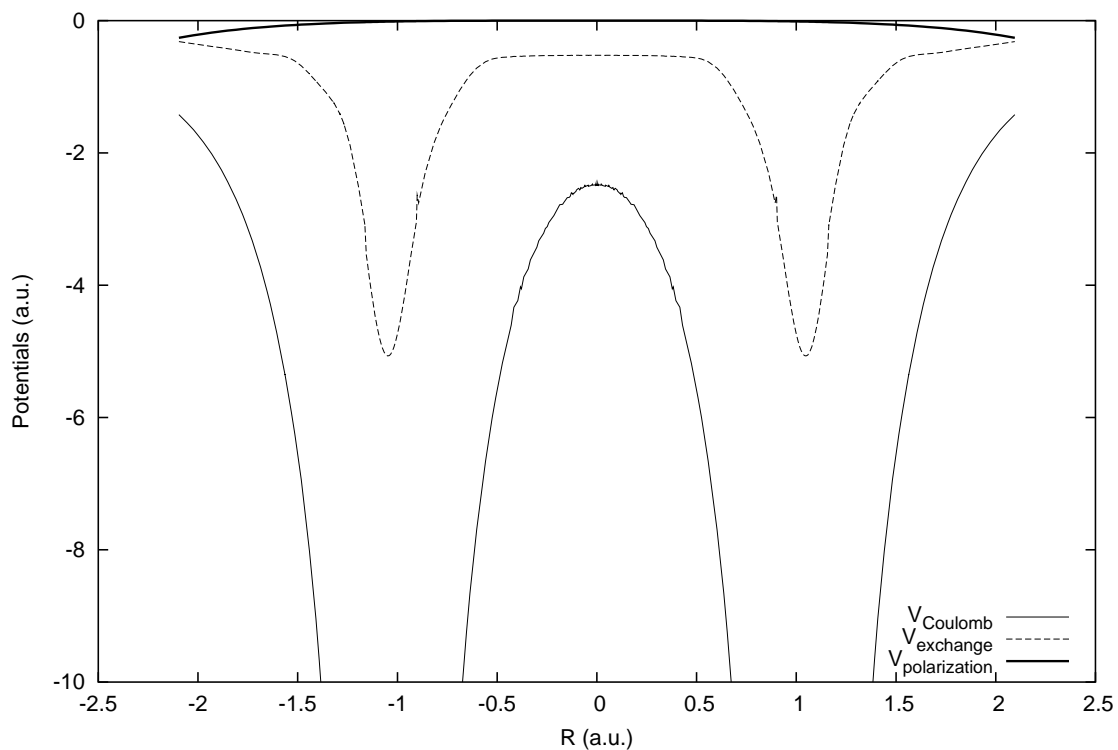
Figure 2.2: The three terms of the potential for a N_2 molecule. The exchange potential is large only at the nuclei (at $r = -1.094$ and $r = 1.094$ a.u. in the equilibrium configuration of the molecule) where the static potential is singular, so V_{ex} is always much smaller than V_s. On the other hand the polarization potential becomes important in the outer zone, where the electron density of the molecule goes to zero. From Ref. [192].

photoionization allows to distinguish between different initial wavefunction symmetries. In the independent electron approximation, the photon extracts the electron from just a single Hartree-Fock orbital, the initial state. The relevant matrix element for the photon absorption from a molecule is:

$$M_{0,f} = < \psi_f \mid e^{ik \cdot r} \hat{\epsilon} \cdot \vec{\nabla} \mid \psi_0 >, \tag{2.27}$$

where ψ_f is the final state. In our case the final state will have only partial wave indices, since our scattering calculation is done at the static exchange level. For optical transitions, the dipole approximation can be used, leading to dipole matrix elements:

$$d_{0,l'm'}^{(-)} = < \psi_{l'm'}^{(-)} \mid \hat{\epsilon} \cdot \vec{r} \mid \psi_0 >, \tag{2.28}$$

using the length form of the dipole operator, where $\hat{\epsilon}$ is the polarization of the incident photon, ψ_0 the initial wavefunction (the orbital from which the electron is ionized), and $\psi_{l'm'}^{(-)}$ the final state of the continuum electron. This is formed from R-matrix eigenstates $\psi_{l'm'}$ using

$$\underline{\psi}^{(-)} = \underline{\psi}(\underline{I} - i\underline{J})^{-1}, \tag{2.29}$$

where I and J are matrices generated from the Wronskians of the solutions inside and outside the R-matrix box, as described in Eqs. 2-31 and 2.41 of Ref. [74], generating a wavefunction with incoming wave boundary conditions:

$$\psi_{l'm'}^{(-)} = \sum_{lm} Y_{lm}(\theta, \phi) \left(\frac{1}{i\sqrt{2}} f_l^+ \delta_{ll'} \delta_{mm'} - \frac{1}{i\sqrt{2}} f_l^- S_{lm,l'm'}^\dagger \right), \tag{2.30}$$

where $f^{\pm}$ are incoming and outgoing wave solutions (exponential functions with unit coefficient), respectively, and $S^\dagger$ is the hermitian conjugate of the scattering matrix. The total cross section can be easily calculated from the $d_{0l'm'}^{(-)}$ matrix elements by

performing a rotational average. This simplifies after expressing the dipole operator as

$$\hat{\epsilon} \cdot \vec{r} = \sum_{m_\gamma} \frac{4\pi}{3} r Y_{1m_\gamma}(\theta, \phi) Y^*_{1m_\gamma}(\theta', \phi'). \tag{2.31}$$

where the first spherical harmonic refers to the vector $\vec{r}$, while the second refers to the polarization vector in the body frame, and m_γ gives the projection of the polarization vector on the molecular z axis. After angular integration, the final cross section is:

$$\sigma = N \frac{4\pi\omega}{3} \sum_{l'm'} d^{(-)}_{0,l'm'} d^{(-)*}_{0,l'm'} \tag{2.32}$$

where N is the number of degenerate electrons that can be knocked out by the photon. For example, $N = 4$ for a fully occupied π orbital in CO_2. The cross section output from the code has to be multiplied by the orbital occupation number. As an alternative to Eq. 2.28, the velocity form of the dipole matrix element,

$$d^{(-)}_{0,l'm'} = \frac{1}{\omega} < \psi^{(-)}_{l'm'} \mid \hat{\epsilon} \cdot \vec{\nabla} \mid \psi_0 >, \tag{2.33}$$

can be used in the code, although this will be slower because of the need to differentiate many continuum wavefunctions. In fact, in the case of many initial wavefunctions, it is too expensive to store all of their gradients, so the final wavefunctions have to be differentiated at each energy point.

Notice that in photoionization of a closed-shell molecule, the construction of our exchange potential will not be strictly correct, since we only derived our exchange functional for closed shell molecules and the resulting ion is a doublet. The final error made in this case will however be quite small, due to the dominance of the electrostatic ionic potential everywhere in space.

The calculation of dipole matrix elements for a returning electron recolliding with a molecule, therefore with boundary conditions opposite to photoionization, is useful also

in the three step model [113] calculation of high harmonic generation (HHG) spectra [36], that are generated by femtosecond and sub-femtosecond pulses. This area of research is growing at a very rapid pace and interesting applications to map the electronic dynamics of molecules undergoing chemical reactions have already been published [13]. This is ripe for a future application of the methods we are developing here.

2.4 Other methods

In the work included in this thesis, there are many different kinds of processes that we are trying to model, and they will require a number of different approaches. The accuracy needed in calculations for small molecules is much higher than for the large DNA bases, where the approximate treatment we have just discussed is good enough, since more accurate calculations are at present too large to perform. In the following sections a description of the other methods that have been used in this work to calculate scattering quantities will be given and the different schemes will be compared to assess when they should be used and what their weaknesses are. To develop methods that can accurately solve the electron-molecule scattering problem is a serious job in itself, and the approaches and programs we describe have been developed by large teams of scientists over the past twenty or so years.

2.4.1 Ab initio methods

A possible alternative route to calculate quantum defect parameters, for scattering of an electron from an ion, is to use bound state quantum chemistry programs, which allow very large configuration interaction (CI) expansions to be used, and therefore high accuracy for the first few low-lying excited states of the $N + 1$ electron system [132].

We have used this approach to calculate Rydberg state Born-Oppenheimer surfaces and K-matrices relevant for HCO^+ dissociative recombination calculations [104], i.e. by calculating the first few Rydberg states (up to $n = 4$) and then neglecting the energy dependence of the higher state eigenquantum defects.

The positive side of this approach is the high precision it is possible to reach using very large configuration spaces (of the order of a million). On the other hand, this procedure is limited by two factors: the higher lying excited states will be less and less converged (and therefore the Rydberg states above, say, $n = 4$ will be incorrect) and the scattering quantities that are of interest here (K-matrices through equation 3.1) will have to be obtained through a fitting procedure, which can be both cumbersome and nonunique. Clearly, above the ionization threshold this approach cannot be used, since there would be a variational collapse of the states onto the ionic surface energies, and an incorrect description of the resonances, due to the bound state boundary conditions imposed that cannot represent the continuum correctly. This approach will be used in the dissociative recombination calculations of Chapters 3 and 6.

2.4.2 Rmatrix-UK

Small molecules often need more accuracy than we are able to provide with the methods just outlined. For this purpose we have used a different approach that involves the R-matrix UK polyatomic codes developed by J. Tennyson and coworkers [135, 136]. The main difference with the approach we have described so far is that the solution of the inner region is a truly many-particle problem, developed starting from quantum chemistry configuration interaction (CI) software. Within the limit of the basis sets used, these codes can give an exact solution to the electron interaction with the many

electrons present in the molecule, at least in principle.

The calculations are usually done in this case starting from a Hartree-Fock mean field description of the target molecule, followed by a CI step to get better target wavefunctions. Many target states might be needed if electronic excitations are considered. The next step involves adding an electron to the molecule and diagonalizing the full Hamiltonian, including the interaction of the scattering electron with the target molecule. A wavefunction of the form:

$$\psi_k = \sum_{ij} \phi_i(x_1...x_N)u_{ij}(x_{N+1})a_{ijk} + \sum_i \chi_i(x_1...x_N)b_{ik} \qquad (2.34)$$

is assumed, where $\phi_i(x_1...x_N)$ are target CI configuration state functions, $u_{ij}(x_{N+1})$ are continuum wavefunctions, while $\chi_i(x_1...x_N)$ are L^2 functions, a and b are the variational coefficients. This is essentially a close coupling expansion with polarization/correlation configurations that allow us to describe the added electron in more compact configurations inside the target virtual orbital space, in a sense allowing the target to relax under the influence of the scattered electron, much as our model polarization potential 2.2.3 does. This wavefunction form goes beyond the static exchange approximation in that it allows electronic excitation of the target. We use this approach to calculate potential energy surfaces and K-matrices for dissociative recombination calculations. The limitation of this approach is one of size, in that when the number of electrons in the scattering problem becomes large the scaling of CI calculations (even with inclusion of just single and double excitations) goes like N^6, where N is the number of single-electron basis functions, and is proportional to the number of electrons. Already a simple HF calculation scales like N^4. This unfavorable scaling prevents this approach from being extended to carry out accurate calculations for molecules with more than

about 10 atoms, especially if what is of interest is the effect of bond breaking on the continuum states. Homolytic bond breaking (in which each of the fragments retains a bonding electron) inherently requires more than one reference configuration, since the Hartree-Fock wavefunction dissociates incorrectly in this case, and in general many configurations will be needed for an accurate description of the process.

Two other methods that are based on the same philosophy of using a full many-electron description of the electron-molecule interaction, and which are competitive with the Rmatrix-UK code. These are the Schwinger variational approach of McKoy and co-workers [205] and the Kohn variational code of McCurdy-Rescigno and coworkers [156], which share roughly the same advantages and limitations as the code we just described.

For the future, promising methods that use a DFT-based description of the inter-action, using more accurate functionals than we have at present [148], which importantly eliminate the local density approximation, are being developed and applied to scattering problems [198]. The scaling of these methods is much better than wavefunction meth-ods, and they might be the only way to treat interactions of a continuum electron with very large targets in the future, to sufficient accuracy. Much as in bound-state quan-tum chemistry calculations, the success of DFT calculations could prove critical for expanding the range of systems that can be treated, especially for new and extremely interesting applications to biomolecules [24].

2.5   QDT and long range interactions

The nature of the electron scattering problem is such that we can devise two zones in configuration space that have distinct properties. In the short range zone, the problem is essentially many body in nature, whereas the long range zone effectively

reduces to a one-body problem of scattering from a potential. When the outer electron is outside the area where the target electron density is confined, there is no nonlocal exchange interaction. The first zone is the most complicated to treat, and we have seen how R-matrix techniques for example can be used for that purpose. The outer zone instead has a feature that is very important: at sufficiently large distances, one can solve for scattering of a particle in the long range potential and get an analytical form of the wavefunction. The computational cost of solving the Schrödinger equation out to very large distances is thus reduced, and equally importantly, it factors out analytically from the S-matrix the long-range part of the phase shift. This key idea allows us to obtain quantities like S-matrices, phase shifts, time-delays, etc., which depend only on the short-range potential, and therefore are much less energy dependent than the ones that also include the long-range phase accumulation. This can in turn save much computation time when dealing with processes for which the scale of the energy dependence of the short-range part of the S-matrix is much weaker than for the long-range part. In the treatment of electron collisions with rotating/vibrating molecules this concept is useful, since the energy scales of the different degrees of freedom are so different, as we will see in Ch.3. This is one of the fundamental ideas of quantum defect theory (QDT), which will be important in the following, especially when we will deal with dissociative recombination reactions.

QDT is a tool that allows to tackle a class of problems that are essentially intractable with any other method, for example the coupling of many degrees of freedom with the infinite number of Born-Oppenheimer potential energy surfaces that arise in scattering from a positive molecular ion. It is conceptually very simple, but in the literature [74, 75, 77, 169] it has been usually obscured by complexities associated with a

large number of parameters, basis pairs and so on.

The key ideas are essentially three. The first one we mentioned already is the division of the scattering electron coordinate space into two areas, short range and long range. The long range part can be treated analytically and effectively removed from the S-matrix to make it a smooth quantity. The second idea is that the boundary conditions on closed channels should be imposed as late as possible in the course of a calculations, again in order to obtain quantities that are smooth in energy, since the sharp energy dependence at ionization thresholds has been eliminated. The third idea is that there is a correspondence between the phase shift at positive energy and the parameter that identifies the position of a bound state (the effective quantum number), at negative energy. For Coulomb systems that automatically possess high lying Rydberg bound states this is easy to see in that the bound states will look more and more like the ionic state to which they converge plus a loosely bound electron. In the case of single channel problems, their energies will be given by the Rydberg formula

$$U_{n,i,\Lambda}(\vec{Q}) = U_i^+(\vec{Q}) - \frac{1}{2(n - \mu_{i,\Lambda}(\vec{Q}))^2} \tag{2.35}$$

where $\vec{Q}$ represents all the vibrational coordinates. In the case of multichannel problems the quantization condition Eq. 4.5 has to be applied to determine the position of the bound states. The interaction of the electron with the ionic core in these very extended and high energy weakly bound states will be more and more similar to that of a free, positive energy electron. In Eq. 2.35, n is the principal quantum number, i is the index of the ionic electronic state, while Λ is the projection of the electronic angular momentum on the molecular symmetry axis and $\mu_{i\Lambda}(\vec{Q})$ is the quantum defect for that geometry and molecular symmetry. Λ is a good quantum number for linear molecules,

and we will use it in HCO$^+$ to label states in bent geometries as well, even though the classification will be approximate. A derivation that shows that the quantum defect in formula 2.35 can be seen as a low-energy electron scattering phase shift can be found in Sec. IIB of Ref. [74]. An important consequence of treating the bound-state physics as a scattering process is that we can use the S-matrix to determine bound-state positions, when the problem is multichannel in nature:

$$(S_{cc}^\dagger - e^{2i\beta})B = 0 \tag{2.36}$$

and the roots of the determinantal equation will give the Rydberg energies. In this equation $S_{cc}^\dagger$ is the part of the S-matrix relative to the closed channels (in which fragmentation all the way to the asymptotic region is energetically forbidden), β is a diagonal matrix of long range phase parameters [74, 75]. Note also that all channels are closed when the energy level is truly bound. In an energy range where open channels are also present, see Eq. 3.10. It is important to restate that QDT has to do with the long-range part of the scattering process, and cannot give by itself the short-range quantities which are needed to complete the modeling of the interaction. These must be calculated by either *ab initio* bound state quantum chemistry calculations or R-matrix (or similar approaches) for scattering processes. Both these avenues will be explored in Ch. 3.

2.5.1   External potentials

Many external potentials have been treated from a QDT standpoint: Coulomb, dipole [75], Coulomb plus dipole [180], polarization [199] and dispersion forces in atom-atom scattering [27]. Here we will be mostly concerned with Coulomb and dipole potentials. The long range form of the wave function will be always some linear combination

of a base pair consisting of a regular (at the origin) and an irregular solution of the Schrödinger equation in the pure long range potential. Since a linear second order differential equation has two linearly-independent solutions, any solution can be expressed as linear combinations of those two. We will call these functions f and g respectively, without specifying their precise functional form, which will vary with the external potential. In the case of zero long-range potential, the external solutions are the familiar spherical Bessel functions.

Given these two functions, matching at the boundary of the internal region with the internal R-matrix of Sec. 2.2.1 generates the K-matrix of Eq. 2.12 in the following way:

$$\underline{K} = \frac{\underline{f} - \underline{f}'\underline{R}}{\underline{g} - \underline{g}'\underline{K}} \tag{2.37}$$

here $\underline{f}, \underline{g}, \underline{f}', \underline{g}'$ are diagonal matrices of the matching functions and their derivatives at the matching point, as described in Sec. IID of Ref.[74]. In the following we will always assume that only one electron at a time can be in the external region, since the energy will always lie below the threshold for double escape and we will not consider such processes further. In electron scattering, the threshold for double escape is the first ionization threshold, which can be as low as 10 eV in some of the neutral molecules we consider in this thesis. We neglect the double escape process nonetheless throughout this work.

2.5.2   Coulomb potential

In the case of a Coulomb potential, the wavefunction at long range for the external electron will be a combination of Coulomb functions [169]

$$\psi_{l'm'} = \frac{1}{r} \sum_{lm} Y_{lm}(\theta, \phi)[f_l(r)\delta_{ll'}\delta_{mm'} - g_{lm}(r)K_{lm,l'm'}] \tag{2.38}$$

this form of the wavefunction is said to obey K-matrix boundary conditions. The functions f_l and g_l are energy normalized regular and irregular Coulomb functions, that behave like $\sin(kr + \frac{\ln r}{k} + \eta)$ and $-\cos(kr + \frac{\ln r}{k} + \eta)$ for $r \to \infty$, where η is the long range Coulomb phase shift (see Eq. 2.39 in Ref.[74]). It is important to notice that the full wavefunction for the system will be a Slater determinant of the wavefunctions in Eq. 2.38. Alternatively, the wavefunction 2.38 can be reorganized in terms of the S-matrix solutions, using a complex linear combination of f_l and g_l, or in the eigenchannel form involving eigenstates of the K-matrix, showing more effectively the short range phase shift μ_α that is not incorporated in the Coulomb functions:

$$\psi_\alpha = \frac{1}{r} \sum_{lm} Y_{lm}(\theta, \phi)U_{lm,\alpha}[f_l(r)\sin \pi\mu_\alpha - g_l(r)\cos \pi\mu_\alpha] \tag{2.39}$$

This phase shift μ_α is termed the eigenquantum defect.

At negative energy, in the bound state region, the form of the wavefunction is effectively unchanged, what varies is the asymptotic form of the Coulomb wavefunctions, which now behave as decaying and growing exponentials. Of course the exponentially growing part is unphysical, but the growth is killed when the correct boundary conditions are imposed at the end of the calculation. All of this makes this long range form of the wavefunction very convenient and flexible. Another base pair that appears in the following is (f^0, g^0), which are analytic functions of the energy and will be important

at very low negative energies since, for $\nu < l$, (f, g) are complex. The transformation between these two pairs of solutions is linear and it is defined in Eqs. 2.15a and b of Ref. [74], the long range parameters of the transformation can be found in Ref. [170] where (f, g) are called $(s, -c)$ and (f^0, g^0) are called $(f, -g)$.

2.5.3 Dipole physics

Since many of the molecules we consider have large electric dipole moments, there is a need to consider the long range effect of the dipole field on the scattered electron. Two possible options might be considered, either extending the boundary of the R-matrix box far out to a region where the dipole potential is very small, which would be extremely time-consuming for our calculations, or matching to outer region functions adapted to the dipole interaction. We choose this second route and, since in the region where only the dipole potential is dominant the Schrödinger equation is

$$-\frac{1}{2}\frac{d^2}{dr^2} - E + \frac{1}{2}(l^2 - 2D\cos\theta)\Omega_N = N(N+1)\Omega_N \tag{2.40}$$

following the example of Clark [33], we define the matrix of the operator:

$$(l^2 - 2D\cos\theta)\Omega_N = N(N+1)\Omega_N \tag{2.41}$$

where l is the angular momentum operator, θ is the angle between the incoming electron and the dipole direction, D is the dipole moment, $N(N+1)$ and Ω_N are eigenvalues and eigenfunctions. We expand Ω_N in a basis of spherical harmonics to diagonalize the system in Eq. 2.41. The order of the spherical Bessel functions that are matched in the outer region will be now N (not an integer, in general) rather than the usual orbital angular momentum quantum number l. Since the dipole moments of the molecules

in question are very large, the dipole plus centrifugal potential can become attractive for the first few channels which may thus have a complex N. In such cases we define $N = -1/2 + i\beta$ and the matching functions will become [33]:

$$\bar{j}_N(kr) = \sqrt{\frac{\pi}{2r}} \frac{1}{\sinh \frac{1}{2}\pi\beta} Im(J_{i\beta}(kr)) \tag{2.42}$$

$$\bar{n}_N(kr) = -\sqrt{\frac{\pi}{2r}} \frac{1}{\cosh \frac{1}{2}\pi\beta} Re(J_{i\beta}(kr)) \tag{2.43}$$

where $J_{i\beta}$ is a cylindrical Bessel function. This allows us to keep the functions in Eq. 2.42 always real, which therefore gives real K-matrices.

It should be mentioned, however, that at extremely low energies these functions oscillate rapidly in energy as $\sin(\beta \ln kr)$, giving rise to K-matrices that are not smooth functions of energy near threshold. Defining the base pair as in Ref. [75] solves the problem, but since we are not interested in energies below about 0.5 eV usually, the functions in Eqs. 2.42-2.43 will be sufficient.

After the matching is carried out, an analytic propagation procedure (see Eq. 8-16 of Ref. [33]) is used to get the scattering wavefunctions at a large radius. This is important since then the scattering observables, phase shifts and cross sections, must be expressed in terms of spherical Bessel functions of integer order, not the dipole-adapted ones in Eqs. 2.42-2.43.

Other multipole contributions outside the R-matrix box must be described in a different way, specifically with a propagation or perturbation method. We have tested an R-matrix propagation approach [15, 127] to include the quadrupole contribution. For the DNA components this contribution has been seen as very small, and therefore it has been neglected in the final results, while it has been included in some of the UK-R-matrix results we have obtained for HCO^+.

The dipole plus centrifugal potential is attractive if the value of the dipole moment is larger than a critical value (D_c=1.625 Debye for a nonrotating dipole). In this case the dipole interaction can bind the electron all by itself. In general, when rotation is included, the critical value of the dipole moment to have a bound state predominantly in the dipole field is around [88] 2-2.5 D and the number of dipole-bound states is finite. In the case of uracil [43, 164, 176], such a dipole-bound state exists at roughly 0.1 eV below the neutral ground state energy, at the equilibrium geometry of the target molecule.

2.5.4   Perturbation theory

The multipolar potential outside the R-matrix box can also be seen as a perturbation, since it is small enough usually that this approximation will be accurate. To this extent, an approach based on a Green function has been developed [73, 175]. We consider the partitioning of the Hamiltonian into a main part and a perturbation

$$\hat{H} = \hat{H}_0 + V \tag{2.44}$$

and we use a solution obeying K-matrix boundary conditions to $\hat{H}_0$ of the type:

$$M(r) = f_0(r) - g_0(r)K_0 \tag{2.45}$$

where all the quantities are matrices and in particular f_0 and g_0 are diagonal matrices of unperturbed long-range functions and K_0 is the unperturbed K-matrix. We can define the Green function for the system to be:

$$(\hat{H}_0 - EI)G(r, r') = -\delta(r - r')I \tag{2.46}$$

where I is the identity matrix, then the solution of the full Hamiltonian will involve an integral over G and V.

To calculate the Green function, we can start from a form of the type

$$G(r, r') = P(r)Q^T(r')A \ for \ r < r' \tag{2.47}$$

$$G(r, r') = Q(r)P^T(r')B \ for \ r > r' \tag{2.48}$$

where P and Q are two sets of linearly-independent solutions of the equation. Then we have to impose continuity at $r = r'$ and derivative discontinuity of $-2\mu I$ at the same point, where μ is the reduced mass, which will be unity in our case. Once these requirements are met, we end up with:

$$G_-(r, r') = -2\mu P(r)[W(Q, P)]^{-1}Q^T(r') \tag{2.49}$$

where $W(Q, P)$ is the Wronskian of the solutions, the advanced Green function will look like the transpose of the previous expression. Now, for the unperturbed problem

$$P(r) = (f_0(r) - g_0(r)K_0)(I + K_0^2)^{-1/2} \tag{2.50}$$

$$Q(r) = (f_0(r)K_0 + g_0(r))(I + K_0^2)^{-1/2} \tag{2.51}$$

the Wronskian will be, after some algebra:

$$W(P, Q) = \frac{2\mu}{\pi}I \tag{2.52}$$

and the solution will formally be:

$$M(r) = P(r) + \int_0^\infty G(r, r')V(r')M(r') \tag{2.53}$$

and to first order

$$M(r) = P(r) + \int_0^\infty G(r, r')V(r')P(r'). \tag{2.54}$$

Now, we substitute in 2.54 the Green function 2.48, and P, Q from Eq. 2.51. Upon introducing the integrals

$$I_{ff} = \int_{r_0}^{\infty} f_0(r')V(r')f_0(r')dr' \tag{2.55}$$

$$I_{fg} = \int_{r_0}^{\infty} f_0(r')V(r')g_0(r')dr' \tag{2.56}$$

$$I_{gg} = \int_{r_0}^{\infty} g_0(r')V(r')g_0(r')dr', \tag{2.57}$$

the perturbed K-matrix will be:

$$K^{pert} = AB^{-1} \tag{2.58}$$

where

$$A = K_0 - \pi(I_{ff} - K_0 I_{gf} - I_{fg}K_0 + K_0 I_{gg}K_0)$$

$$B = I + \pi K_0(I_{ff} - K_0 I_{gf} - I_{fg}K_0 + K_0 I_{gg}K_0 \tag{2.59}$$

when the perturbing potential vanishes we recover the unperturbed form. The advantage of this form of the K-matrix over, for example, the treatment in Ref. [12] is that the poles are shifted with respect to the unperturbed poles. We will show in Ch. 4 how well this method works, compared to an R-matrix propagation, for positive and negative energies, for a complicated system like an electron in the field of HCO^+.

Chapter 3

Methods: vibrations, rotations and dissociative recombination

This chapter describes the methods we employ to treat vibrational motion and nuclear dynamics in general. Particular attention is paid to dissociative recombination reactions (in this chapter and Ch. 6). Sec. 3.2 shows how we obtain the electronic parameters adopted in the calculations, and it describes the different representations (adiabatic/diabatic) of the electronic states and their use. Symmetry-distortion effects, such as Jahn-Teller and Renner-Teller, are considered, as well as the way they can accelerate the dissociative recombination (DR) rate. A brief survey of frame transformation techniques is given in Sec. 3.3, while our treatment of the molecular dissociation is shown in Sec. 3.4. Our formulation can be adapted in principle to any kind of molecule, but some specific choices (especially the vibrational coordinates and the form of the model K-matrix) are tailored for HCO^+, which is the system we have studied in detail.

3.1   Introduction

The dissociative recombination (DR) of small molecular ions that collide with electrons plays an important role in interstellar diffuse and dense clouds, see Ref. [53] for a recent review on theory and experiment in this field. It is well known that these clouds constitute building material for new stars. The importance of DR cross sections

as parameters in star formation models, for such astrophysically relevant ions as H_3^+ and HCO^+, is one of the reasons why DR has been extensively studied in laboratory experiments [105]. For diatomic molecules the process is well understood and described theoretically [65, 89]. Until recently [94, 95, 143] though, theory was unable to model the DR process in triatomic ions, except in cases where a neutral dissociative state crossed the ionic Born-Oppenheimer surface in the Franck-Condon region, generating a rapid rate [143]. In triatomics, a key complication is that multiple vibrational and rotational degrees of freedom must generally be taken into account. Beyond the greater computational burden of treating more dimensions quantum mechanically, the addition of these new degrees of freedom can also lead to new conceptual issues, related to the degeneracy of vibrational or rovibrational levels in certain triatomic ions (e.g., in both H_3^+ and HCO^+). This can cause an intrinsic instability of the corresponding neutral molecules that forces them to distort away from the symmetric geometry.

Consider an incident electron that interacts with a closed-shell triatomic ion having a degenerate vibrational mode. If the symmetry group Γ of the resulting neutral complex has at least one degenerate irreducible representation, the electronic partial wave components with angular momentum $l > 0$ typically contain at least one such representation, whereby the corresponding electronic states of the neutral molecule are degenerate in the clamped-nuclei approximation. Due to the Jahn-Teller theorem [9, 115], this degenerate electronic state strongly interacts with a degenerate vibrational state of the Γ group. If the molecule is nonlinear, the interaction leads to the Jahn-Teller effect, a conical intersection, in which the two states have an off-diagonal coupling which is linear in the distortion coordinate. If the molecule is linear, the off-diagonal coupling of lowest order is quadratic, giving rise to a Renner-Teller [126] (glancing) intersection.

It has been well established in the literature that these distortion effects are a general characteristic of potential energy surfaces for polyatomic molecules, and taking them into account has explained many spectra and fast reaction rates. Conical intersections [20, 208] can generate a "funnel" effect that leads to rapid passage of a wavepacket from the upper surface to the lower surface, thus providing a preferred pathway for the reaction to occur.

In electron-induced reactions, electron capture can be followed by dissociation or autoionization of the recombined system. Since the degenerate electronic state causes the instability of the symmetric configuration, the recombined molecule quickly distorts away from the symmetry point to remove the degeneracy, after which the autoionization channel typically becomes energetically closed, and the molecule eventually finds a pathway along which it can dissociate (if there is an electronic state of the molecule which is open for dissociation). In a system for which no direct crossing of a neutral dissociative state with the ground state of the ion is present, this mechanism can become dominant, and it can still produce large DR cross sections. This is expected to be particularly true for molecules containing hydrogen. A schematic illustration of these two cases is shown in Fig. 3.1.

Recently Kokoouline and Greene [95] have demonstrated this occurs in $H_3^+ + e^-$ collisions. For HCO^+, a closed-shell linear ion in its ground state, the picture is similar. The lowest doubly-degenerate vibrational E states are coupled to the electronic states $E_1(np\pi)$ of the neutral system through the Renner-Teller interaction, resulting in a large probability for recombination.

Although the Renner-Teller coupling is well known, electron-molecule collisions where the coupling is present have not yet been studied until recently. This is possibly

due to the complexity of the problem because the molecule must be at least triatomic so that one has to treat three or four degrees of freedom simultaneously. In a recent study [126] McCurdy *et al.* have made an important step in understanding the role of Renner-Teller physics in collisions between the electron and the CO_2 molecule. The authors have employed a time-dependent framework to describe the nuclear motion of the negative ion CO_2^- formed during the collision. The nuclei move in the two-component $^2A_1$ and $^2B_1$ electronic complex potential corresponding to the doubly-degenerate $^2\Pi_u$ molecular state at linear configuration. The two components are coupled by the Renner-Teller interaction.

3.2   Ab initio surfaces

To treat the electronic degrees of freedom and the Rydberg state dynamics we work in the framework of multichannel quantum defect theory (MQDT). This allows us to treat Rydberg states of arbitrarily high principal quantum number, provided we can extract a few geometry-dependent quantum defect parameters from accurate *ab initio* quantum chemistry or scattering calculations. In our model we use a further simplification, imposing the energy independence of the quantum defects, a statement that we will show to be accurate, except possibly for the very lowest ($n = 2$ for HCO^+) states, which have considerable valence character.

In MQDT the information regarding the potential energy surfaces of Rydberg states is expressed in a compact and convenient fashion using an effective K-matrix. This can be derived from the Lippmann-Schwinger equation [141]

$$-\frac{1}{\pi}\underline{K} = \underline{V} - \frac{1}{\pi}\underline{V}\frac{1}{E - \underline{H}_0}\underline{K} \tag{3.1}$$
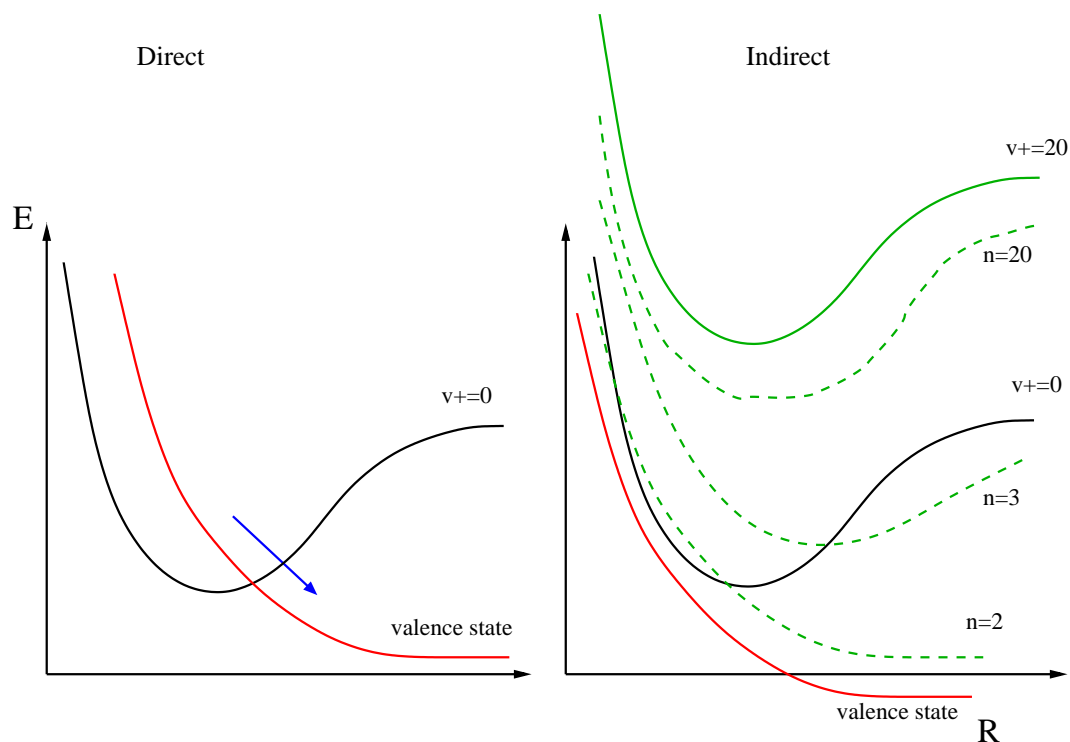
Figure 3.1: Schematic representation of direct and indirect DR processes. For direct processes a crossing of the ion (black curve) ground state and the neutral dissociative state (in red) leads to quick dissociation. For an indirect mechanism, in an adiabatic picture, the neutral dissociative state lies below the ionic potential and cannot lead to direct dissociation, since there is no classically-allowed Condon point for capture. The electron can be captured into a Rydberg state (dashed green curve) converging to an excited vibrational threshold (full green curve) and, through subsequent decay through the Rydberg manifold and additional vibrational excitation, it can find a dissociative pathway and give a high DR rate.

where $\underline{V}$ is a matrix that represents the electronic interaction between the electron and the ion, $\underline{H}_0$ is the ionic Hamiltonian. We can approach the solution of this equation perturbatively, and in the case in which $\underline{K}$ can be considered energy independent, as in the present case, it is sufficient to stop the perturbative expansion at first order, leading to

$$-\frac{1}{\pi}K_{i,j} = < \psi_i \mid V \mid \psi_j > +\mathcal{O}(V^2)$$
(3.2)

where i, j are two different electronic states. This matrix is usually multiplied by $-\pi$ in order to agree with the usual reaction matrix of MQDT [95]. Therefore the K-matrix corresponds to the matrix of diabatic (potential) couplings. It is possible to extract such quantities by fitting the adiabatic (Born-Oppenheimer) potential energy surfaces of the Rydberg states to a model K-matrix with off-diagonal couplings. It is important to have a diabatic description of the electronic states because when a conical (or Renner-Teller) intersection is present the different potential energy curves have a true crossing. In an adiabatic representation the couplings would be infinite, since in a Landau-Zener picture [101] the couplings are inversely proportional to the difference of the potentials between the two states. In a diabatic representation the couplings remain finite at every point.

The electronic dynamics is tackled calculating the Rydberg potential energy surfaces with quantum chemistry codes, and then fitting them to a model K-matrix to be used in a QDT calculation. Details of the procedure can be found in Sec. 6.2.1. Some new results for HCO Rydberg states potential energy surfaces, achieved using a Green function method, can be found in Ref. [49], they compare very well with our calculations.
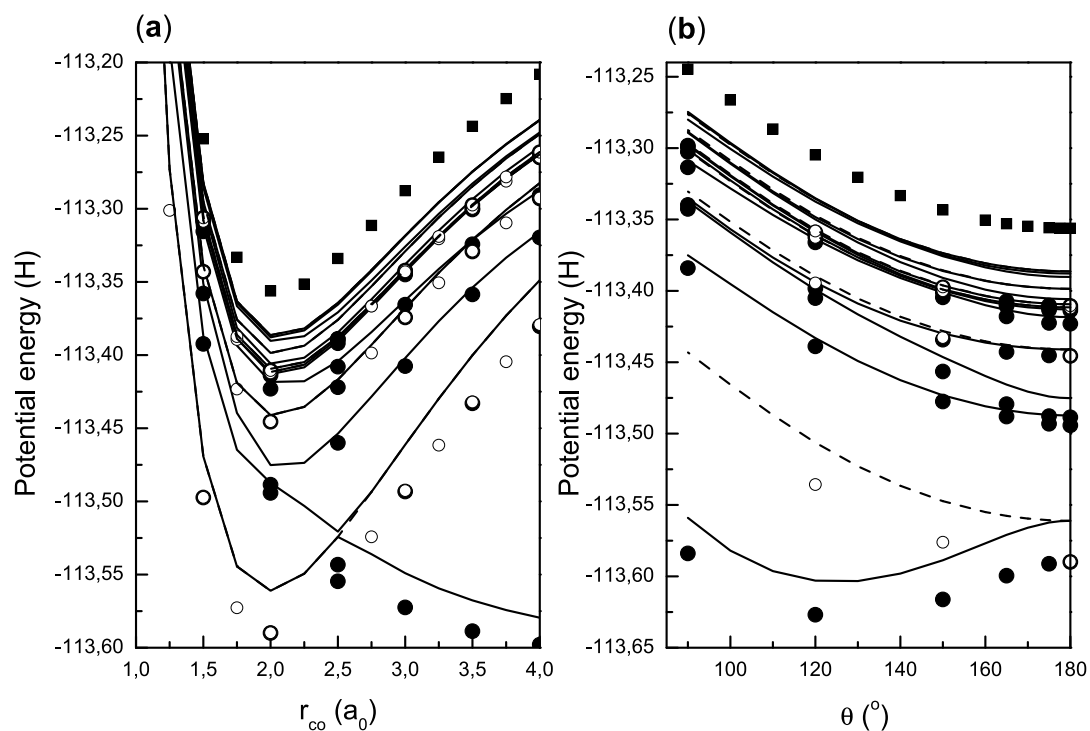
Figure 3.2: HCO$^+$ ground state ionic and HCO ab initio potential energy curves as a function of (a) CH stretch at the equilibrium $r_{CO} = 2.0877$ a.u. and $\theta = 180$ degrees and (b) bending at the equilibrium distances for CO and CH ($r_{CH} = 2.0$ a.u.). The filled symbols indicate MRCI potential energy curves of HCO states of A' symmetry, while open symbols are states of A" symmetry. The corresponding potential energy curves obtained using Koopmans' theorem are shown as solid and dashed lines respectively. From Ref. [104].

We have performed two calculations of DR in HCO$^+$, which we will call Model 1 and 2, that are described in detail in this chapter. The results are shown in Ch. 6. The main difference between the two models is the treatment of the Renner-Teller couplings, which are not included in Model 1, whereas they are present in Model 2.

We assume that the incident electron is initially captured into one of the neutral Rydberg states, which can be approximately characterized by the principal quantum number n, the orbital angular momentum l, and its projection on the molecular axis λ. In our model we have included only the $np\pi^{-1}$, $np\pi^{+1}$, $np\sigma$, $ns\sigma$ and $nd\sigma$ states. The symbols ±1 imply two opposite-sense electronic angular momenta associated with the different signs of λ. Linear combinations of the $n\pi^{\pm1}$ states give states $np\pi'$ and $np\pi''$, symmetric and antisymmetric with respect to reflection in the plane containing the molecular axis. The other three states are symmetric. These states were established in Ref. [104] to be the most important for DR, since they exhibit the largest dependence on the vibrational coordinates.

In the first model we have fitted our *ab initio* electronic surfaces to a K-matrix having the following structure:

$$
K(\mathcal{Q}) = \begin{pmatrix}
K_{s\sigma,s\sigma} & K_{s\sigma,p\sigma} & K_{s\sigma,d\sigma} & 0 & 0 \\
K_{p\sigma,s\sigma} & K_{p\sigma,p\sigma} & K_{p\sigma,d\sigma} & 0 & 0 \\
K_{d\sigma,s\sigma} & K_{d\sigma,p\sigma} & K_{d\sigma,d\sigma} & 0 & 0 \\
0 & 0 & 0 & K_{\pi^{-1},\pi^{-1}} & 0 \\
0 & 0 & 0 & 0 & K_{\pi^{+1},\pi^{+1}}
\end{pmatrix} , \tag{3.3}
$$

where $\mathcal{Q}$ represents all the vibrational coordinates.

The important characteristic of this model K-matrix is the absence of Renner-Teller coupling, which implies that the π-block is diagonal, while the sigma block is fully

coupled. Renner-Teller coupling was initially omitted because of the observed nature of the Rydberg states surfaces as a function of the bending angle, shown in Fig. 3.2. In particular it appeared to suggest that the Renner-Teller splitting was large for $n = 2$ states, but very small for all other Rydberg states. The higher Rydberg states are responsible for the capture of the electron in the DR process, therefore Renner-Teller coupling was thought to be uninfluential for the reaction rate. The fitting procedure is described in Sec. 6.2.1.

3.3   Frame transformation and adiabatic methods

The frame transformation technique, which has similarities to the adiabatic nuclei approximation (also called Chase [31] or infinite-order sudden approximation [147]) assumes that the timescales for electronic motion and vibrational/rotational motion are very different, as in the Born-Oppenheimer approximation. This would seem at first not to hold for very high Rydberg states, where the Rydberg electron is so slow that its motion has a period similar to a molecular vibration or longer. In fact, this approximation holds up very well for Coulomb systems no matter how high the principal quantum number n is. This is because the Rydberg state has an elliptic "orbit", therefore even for very high n the electron spends a large amount of time outside the ion core, and very little time inside. Effectively the speed with which the electron passes through the core is almost energy independent, due to the large Coulomb acceleration that the electron receives close to the ionic core, which is always much larger than the Rydberg state energy. For neutral systems this does not happen, and indeed close to threshold the frame transformation treatment is less accurate. See, however, Ref. [76] for e-N_2 scattering.

We treat the nuclear dynamics in a two-step adiabatic framework, using Jacobi coordinates. This two step process is dictated by the need to calculate many vibrational states for the ion, which a full three dimensional calculation (which we have carried out anyway to check our results) would not have allowed. The coordinates are chosen to mimic as much as possible the normal modes of the molecule, since this improves the adiabaticity of the curves, probably because the couplings between the modes are minimal. We had initially tried to represent this ion using hyperspherical coordinates, but the simple adiabatic picture failed completely. In H_3^+ [95] the hyperspherical coordinates are similar to the normal modes and the adiabatic approximation holds well. The variable R represents the CH distance, while R is the distance between the oxygen atom and the center of mass of the other two, which is very close to the CO distance. the angle θ is the acute angle between these two vectors:

$$R = r_{CH}$$

$$r = \frac{m_C r_{CO} + m_H r_{OH}}{m_C + m_H}. \tag{3.4}$$

The Hamiltonian in Jacobi coordinates for $J \neq 0$ reads [188]

$$H_V = -\frac{\hbar}{\mu_1 R^2}\frac{\partial}{\partial R}(R^2\frac{\partial}{\partial R}) - \frac{\hbar}{\mu_2 r^2}\frac{\partial}{\partial r}(r^2\frac{\partial}{\partial r}) - \frac{\hbar}{2}(\frac{1}{\mu_1 R^2} + \frac{1}{\mu_2 r^2})\frac{1}{\sin\theta}\frac{\partial}{\partial\theta}(\sin\theta\frac{\partial}{\partial\theta}) \tag{3.5}$$

$$H_{VR} = \frac{1}{2}[\frac{1}{\mu_1 R^2}(J_x^2 + J_y^2) + (\frac{\cot^2\theta}{\mu_1 R^2} + \frac{\csc^2\theta}{\mu_2 r^2})J_x^2 + \frac{\cot\theta}{\mu_1 R^2}(J_x J_z + J_z J_x)$$
$$+ \frac{\hbar}{i}\frac{1}{\mu_1 R^2}(\frac{\partial}{\partial\theta} + \frac{\cot\theta}{2})J_y] \tag{3.6}$$

where J_x, J_y, J_z are the Cartesian components of the total angular momentum operator. The need to include $J \neq 0$ states, even in the absence of rotational dynamics, is due to the fact that for a linear molecule the odd quanta of the bending vibrations are

present only for odd J. This means that considering only states arising from a $J = 0$ calculation would lead to neglecting the lowest vibrational excited state (01^10), the quantum numbers are illustrated in Tab. 3.1. In the calculations we include only $J = 0$ and $J = 1$ and neglect the rotational spacing.

We use a spline basis [11] to carry out the target vibrational calculations in all three dimensions, first solving the two dimensional $r - \theta$ problem and then carrying out the R-dependent calculation on the adiabatic curves obtained in the first stage. A schematic illustration of the molecule with the Jacobi coordinates we use and the adiabatic vibrational curves as a function of r_{CH} is given in Fig. 3.3.

The vibronic K-matrix is obtained through a two-step frame transformation. The first step consists in taking the overlap of the electronic K-matrix with the adiabatic CO-bending wavefunctions

$$K_{\Lambda\nu_r\nu_\vartheta,\Lambda'\nu_r'\nu_\vartheta'}(R_{CH}) = \left\langle \phi_{\nu_r,\nu_\vartheta} | K_{\Lambda,\Lambda'}(\mathcal{Q}) | \phi_{\nu_\nabla',\nu_\vartheta'} \right\rangle. \tag{3.7}$$

In practice this integral is done on the quantum defect matrix, $\underline{\mu} = \pi^{-1}\tan^{-1}\underline{K}$, since the K-matrix has poles.

3.4   Siegert states

In this first study, we have used Siegert (outgoing-wave) boundary conditions [80, 189, 190] in the C-H degree of freedom. This allows the description of outgoing dissociative flux, i.e. predissociation. If outgoing wave boundary conditions are imposed at a finite distance, which is possible for finite range potentials (or for long-range potentials as suggested in Ref. [162]), one can use an L^2 (square-integrable) basis set to represent the Siegert states. Using these boundary conditions, a quadratic eigenvalue
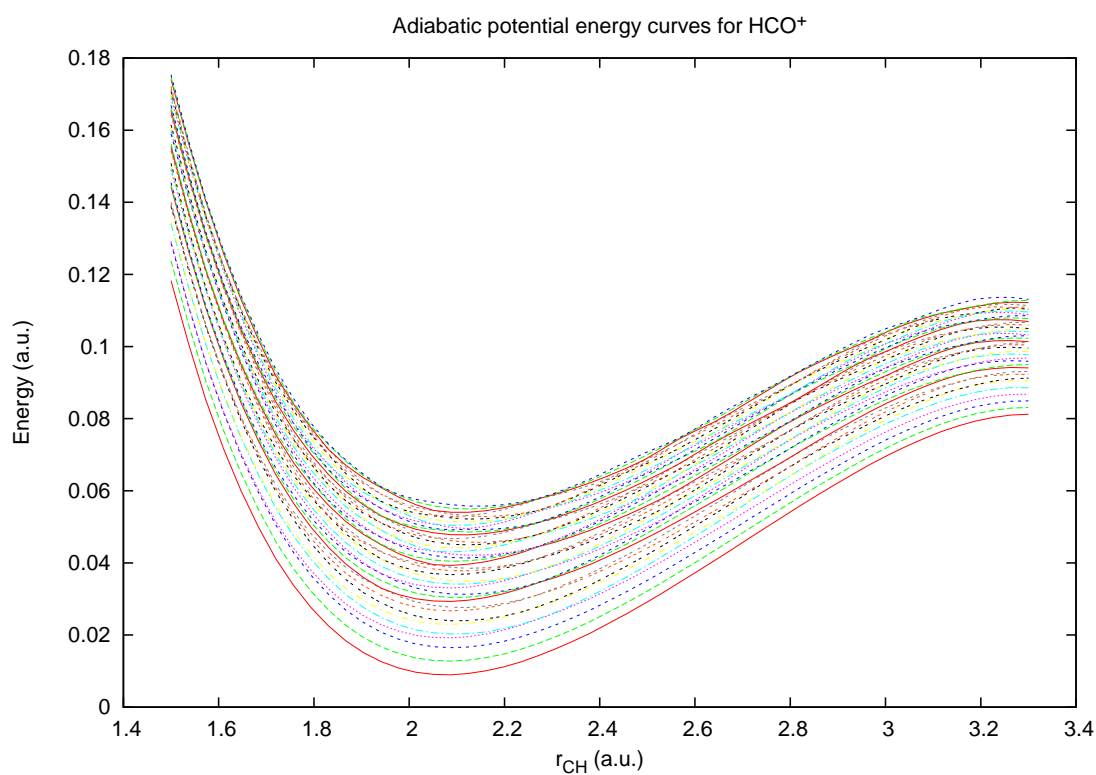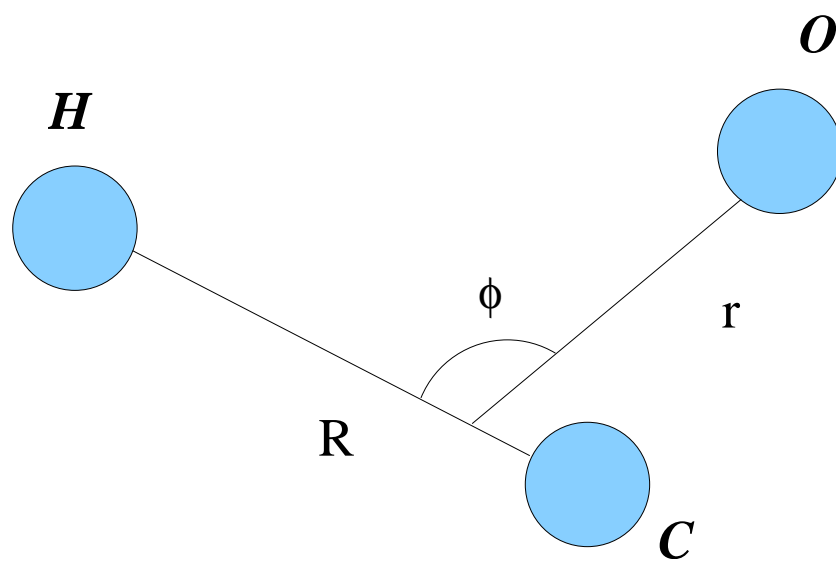
Figure 3.3: Top: Jacobi coordinates used to model HCO$^+$ vibrational dynamics, R is the adiabatic coordinate and it is coincident with r$_{CH}$. Bottom: adiabatic vibrational curves as functions of the r$_{CH}$ adiabatic coordinate. The figure represents the 40 lowest eigenvalues of the adiabatic Hamiltonian.

problem in k, the wave vector

$$(\underline{H} - ik\underline{L} - k^2\underline{Q})\vec{c} = 0 \qquad (3.8)$$

is recovered, where $\underline{L}$ is the matrix of the Bloch operator, and $\underline{Q}$ is the overlap of the basis functions. Eq. 3.8 can be solved iteratively. It can also be dealt with in one step by solving an eigenvalue problem of dimension twice the dimension of the basis space [190]. The second step in the frame transformation is then to use the Siegert states (ϕ_{ν_R}) to calculate the full S-matrix

$$S_{\Lambda\nu_r\nu_\vartheta\nu_R,\Lambda'\nu'_r\nu'_\vartheta\nu'_R} = \left\langle \phi_{\nu_R} | S_{\Lambda\nu_r\nu_\vartheta,\Lambda'\nu'_r\nu'_\vartheta} | \phi_{\nu'_R} \right\rangle . \qquad (3.9)$$

The channel elimination procedure [74], in which physical (exponentially decaying) boundary conditions are imposed in the closed channels is then applied. If we arrange the full S-matrix in open and closed channel partitions, we have [74]:

$$S^{phys} = S_{oo} - S_{oc}(S_{cc} - e^{-2i\beta})^{-1}S_{co} \qquad (3.10)$$

and we obtain the physical S-matrix (S^{phys}) of dimension $N_o \times N_o$ where N_o is the number of open channels [74]. The matrix β in Eq. 3.10 is diagonal with elements $\beta_j = \pi/\sqrt{2(E - E_j)}$ and it represents the Coulomb long-range phase parameter; E is the total energy, and E_j is the threshold of the $j-$th channel. When the Siegert states are used, the physical S-matrix will not be unitary and the difference from unitarity will be related to the DR cross section

$$\sigma(E_{el}) = \frac{\pi}{2E}\left(1 - \sum_{i=1}^{N_o} S_{i,i'}^{phys}(E)S_{i',i}^{\dagger phys}(E)\right), \qquad (3.11)$$

where $E_{el} = E - E_i$. This nonunitarity stems from the fact that the outgoing flux, which will be lost, is assumed to go exclusively into dissociative channels, which are

not included explicitly in the S-matrix. Notice that, following the definition of the Siegert states, their orthogonality relation involves a surface term, and therefore the frame transformation performed in Eq. 3.9 will have a similar surface term as in Eq. 6 of Ref. [80]. The results for this model are shown in Sec. 6.2.

3.5   Model Hamiltonian including the Renner-Teller coupling

Since the results obtained with the previous model K-matrix have not been satisfactory, we have built a new treatment that has as a focal point the inclusion of the Renner-Teller coupling. We also freeze the CO degree of freedom, and we include many vibrational angular momenta, instead of the two included in our previous treatment. The starting point of the present theoretical approach is the molecular Hamiltonian H of HCO, which we represent as $H = H_{ion} + T_e + H_{int}$, where H_{ion} is the ionic Hamiltonian, T_e is the kinetic energy of the incident electron, and H_{int} describes the electron-ion interactions. We assume that the ion is in its ground electronic state. H_{ion} and H_{int} depend on the four internuclear coordinates $\mathcal{Q} = \{R_{CH}, R_{CO}, \theta, \varphi\}$, where R_{CH} and R_{CO} are the C-H and C-O internuclear distances, θ is the bending angle, which is zero for linear configurations. The electronic energies are independent of the angle φ, which represents the azimuthal orientation of the bending.

As in Model 1 we consider 5 electronic states. Therefore, $H_{int} + T_e$ assumes a block-diagonal form with an infinite number of 5×5 blocks corresponding to $n = 2, 3, \cdots, \infty$, in addition to the continuum. In the derivation of the model we assume that there are no couplings between manifolds with different principal quantum numbers; later, the MQDT treatment will relax this constraint.

Since the only off-diagonal couplings included in our analysis are those among

the three np states, for simplicity we specify only these states in the formulas below.

The np sub-block of $H_{int} + T_e$ in the basis of the $np\pi^{-1}$, $np\sigma$ and $np\pi^{+1}$ states has the form [98]

$$H_{int}(\mathcal{Q}) = \begin{pmatrix} E_\pi & \delta e^{i\varphi} & \gamma e^{2i\varphi} \\ \delta e^{-i\varphi} & E_\sigma & \delta e^{i\varphi} \\ \gamma e^{-2i\varphi} & \delta e^{-i\varphi} & E_\pi \end{pmatrix}, \qquad (3.12)$$

where E_σ and E_π are the electronic energies of the $np\sigma$ and $np\pi^{\pm1}$ states at the linear ionic configuration; δ and γ are the real, non-Born-Oppenheimer coupling elements. We denote both the $(n\pi - n\pi)$ and $(n\pi - n\sigma)$ couplings as Renner-Teller (RT) couplings, whereas in some previous studies, only the former is denoted by this term. The couplings δ and γ depend on R_{CH}, R_{CO}, and θ. The diagonalization of $[T_e + H_{int}](\mathcal{Q})$ is accomplished by the unitary transformation matrix U [98]:

$$U = \frac{1}{\sqrt{2}} \begin{pmatrix} e^{i\varphi} & e^{i\varphi}w_- & e^{i\varphi}w_+ \\ 0 & \sqrt{2}w_+ & -\sqrt{2}w_- \\ -e^{-i\varphi} & e^{-i\varphi}w_- & e^{-i\varphi}w_+ \end{pmatrix}, \qquad (3.13)$$

with the abbreviations

$$w_\pm = \sqrt{(1 \pm \Delta/w)/2}; \ \Delta = (E_\sigma - E_\pi - \gamma)/2;$$

$$w = \sqrt{\Delta^2 + 2\delta^2}. \qquad (3.14)$$

When diagonalized, the Hamiltonian becomes

$$U^\dagger[H_{int} + T_e]U = \mathrm{diag}\{V_{\pi''}, V_\sigma, V_{\pi'}\}, \qquad (3.15)$$

where

$$V_{\pi''} = E_\pi - \gamma, \quad V_\sigma = (E_\sigma + E_\pi + \gamma)/2 + w,$$

$$V_{\pi'} = (E_\sigma + E_\pi + \gamma)/2 - w. \qquad (3.16)$$

The adiabatic potential energy surfaces $V_{\pi',\pi'',\sigma}(\mathcal{Q})$ are known from *ab initio* calculations (see Ref. [104] for a detailed description). From Eq. (3.16) we obtain

$$\gamma = E_\pi - V_{\pi''}\,, \quad w = (V_\sigma - V_{\pi'})/2\,. \tag{3.17}$$

Therefore, the matrices U in Eq. (3.13) and H_{int} in Eq. (3.12) are obtained from $V_{\pi',\pi'',\sigma}(\mathcal{Q})$.

3.6   Reaction matrix and O'Malley formalism for the DR cross section

Again here we employ multichannel quantum defect theory, and the first step is to construct the reaction matrix K. First we introduce the diagonal quantum defect matrix $\underline{\mu}$, whose nonvanishing elements μ_i are related to the diagonal element of the potential surface by $V_i = -1/[2(n - \mu_i)^2]$, where i is the electronic state index. Therefore, the diagonal form of the reaction matrix is directly obtained from the *ab initio* calculation.

The coupling δ in Eq. 3.12 is linear in θ for small θ. Correspondingly, the splitting between adiabatic electronic energies $V_{\pi''}$ and $V_{\pi'}$ is quadratic with respect to θ, and, therefore, the splitting between quantum defects $\mu_{\pi''}$ and $\mu_{\pi'}$ is also quadratic. This can be seen in Fig. 3.4, where $\mu_{\pi''}$ is almost constant because it has a different symmetry and is unchanged due to the Renner-Teller effect. The quantum defect $\mu_{\pi'}$ is approximately quadratic due to the Renner-Teller effect until $\theta \approx 50^o$, beyond which the linear approximation for $\delta(\theta)$ is not adequate. In a preliminary calculation we used such a linear dependence of $\delta(\theta)$, because we have found that we can use Eqs. 3.13, 3.14, 3.15, 3.16, and 3.17 and fit the model Hamiltonian accurately to the *ab initio* energies without the additional approximation of linearity of $\delta(\theta)$. The result of the preliminary
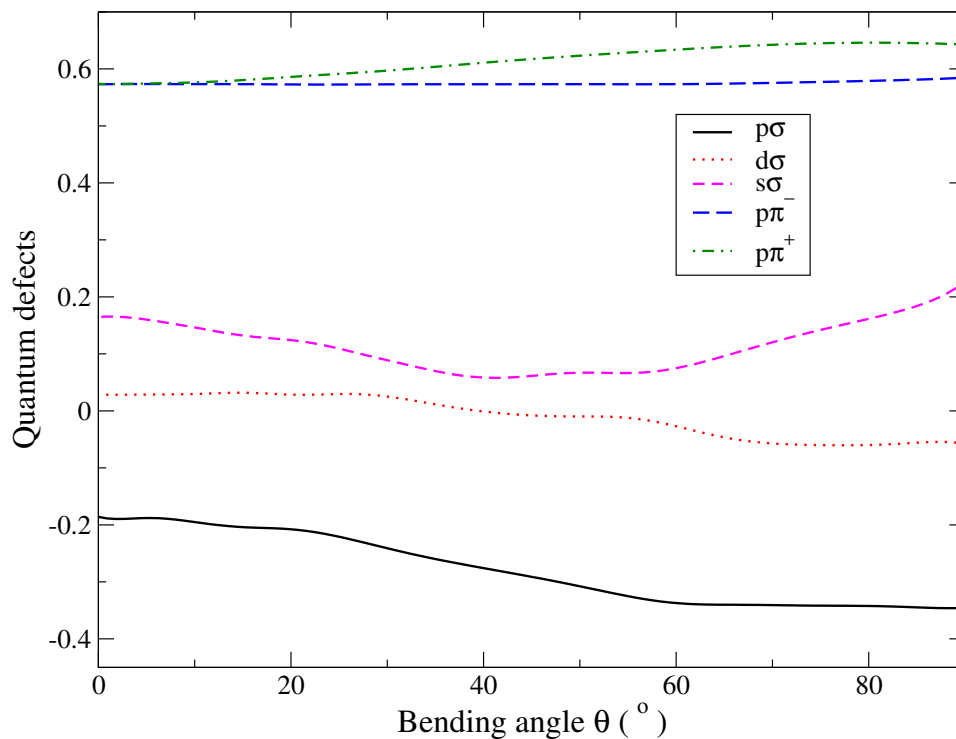
Figure 3.4: The eigenquantum defects of the electronic states included in the present study as functions of the bending angle θ for fixed $R_{CH} = 2.0$ a.u. and $R_{CO} = 2.0877$ a.u. Labeling the states with electronic momentum projection λ is an approximation and for large values of θ it is not appropriate. However, the four $s\sigma$, $p\sigma$, $d\sigma$, and $p\pi'$ states are always uncoupled from $p\pi''$ states for nonlinear geometries. In the absence of the non-diagonal matrix elements in Eq. 3.12 the $p\pi'$ and $p\pi''$ states would have the same quantum defects. The Renner-Teller parameters are completely determined by the geometry dependence of $p\pi$ and $p\sigma$ defects (Eq. 3.17). From Ref. [130].

calculation is consistent with the present calculation using the accurate fit to the *ab initio* energies.

The next step is to bring the reaction matrix into the representation of the Hamiltonian of Eq. 3.12. Since the transformation matrix U is known from Eq. 3.15, the K matrix in that representation reads

$$K = U \tan(\pi\mu)\, U^{\dagger}\ . \tag{3.18}$$

The matrices $\hat{\mu}$, $H_{int} + T_e$, K, U are diagonal for the $ns\sigma$ and $nd\sigma$ states. We used quantum defects from Ref. [104] with $n = 4$ for $ns\sigma$ and $n = 3$ for the other states. Figure 3.4 gives the quantum defects as functions of θ, with R_{CH} and R_{CO} fixed at the ionic equilibrium values.

Once the reaction matrix $K_{i,i'}$ is obtained, the DR treatment is along the lines of Refs. [94] with the following differences. We choose here the R_{CH} distance as the dissociative adiabatic coordinate. This assumption is justified because experimentally the H+CO channel is largely dominant at low energies. It has been long known that the CH+O channel is endothermic by 0.17 eV and could have an energy barrier, while the OH product is not observed (see Ref. [144] and references therein). Recently, branching ratios have been measured [57] for the DCO^{+} dissociative recombination, confirming that the D+CO channel is by far the dominant, with a dissociation branching ratio of 0.88. We keep the R_{CO} distance frozen at its ionic equilibrium value. This assumption was made to simplify the treatment but it could result in an underestimation of the DR cross section. In order to account for the CO vibration one might use the hyperspherical coordinates similar to Ref. [104], or else normal mode coordinates as in McCurdy *et al.* [126]. Although the CO bond is frozen, the Renner-Teller coupling physics is included
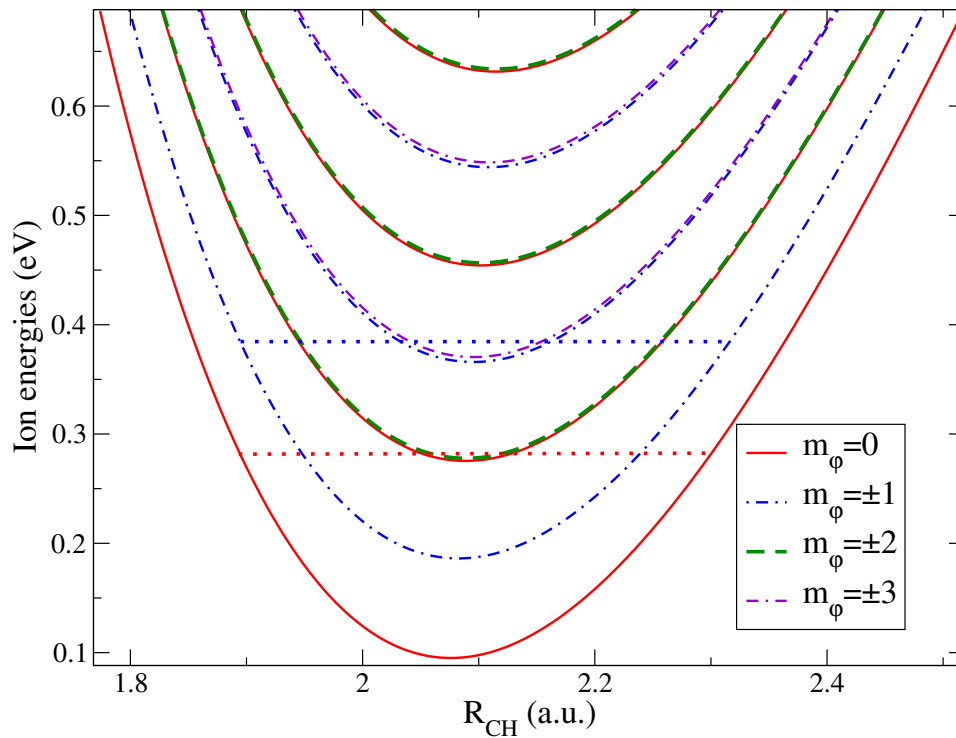
Figure 3.5: Several adiabatic potential curves for the HCO$^+$ ion are shown as functions of the R_{CH} distance for different projections m_φ of the vibrational angular momentum. The curves of the same color correspond to the vibrational states with the same quantum number m_φ but different L. The energies of the lowest vibrational states with $m_\varphi = 0$ and $m_\varphi = \pm 1$ are shown by two horizontal lines. From Ref. [130].

in our model; we show below that it does increase the DR cross section significantly. We will briefly address below the possible influence of the CO vibration.

Consequently, for every R_{CH} distance we calculate matrix elements of the "large" reaction matrix $\mathcal{K}(R_{CH})$

$$\mathcal{K}_{j,j'}(R_{CH}) = \langle \Phi_{m_\varphi,L}|K_{i,i'}(\mathcal{Q})|\Phi_{m'_\varphi,L'}\rangle_{\theta,\varphi}, \tag{3.19}$$

where $\Phi_{m_\varphi,L}(R_{CH};\theta,\varphi)$ are vibrational wavefunctions of HCO$^+$ parametrically dependent on R_{CH}, while R_{CO} is frozen. They are eigenfunctions of H_{ion} with eigenvalues $U^+_{m_\varphi,L}(R_{CH})$. Each index j in $\mathcal{K}$ can be represented as $\{i, m_\varphi, L\}$, where m_φ specifies the projection of the vibrational angular momentum on the molecular axis, while the index L distinguishes different vibrational states with the same m_φ. The rotation of the whole molecule is not considered. Fig. 3.5 shows the vibrational eigenenergies $U^+_{m_\varphi,L}$ as a function of R_{CH}.

It is informative to compare the ionic vibrational energies obtained in our simplified approach with the exact calculation accounting for all four vibrational coordinates [154]. We cannot compare the absolute values of the energies because the CO stretch is frozen, however, we can compare the energies of a few vibrational levels $\{v_1 v_2^l, v_3\}$ with respect to the energy $E = 0$ of the ground vibrational level $\{00^00\}$. Table 3.1 compares the vibrational energies obtained in this study with accurate results from Ref. [154]. The overall errors of the present calculated vibrational levels are about 12 % or less. Since the vibrational wave function error can thus be deduced to be of order $\sqrt{0.12} \approx 0.35$, whereby a conservative estimate of the error in our calculations of the final cross section would be of order 70%.

The matrix $\mathcal{K}(R_{CH})$ is used to obtain the potential curves $U_a(R_{CH})$ of HCO

$\{v_1 v_2^l, v_3\}$	Present calculation	Puzzarini *et al.*[154]
$10^0 0$	2933	3090.40
$01^1 0$	740	830.7
$02^0 0$	1460	1641.14
$03^1 0$	2200	2458.9
$04^0 0$	2925	3256.94

Table 3.1: The table compares the accuracy of the vibrational energies obtained in the present study that neglects CO vibrations with the "exact" calculation from Ref. [154]. v_1 indicates CH stretching, v_2 is the bending quantum number, v_3 is CO stretching and l the is vibrational angular momentum. Since the CO bond is frozen, we don't provide energies for excited v_3 modes. The overall energy error is about 12 %, which translates into an error of about 35 % for the vibrational wave functions. The energies are given in cm^{-1}. From Ref. [130].

as described in Ref. [94]. The curves in general have non-zero autoionization widths $\Gamma_a(R_{CH})$.

The potential curves $U_a(R_{CH})$ and their autoionization widths $\Gamma_a(R_{CH})$ are then used to calculate the DR cross section. The cross section is calculated in a manner similar to the procedure described in Refs. [94], with some adaptations. Specifically, we start from Eq. (5.19) of Ref. [142] for the cross section of the process of dissociative attachment of the electron to a neutral molecule, which applies equally to the dissociative recombination process considered here. The resulting approximation adapted to this situation reads (see Eq.6 of Ref.[94]):

$$\sigma_{DA} = \frac{2\pi^2}{k_o^2} \frac{\Gamma_a(R_{CH})}{|U'(R_{CH})|} |\chi_o^+(R_{CH})|^2 e^{-\rho(E)}. \tag{3.20}$$

Here $e^{-\rho(E)} \leq 1$ describes the survival probability, which could be less than unity if the system has a substantial probability to autoionize before it dissociates; k_o is the asymptotic wave number of the electron incident on vibrational level o of the target molecule. The distance R_{CH} is a dissociation coordinate understood to be evaluated at the Condon point, which depends on the total energy as well as the initial target vibrational level o; $\chi_o^+(R_{CH})$ is the initial vibrational wave function of the ion. The above formula is appropriate for the capture into a resonant potential curve that is energetically open for direct adiabatic dissociation. If the corresponding resonant state is closed, i.e. bound with respect to dissociation, it requires modification. To this end, we adapt Eq. (4.2) of Bardsley [16] to our present situation involving indirect DR. The indirect process proceeds via capture into a bound (typically Rydberg) state, which eventually predissociates. For a case involving a single incident electron partial wave (e.g. $p\pi'$, for definiteness) and a single ionic target state, the fixed-nuclei autoionization

width of the resonance potential curve will be denoted $\Gamma_a(R_{CH})$. Once the vibrational

motion in the resonance potential is quantized into a vibrational resonance level, with

radial wavefunctions $\chi^{\text{res}}(R_{CH})$, it should be remembered that only a subset o of the

target vibrational levels v will be energetically open, at any given total energy E. Each

resulting quantized resonance acquires a partial autoionization width $\Gamma_{a,o'}$ into an open

vibrational channel o', which is given approximately by

$$\Gamma_{a,o'} = |\int_0^\infty \chi_{o'}^+(R_{CH})\sqrt{\Gamma_a(R_{CH})}\chi^{\text{res}}(R_{CH})dR_{CH}|^2. \tag{3.21}$$

The sum of these is then the total resonance autoionization width (within this ap-

proximation, neglecting Rydberg level perturbations of the MQDT type, which could

sometimes produce complex, non-isolated resonances),

$$\Gamma_{a,\text{tot}} = \sum_{o'} \Gamma_{a,o'} \tag{3.22}$$

while the total linewidth Γ of this quantized resonance also includes its predissociation

partial linewidth, Γ_d: $\Gamma = \Gamma_d + \Gamma_{a,\text{tot}}$. In this notation, the contribution to the total DR

cross section will be the following, if only the ground vibrational level o of the target is

populated:

$$\sigma^{\text{res}}(E) = \frac{2\pi^2}{k_o^2}\frac{1}{2\pi}\frac{\Gamma_{a,o}\Gamma_d}{(E - E_{\text{res}})^2 + \frac{1}{4}\Gamma^2}. \tag{3.23}$$

Our model does not account for vibrational motion along the CO bond and,

therefore, positions of resonances cannot be compared directly with the experiment.

Moreover, the resolution in the available experiments is usually not sufficient to resolve

individual resonances. This suggests that we should average the cross section over

energy. Each energetically-closed ionic bound vibrational state c generates a Rydberg

series of resonances ϵ_{n_c}, numbered with the effective principal quantum number n_c. The

cross section averaged over the energy interval between two resonances with energies $E = \epsilon_n$ and ϵ_{n+1} is given by

$$\langle \sigma(E) \rangle = \frac{1}{\Delta_n + \Delta_{n+1}} \int_{E-\Delta_n}^{E+\Delta_{n+1}} \sigma(E') \mathrm{d}E', \quad \Delta_{n+1} = \frac{\epsilon_{n+1} - E}{2}. \tag{3.24}$$

Extending the limits of the integral to infinity, one can easily obtain the following:

$$\langle \sigma \rangle \approx \frac{2\pi^2}{k_o^2} \left(\frac{\Gamma_{a,o} \Gamma_d}{\Gamma \Delta} \right) \tag{3.25}$$

where the $\Delta = \Delta_n + \Delta_{n+1} \approx 1/n_c^3$. Note that the quantity in parentheses here approaches a constant at sufficiently high effective principal quantum numbers n_c in the relevant closed channel c, because each partial and total width in the parentheses of this formula should become proportional to Δ in this limit. The total cross section is then calculated by summing up the average contribution from all Rydberg states (a sum over closed ionic channels). In the limit where $\Gamma_d >> \Gamma_{a,\text{tot}}$, this gives

$$\langle \sigma \rangle = \frac{2\pi^2}{k_o^2} \sum_c |\langle \chi^{\text{res}}(R_{CH})| \sqrt{\Gamma_a(R_{CH})} |\chi_o^+(R_{CH})\rangle|^2 n_c^3. \tag{3.26}$$

The projection $M = m_\varphi + \lambda$ of the total angular momentum on the molecular axis O–C is a conserved quantity in our model. We calculate all the resonances and the cross section for all allowed values of M. Since we are considering only $s\sigma, p\sigma, d\sigma, p\pi', \pi''$ quantum defects and the initial ion is in its ground state $m_\varphi = 0$, the only possible values of M for the final state are 0 and ± 1. Resonance energies and widths are of course dependent only on $|M|$. Finally, we obtain for the cross section:

$$\langle \sigma^{total} \rangle = \langle \sigma^{M=0} \rangle + 2\langle \sigma^{M=1} \rangle. \tag{3.27}$$

The results from this model are shown in Sec. 6.3.

Chapter 4

Results: electron scattering, small molecules

4.1   Introduction

The approach developed in sections 2.2-2.3 is now tested in calculations of electron scattering by N_2 and CO_2, classic benchmarks in this field [120, 139, 156], because their elastic cross sections exhibit striking features that can be challenging to reproduce. These first results were published in Ref. [192]. We have moved to larger target molecules, specifically SF_6, XeF_6 and C_{60} fullerene (which is not presented here), to understand how well our approach scales for these large systems. These results are in sections 4.3.2-4.4.2. Photoionization calculations are described in Sec. 4.4.

4.2   Computational Details

Three-dimensional integrals are expensive to calculate in general so it is highly desirable to minimize the time spent in their calculation. For the sectors that do not contain a nucleus it is possible to use just 4 Gauss-Legendre points of integration in each coordinate, since doubling the number of points changes the calculated eigenphase shifts by only about 10^{-6} radians, while increasing the computation time by approximately an order of magnitude. Particular caution has to be observed when integrating over sectors

that contain a nucleus. We have found it important in general to have a finite element vertex on each Coulomb singularity, in order to obtain correct results, and to use more integration points. In these sectors we use 20 integration points in each dimension since we found that the convergence of the phase shifts in this case is, as in the previous case, about 10^{-6}. It is important also to provide sector boundaries near the K-shell radius for each atom in the molecule, since close to the nucleus the wavefunction varies rapidly. A fine grid is needed to represent the wavefunction oscillations near the nuclei, otherwise the phase shifts for the lowest, penetrating partial waves will be unconverged.

The sparse structure of the finite element matrices (see Fig. 4.1) can be exploited with great advantage from the beginning. No matter how the grid is defined, each basis function has matrix elements with at most 216 functions. This allows us to know the sparsity pattern of the matrix Γ in Eq. 2.8 (which we show again here for convenience)

$$\underline{\Gamma}\vec{C} = 2(E\underline{Q} - \underline{H} - \underline{L})\vec{C} = \underline{\Lambda}\vec{C}b \tag{4.1}$$

in advance and store just the nonzero elements, with a reduction in memory cost of approximately two orders of magnitude. This economy is crucial to allow us to perform three dimensional calculations in the first place.

The dimension N of the eigensystem in Eq. 2.8 is, for CO_2, of the order of 40000, whereas for the open subspace it is only 100 or less. N increases rapidly with the complexity and spatial extension of the molecular potential, but the sparsity of the matrices is high (about 0.5% full for $N \sim 40000$), and it increases with the dimension of the system. To solve the linear system in Eq. 2.11 we use direct sparse LU factorization solvers (SuperLU [87] at the beginning, now more extensively the Pardiso [168] solver). We have tried in the past to use iterative methods, such as biconjugate gradient [68]

, with different preconditioners to speed up the solution of the linear system. The one we have found to work best has been an incomplete Choleski factorization, which reduces drastically the number of iterations with respect to a diagonal preconditioner, the $\underline{\Gamma}$ matrix in Eq. 2.11 is not, in fact, diagonally dominant. Iterative methods are slower than direct factorization: in the tests we have performed normally the direct method is faster by an order of magnitude, but they are convenient if there are memory limitations. Since the factorization of a sparse matrix does not preserve the sparsity pattern, the factorized matrices present storage problems, since a fill-in factor of around 10-15 is common for these systems. We have decided to not use iterative methods since our linear system is often ill-conditioned and in these cases reaching convergence is very difficult, while direct methods always achieve the correct solution. This code therefore needs a large amount of memory for large target calculations, for which we have used Opteron 64-bit workstations with great success.

4.3   Results

In the first few calculations we show here, also published in Ref. [192], we have used an adjustable parameter in the polarization potential of Eq. 2.20, which here is used both at short and long distances:

$$V_{pol} = -\frac{1}{2r^4}[\alpha_0 + \alpha_2 P_2(\cos\theta)][1 - e^{-(\frac{r}{r_c})^6}]. \tag{4.2}$$

It is appropriate to carry out the expansion up to these first two terms, and neglect the rest of the dipole polarizability tensor, since the target molecules for which this potential is used are either linear or approximately so. Here r_c is a distance parameter comparable to the range of the target charge distribution. When high accuracy is
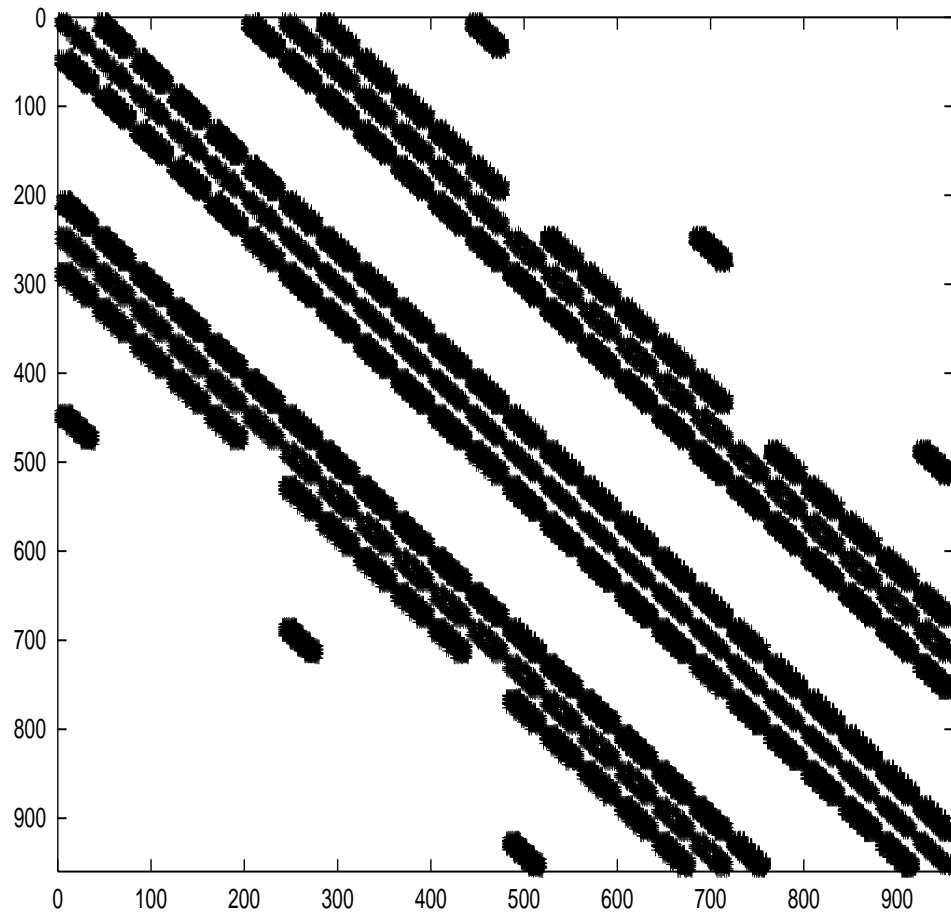
Figure 4.1: Structure of the finite element matrix Γ for a small test case of dimension 900. Notice the great sparsity of the matrix, which increases with the dimension of the matrix. From Ref. [192].

needed for resonance positions in some applications, r_c can be determined empirically [139] to reproduce the energies of one or more resonances of interest. In the calculations for N_2, CO_2 and HeH we used this simple adjustable potential instead of the more sophisticated and *ab initio* DFT potential described in section 2.2.3. This allows a tuning of the resonant features, if needed for particular purposes, but it is detrimental of the predictive power of the approach. In the calculations of Sec. 4.3.2 and following, we use the DFT polarization potential.

The strong and narrow Π_g resonance at 2.4 eV in N_2 is reproduced in our calculations at the right energy, provided we use a physically reasonable cutoff radius $r_c = 2.8$ a.u. for the polarization potential. In Fig. 4.2 are shown the results. Other theoretical studies of this resonance, definitely one of the most studied in electron-molecule scattering, can be found in Refs. [85, 137, 202], where exact treatments of exchange are performed. The resonance is reproduced also at the static exchange level (without using a long range polarization potential), but at an energy of 5.4 eV.

For CO_2 the main feature in the total elastic cross section is a Π_u resonance at 3.8 eV. To reproduce it at the correct energy we have to tune the polarization cutoff radius to 2.4 a.u.. This feature is present also at the static exchange level, at 8 eV. It should be noticed that in calculations made using an exact form of static exchange this resonance lies at 6 eV [63, 118, 134, 156]. The polarization dependence becomes much more pronounced than in N_2, as one expects from the larger spatial extension, the larger number of electrons and the greater asymmetry of this molecule. The scattering cross section for this system is shown in Fig. 4.3 . Fig. 2.2 shows how the polarization potential of N_2 is appreciable just outside the region where the main part of the electronic density is located. Therefore the value of the cutoff radius for the polarizability potential, which

is the only adjustable parameter in the model, is reasonable. The results are always in good agreement with previous theory, as shown in the figures.

The present calculations have been performed for the molecular targets only at their equilibrium distances. Vibrational effects tend to broaden these resonances in experimental elastic scattering cross sections, and they also give rise to more structured resonance peaks, which are not considered in this work.

The values of the polarizabilities used in these calculations are [139] $\alpha_0 = 11.89a_0^3$ and $\alpha_2 = 4.19a_0^3$ for N_2 and [102] $\alpha_0 = 17.9a_0^3$, $\alpha_2 = 9.19a_0^3$ for CO_2. It should be pointed out that accurate static polarizability coefficients α_0 and α_2 in Eq. 2.20 can also be extracted from *ab initio* calculations, although to get the correct values, extremely diffuse basis sets have to be used. Generally, the low-lying shape resonances present in these small molecules are spatially highly localized, which allows the radius of the R-matrix box to be kept small, around 8 to 14 a.u. for the present calculations.

In the case of the third neutral molecule that we present here, ethylene, the situation is more complicated. Since the target is now nonlinear it is more difficult to describe in a discrete basis set and it is more expensive computationally to calculate the scattering cross section. Nevertheless we are able to reproduce the features of the elastic cross section for this molecule. We find good agreement with the energies of the resonances and with the overall cross section magnitude, compared with previous theory and also experimental data, although the vibrational effects again tend to broaden the resonance peak.

It should be noticed parenthetically that if we neglect exchange altogether in calculations for all of the molecules presented here, the cross sections are qualitatively wrong, with resonances far lower in energy than the experimental ones and in the wrong

symmetry channels. This is due to the fact that some of the target electrons are not bound anymore in the resulting potential without exchange, because the static potential is not attractive enough. For example, in electron scattering from N_2 the Π_g resonance at 2.4 eV is recovered at 5.4 eV for a static exchange calculation in our model potential. Using only the static potential, there will be a Σ_g resonance around 2 eV, which is due to the σ_u electrons of the target being above the ionization threshold. The exchange potential is basically an attractive potential (local in our model), so adding it to the static potential produces the correct number of bound states for the target; consequently the scattering resonances are generated by capture of the electron in truly unoccupied molecular orbitals of the target. A more systematic study of the behavior of the cross sections, when different parts of the potential are neglected altogether, can be found in Ref. [102].

4.3.1   Quantum defect calculations

It has been shown [186] that use of a local density approximation can often be effective in calculating molecular quantum defects, for bound or scattering states, for small closed-shell target molecules. It is possible to calculate quantum defects from a scattering calculation carried out near zero energy. The key step is to diagonalize the K-matrix

$$K_{ii'} = \sum_\alpha U_{i\alpha} \tan \pi\mu_\alpha U^T_{\alpha i'} \tag{4.3}$$

and then utilize the relationship between the quantum defect and the scattering phase shift [74, 169],

$$\delta_\alpha = \pi\mu_\alpha. \tag{4.4}$$
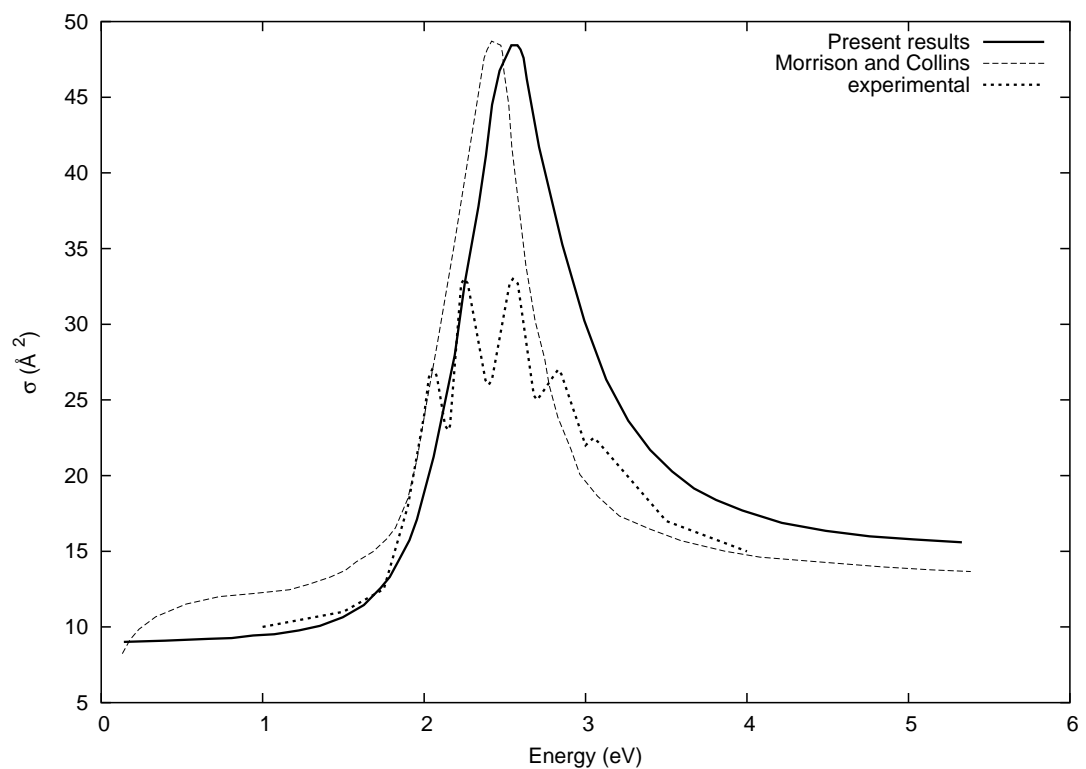
Figure 4.2: The integrated elastic cross section versus energy for electron-N_2 scattering, is compared to the theoretical results of Morrison and Collins [139] and to the experimental cross section of Kennerly [90]. From Ref. [192].
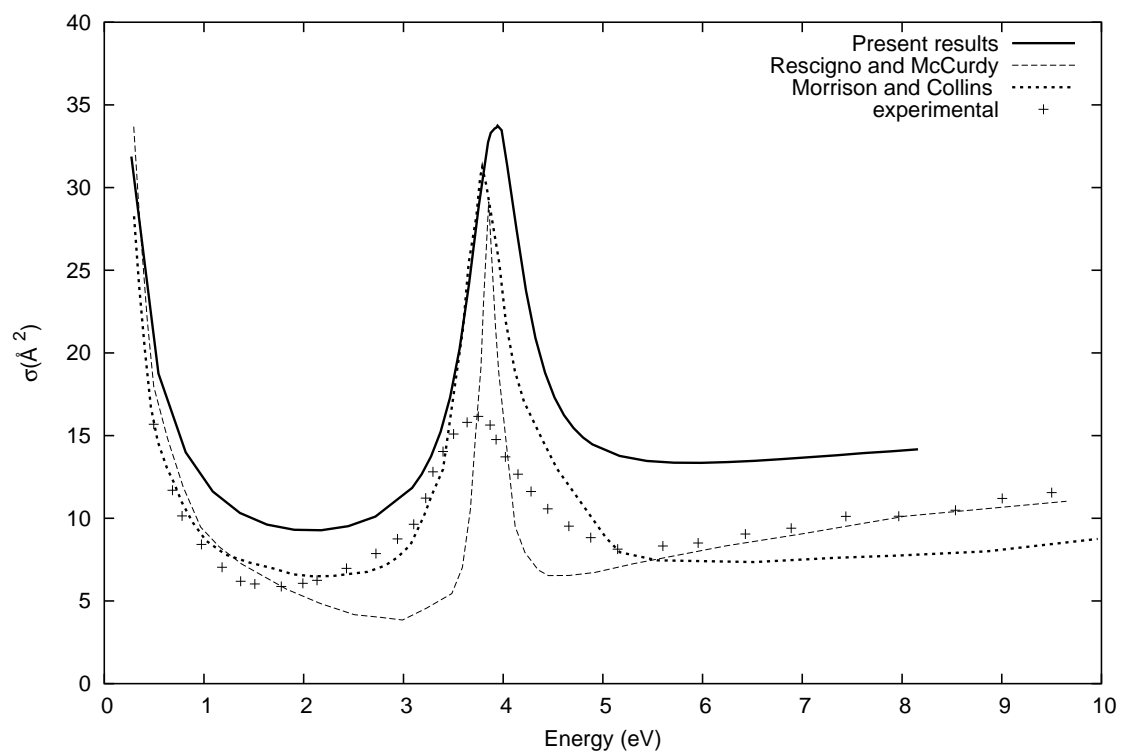
Figure 4.3: The integrated elastic cross section for scattering of electrons from CO_2 is shown as a function of the incident electron energy. The present results are compared with previous theory from Rescigno *et al.* [156] and Morrison and Lane [102], whereas the experimental results are those of Szmytkowski *et al.* [182]. From Ref. [192].
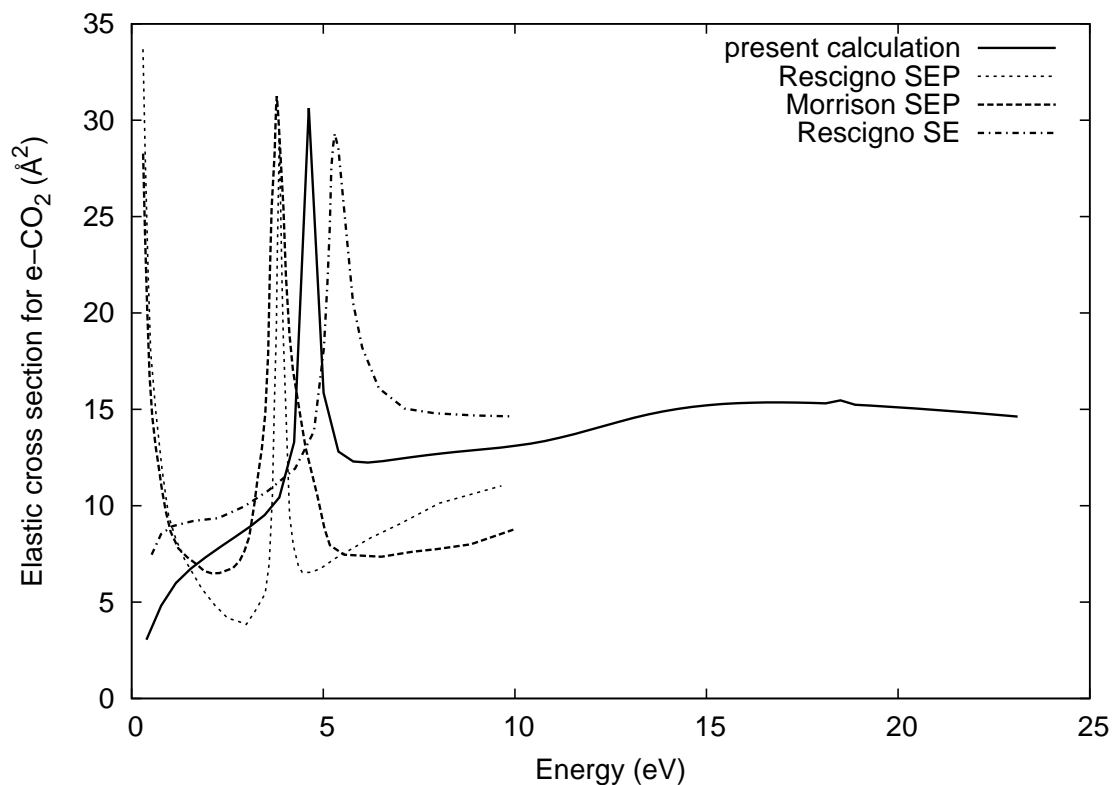
Figure 4.4: The e-CO$_2$ elastic cross section at low energies using our completely *ab initio* potential. The prominent structure is the well-known π_u resonance which, in experiment, has been found at 3.8 eV. Often the resonances we calculate with our approach are roughly 2-2.5 eV higher if compared to Fig. 4 in Ref. [192]. Our results are compared with those of Rescigno *et al.* [156] (exact static exchange and exchange plus polarization) and Morrison and Collins [139] (model exchange plus semiempirical polarization). The resonance width is comparable to the SEP results of Rescigno *et al.*. From Ref. [191].
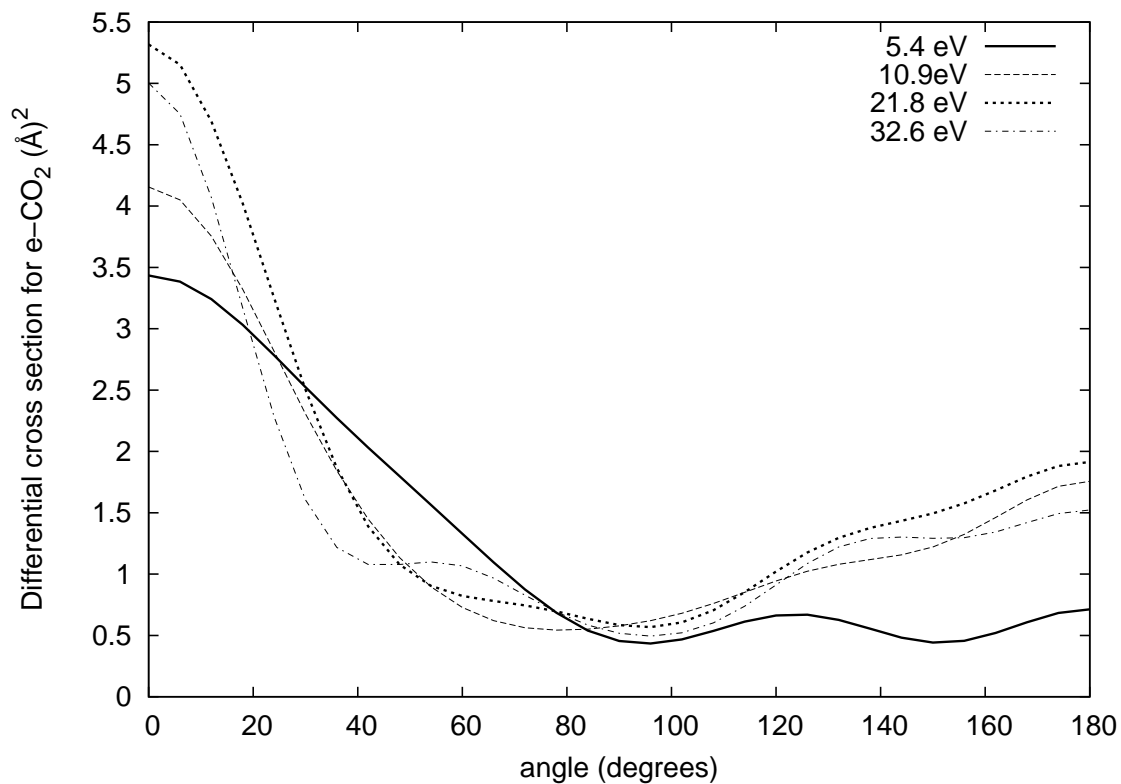
Figure 4.5: The e-CO$_2$ differential cross section is shown as a function of scattering angle at four low electron impact energies. The results can be compared with those of Refs. [63, 64, 138, 156]. From Ref. [191]. We calculate this differential cross section, averaged over molecular orientations, using the formalism derived in Ref. [41].
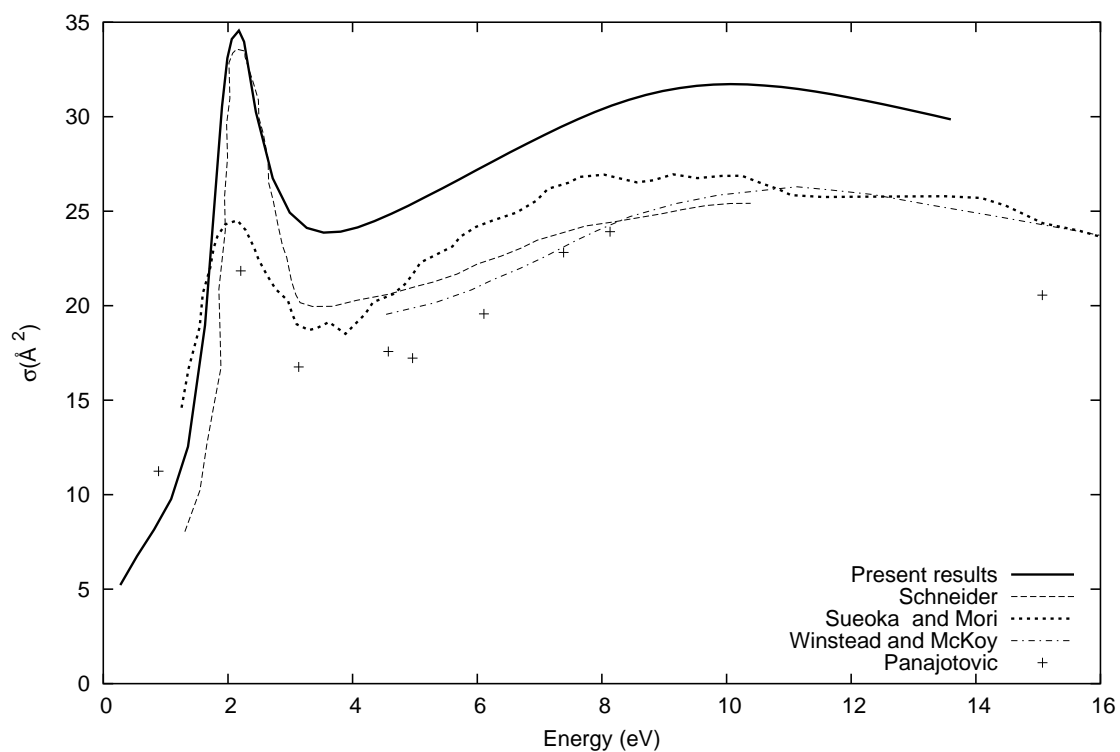
Figure 4.6: The integrated elastic cross section for electron-C_2H_4 scattering shown as a function of energy, is compared to previous theoretical results of Winstead *et. al.* [205] and of Schneider *et. al.*. [167] The experimental results are the ones of Panajotovic *et. al.* [145] and of Sueoka and Mori [179]. From Ref. [192].

Accordingly, quantum defects can be extracted from electron-scattering calculations at positive or negative energies if energy-dependence of the parameters is investigated. These quantum defects can then be used to determine the Born-Oppenheimer potential energy curves of the Rydberg states converging to the various ionization thresholds through the Rydberg formula, Eq. 2.35. These potential energy curves can then be exploited through MQDT techniques, to extract dynamical information to model, for example, dissociative recombination [95], as we show in Ch. 3. Here we show an example of how well this approach works for a simple diatomic molecule.

We compare our results to the work of Sarpal and Tennyson [163] which made no approximation about the nature of the electron-molecule potential, and the agreement is generally very good. The quantum defects represented in Fig. 4.7 are the most important ones, partial waves ($l > 2$) having very small phase shifts at the low energies considered here. In electron scattering from an ionic target we must account for the fact that heteronuclear target molecules like HeH^+ have a dipole moment, so we must transform from the center of mass frame to a new frame defined by the center of charge (the proton in this case), which allows us to match to simple Coulomb functions at the boundary of the box. Otherwise multipole potentials have to be included in the external region.

4.3.2 XeF_6

The xenon fluorides are among the few stable molecules formed by this noble gas. XeF_6 has a structure that can be seen as a distorted octahedron [28]. The distortion is commonly ascribed to the lone pair of electrons that remains on the xenon atom, after it has formed 6 bonds with the fluorine atoms. Since this system includes a heavy
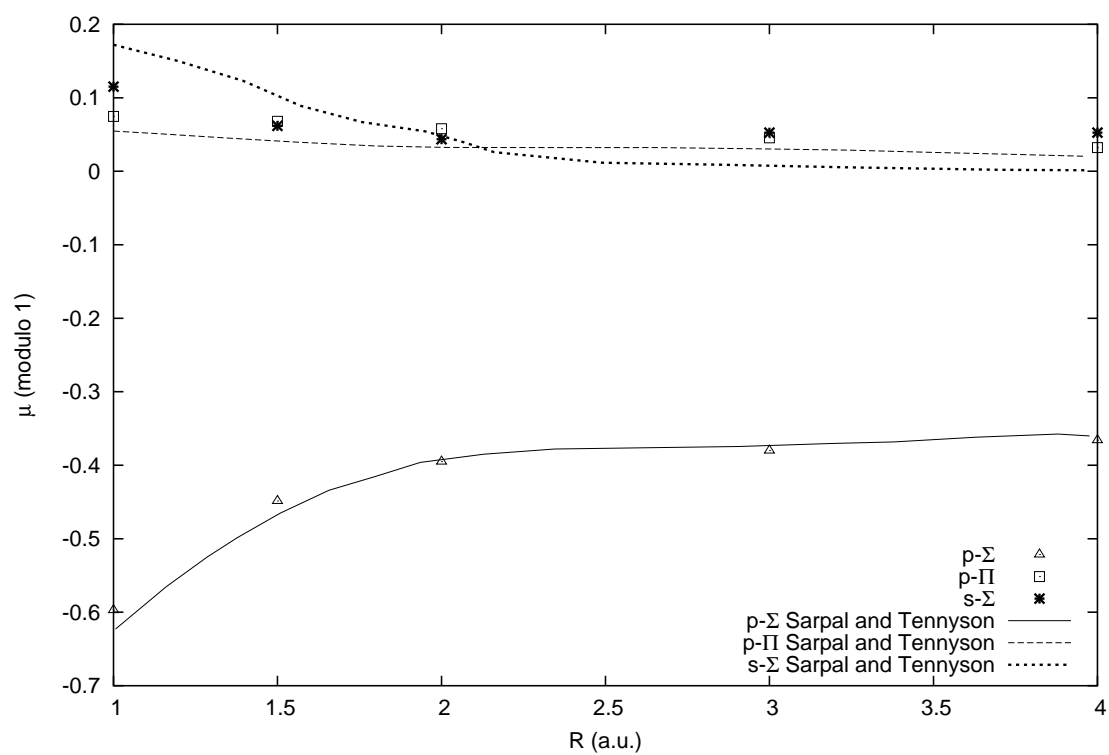
Figure 4.7: Our calculated eigenquantum defects at an energy of 0.1 eV for the HeH molecule calculated with our method are compared with those of Sarpal and Tennyson [163] as a function of the internuclear distance R. From Ref. [192].

atom, it is hard to treat with more sophisticated methods because of the large number of electrons and consequently the large basis set requirements. Our approach instead scales roughly the same way as for SF_6. Notice that relativistic effects could be significant in Xe, see for example Ref. [28], but we neglect them altogether.

For convenience, and because there are no experimental data to compare to for this system, we have distorted the molecule back to octahedral geometry. The elastic cross section results are shown in Fig. 4.8. The resonant structures are similar to SF_6, since the two molecules have similar electronic structure and, in this case at least, the same geometry.

The distortion of the octahedral cage could lead to interesting effects on the resonances that might be worth exploring in the future. Many highly coordinated compounds show "cage" effects [39] in their electronic structures and interactions with continuum electrons. Molecules like C_{60}, which have an internal cavity and therefore a potential energy barrier in the motion of an electron between the internal and the external regions, can trap electrons in this kind of resonance. A detailed study could uncover interesting properties. In cluster environments, caging effects have been measured for heavy particles, for example in photoionization of negative ions in a CO_2 cluster [146]. Likewise these effects could be pronounced for an electron as well, leading to a sensible modification of single-molecule shape resonances. Through the trapping of an electron inside the cage, it might be possible to extend the lifetime of the diffuse anionic states, while the continuum electron scatters off the cluster cage. These phenomena will be reserved for future studies using the same approaches adopted here for single molecules.

A spatial map of the wavefunction, calculated as described in Sec. 5.1.3, for the lowest energy resonance is shown in Fig. 4.9, as a cut through the $x - z$ plane of the

molecule, which shows clearly the positions of the Xe nucleus at the center and the four fluorine atoms in the plane around it, with the areas of greater electron density shown in blue and yellow.

4.4   Photoionization

In photoionization studies, it is possible to detect resonances of the ion that couple to different initial states by ionizing different electrons in the molecule, something that cannot be done in scattering experiments. We have studied two molecules in particular, CO_2 and SF_6, described in detail below. All the cross sections are multiplied by the number of degenerate electrons of that symmetry, as described in Sec. 2.3. Here, as in the previous electron scattering studies, we assume a fixed geometry for the molecule, namely the equilibrium geometry, and neglect vibrational effects altogether. This leads to resonances that are sharper than in experimental data, where the effect of vibrational averaging is important. The cross sections are summed over the different possible molecular orientations, as shown in Ref. [41]. The purpose of these calculations is to show their feasibility and predictive power within our approach, detailed analysis of the spectra and their resonances have been discussed previously in the literature and will not be examined in depth here.

4.4.1 CO_2

We have tested our photoionization approach first for CO_2, and our results are in Fig. 4.10. The ground electronic state of CO_2 is $^1\Sigma_g$ and therefore when an electron is extracted, in the single electron approximation, from a molecular orbital, the symmetry of the residual molecular ion will be the same as that of the orbital the ionized
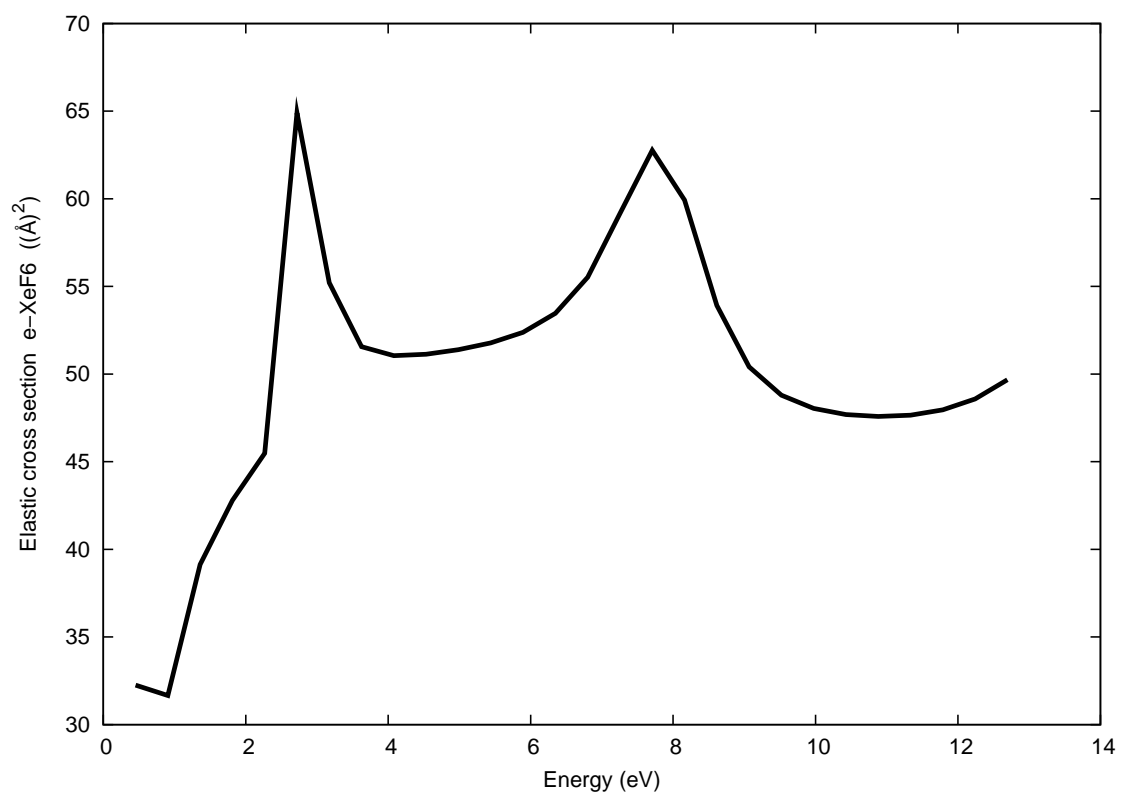
Figure 4.8: The integrated elastic cross section for e-XeF$_6$ shown as a function of energy.
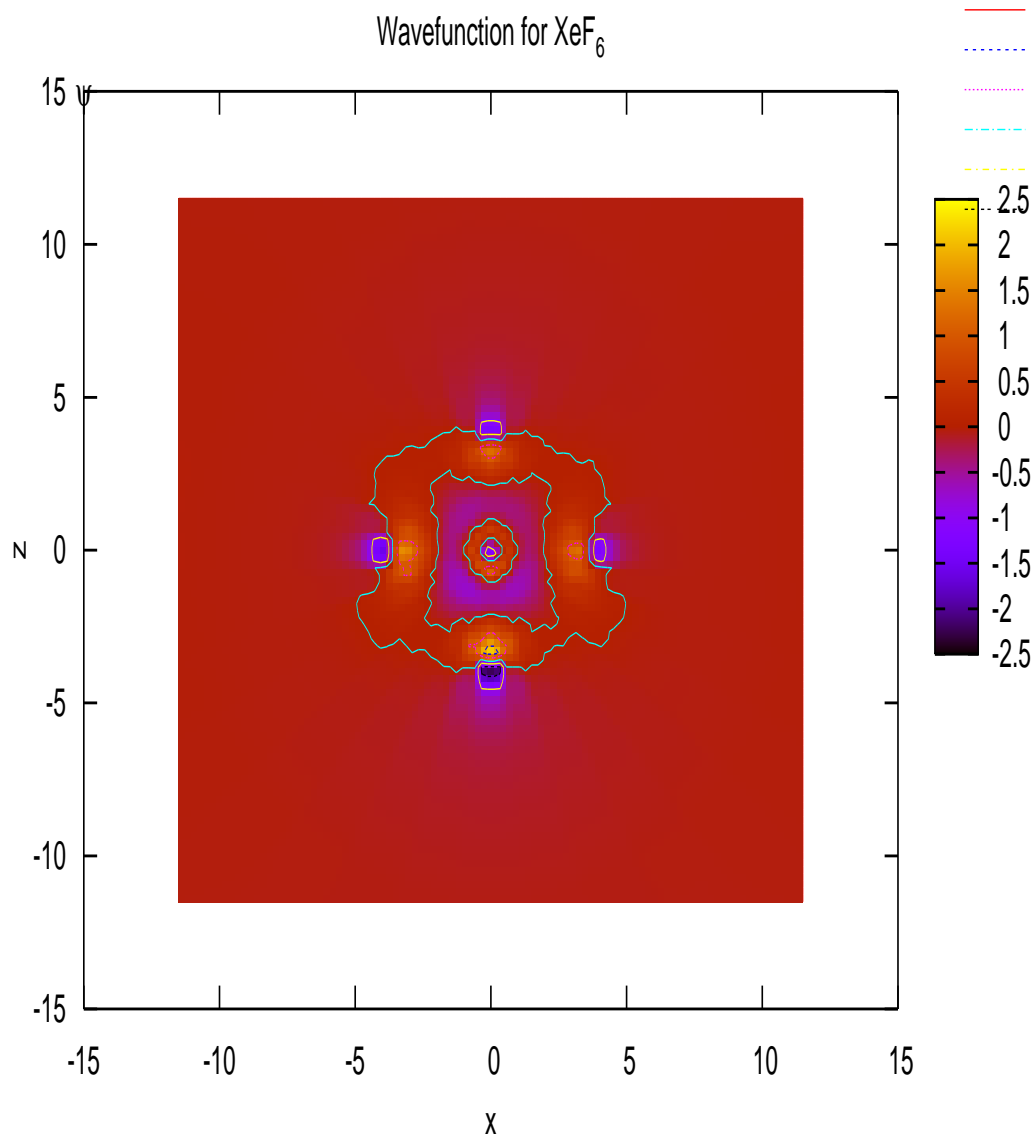
Figure 4.9: Resonance wavefunction map for e-XeF$_6$, for the resonance at 2.5eV. Plotted is the largest eigenvalue of the time-delay matrix. At the center it is visible the Xe atom, whereas the four fluorines in the plane are located at 90 degrees with respect to each other, between the yellow and blue areas, since the wavefunction has a node at the nuclei.

electron occupied in the target molecule. The curves in Fig. 4.10 are labeled accordingly. Comparing with the results of Ref. [119] we see quite good agreement, although the resonance position is shifted about 0.8eV lower, due to the different description of exchange in the two models, and also the fact that our calculations include polarization. It is possible to see that the σ_u resonance at a kinetic energy of 21.8 eV couples to the gerade initial orbitals but not to the π_u orbital, since the dipole matrix element is zero in that case by symmetry. A detailed analysis of CO_2 photoionization can be found in Ref. [119].

4.4.2   SF$_6$

In the case of SF_6 we have also done both a scattering and photoionization study. The scattering cross section for e+SF$_6$ is shown in Fig. 4.11 and it compares favorably with a more sophisticated theoretical model [59] and experimental data [91], both for the overall magnitude and for the resonance position, which are as usual somewhat shifted to higher energies with respect to experiment. The photoionization study is, at the moment, preliminary, but it nevertheless reproduces correctly many of the features present in experiment and other theoretical studies [207]. Our results are shown in Fig. 4.12. The main differences between our results and Ref. [207] are the sharp high energy (20 eV kinetic energy of the electron) resonances in the $5t_{1u}$ and $4t_{1u}$ channels, which probably will be smeared out to a larger final width by vibrations. These resonances are prominently featured in the calculations of Ref. [112] as well, where a model potential similar to ours is used, suggesting that this is a model-dependent feature. SF$_6$ has 70 electrons and 35 filled molecular orbitals, therefore here we show data for the 7 orbital groups highest in energy. The ionization energies of these orbitals are reported in Ref.

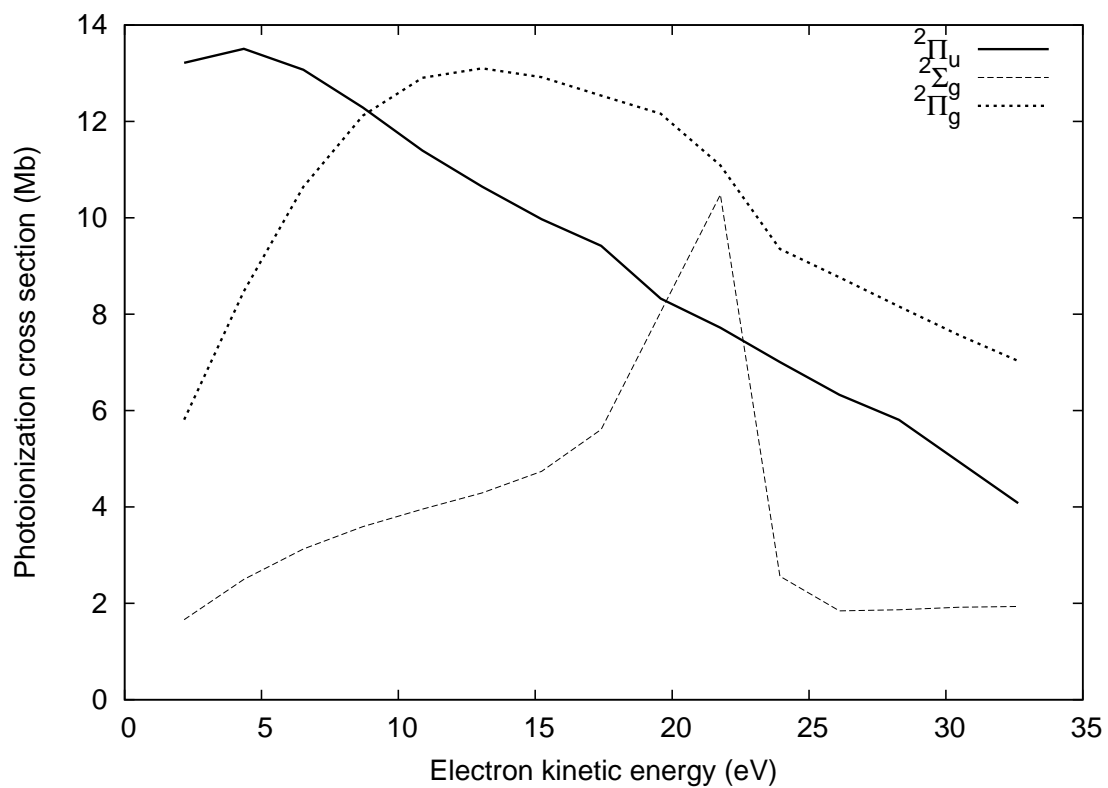Figure 4.10: The CO$_2$ photoionization cross sections are shown versus the kinetic energy of the photoelectron, for the three highest valence orbitals (π_u, π_g, σ_g), which generate the doublet final states in the figure. Agreement with the results of Lucchese et al. [119] is very good. In our calculation the σ_u resonance occurs roughly 1 eV higher than in Ref. [119]. From Ref. [191].

[207]. Probably the most evident feature is the low-energy t_{2g} resonance in the ungerade channels, which reproduces other literature results [207, 112]. A more detailed analysis of this spectrum can be found in Ref. [207].

4.5   HCO$^+$ Rmatrix-UK calculations

As a first example of results for the electronic degrees of freedom that we can extract from the R-matrix UK package to use subsequently in DR dynamics calculations, we have performed a scattering calculation with HCO$^+$ as a target. The results that we show in Fig. 4.13 represent the quantum defect parameters at positive energy, obtained near threshold (0.01 eV), as a function of the CH stretching and bending coordinates respectively. The calculations were performed using a basis set from Ref. [185] and 4 target states: two singlets and two triplets, the lowest in energy.

Around a bending angle of 30 degrees a state crosses the threshold and interferes with the π states, this is a Rydberg state relative to an excited electronic threshold. Notice also the Renner-Teller splitting of the two π states, which at this energy is quite small, as opposed to the large splittings present in the $n = 2$ Rydberg states shown in Fig. 3.2. The π states are not exactly degenerate at linear geometry because our orbital basis for the CI does not include all the orbitals obtained in a HF calculation of the target. If the CI included all the orbitals, the degeneracy would be exact, as we have tested, but the configuration space would become very large, and many of those high energy orbitals are not needed to gain an accurate description of the scattering process at the low energies we are interested in here. Our quantum defect results compare favorably with those taken from bound state calculations of Ref. [49] using a Green function approach and the ones we calculated with MRCI methods, shown in Sec. 6.2.1
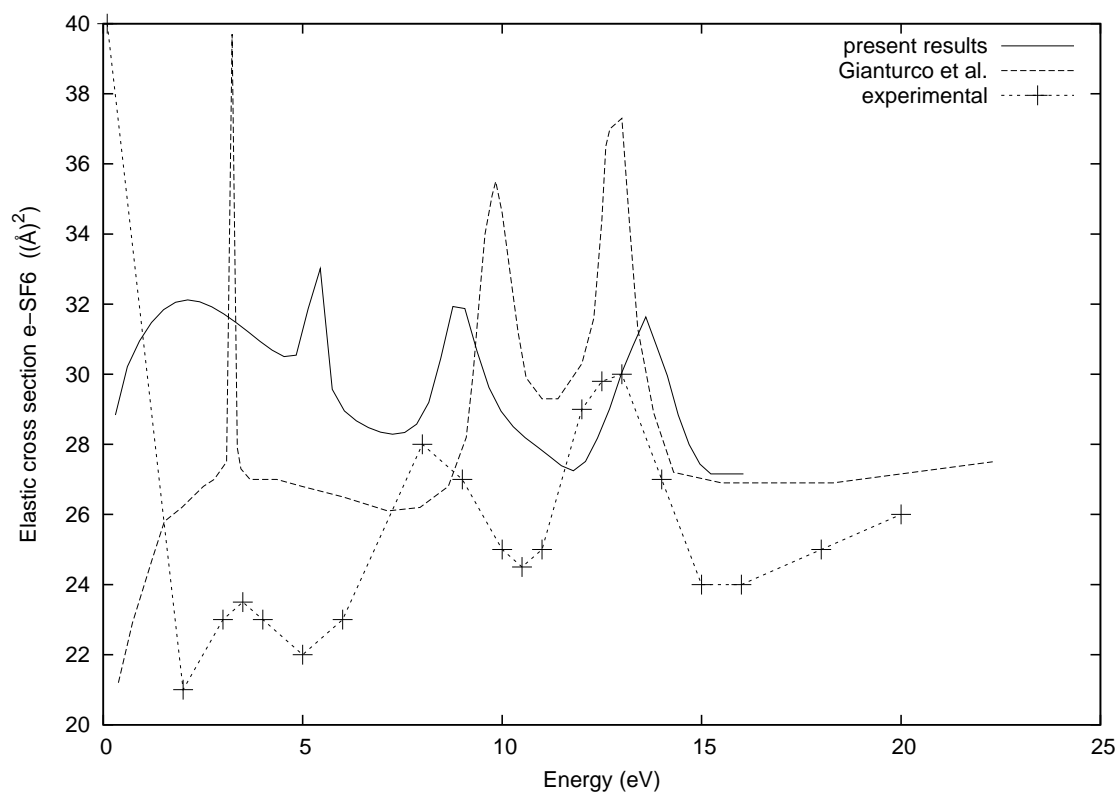
Figure 4.11: The e-SF$_6$ elastic scattering cross section shown as a function of energy, is compared to the calculations of Ref. [59] and experiment by Kennerly *et al* [91].
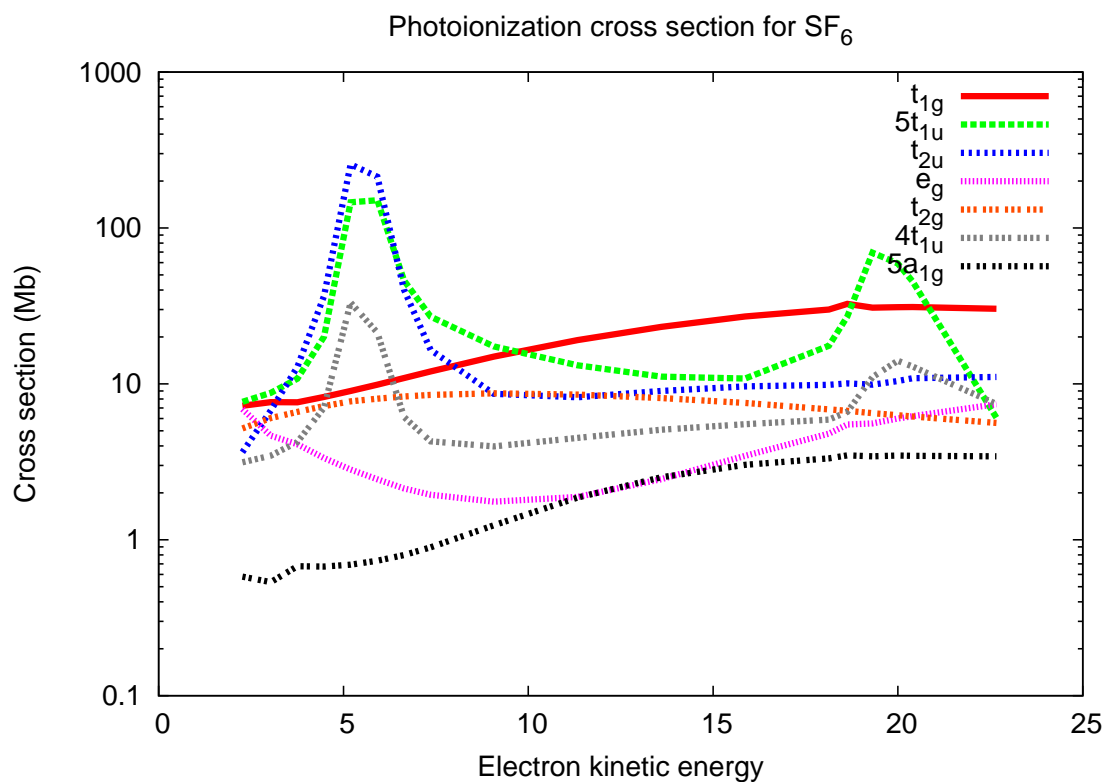
Figure 4.12: SF_6 photoionization cross sections versus photoelectron energy for the seven highest groups of valence orbitals indicated in the figure, which generate doublet final states. Comparison with the results of Ågren et al. [207] is good. In our calculation the high energy resonances in the t_{1u} and t_{2u} channels are much sharper than in Ref. [207], presumably due to the differences in the model potentials used.

and Ref. [104].

4.5.1 Perturbation results

As a test of the perturbative approach developed in Sec. 2.5.4 we perform calculations on scattering of an electron from HCO^+, at negative energies, to map out the quantum defect parameters. When the appropriate quantization condition is applied

$$det[K + \tan(\pi\beta)] = 0, \tag{4.5}$$

with β as in Eq. 3.10, the geometry-dependent quantum defects will determine the positions of the Rydberg states. HCO^+ has an electric dipole moment and also a strong quadrupole moment, therefore it is necessary to consider these contributions outside the R-matrix radius to obtain correct observables.

The R-matrix calculations we use to test this approach have been performed with $R_0=10a_0$ and only 1 target state, for the rest they are similar to what described in the previous section, the geometry of the molecule is taken to be the ground state equilibrium linear configuration. The highest partial wave included is a g-wave. In Fig. 4.14 a comparison is shown between different methods of dealing with the multipoles: by perturbation theory as described in Sec. 2.5.4 (blue dots) with integrals going up to $R_f=100a_0$, by R-matrix propagation [15, 127] (green dots) up to $R_f=65a_0$ and neglecting them altogether (red dots). The agreement between the simple perturbative approach and the propagation is very good down to -0.015 a.u. Below this energy, the effect of strongly closed channels is visible in the abrupt oscillations of the quantum defects, which are smooth throughout the energy range shown in the figure when the multipoles are omitted. The energy at which the effect of the closed channels starts to be strong is
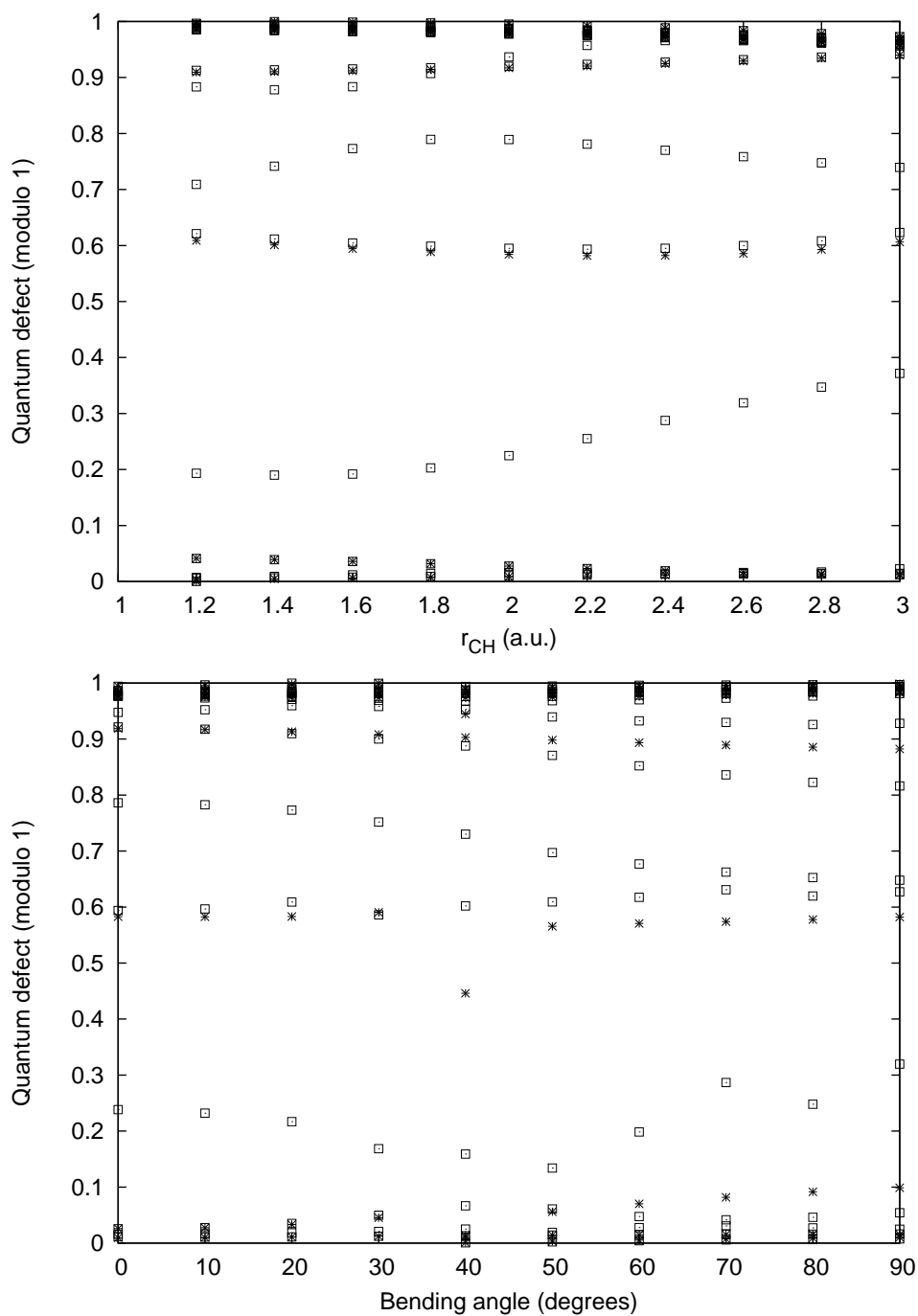
Figure 4.13: Top: R-matrix calculation of eigenquantum defects at threshold (0.01 eV) for HCO$^+$ plus an electron, as a function of the CH stretching coordinate, with the CO coordinate and bending angle kept at their ionic ground state equilibrium values. The squares represent the A' states, while the asterisks represent the A'' states. Bottom: R-matrix calculation of eigenquantum defects at threshold (0.01 eV) for HCO$^+$ plus an electron, as a function of the bending angle, zero degrees represents the linear ionic equilibrium geometry.

a function of R_f, in general the higher this value the higher the energy at which these effects are visible. We would like to point out that using the perturbative approach developed in Ref. [12] the results obtained are very similar, except that strong oscillatory behaviors result at very negative energies.

In general it is not possible, in a system as complex as the one we have considered, to obtain quantum defect parameters that are smooth in an energy range that extends from threshold down to very negative energies with a single method. Both perturbation and propagation will at some point be affected by the strongly closed channels. Even if the closed channels are treated as such by channel elimination, Eq. 3.10, they still affect the remaining quantum defects as sharp avoided crossings at the closed channel energy. It is probably a better solution, especially in the case of polar molecules, to separate the very negative energy part of the spectrum and treat it in a different fashion.
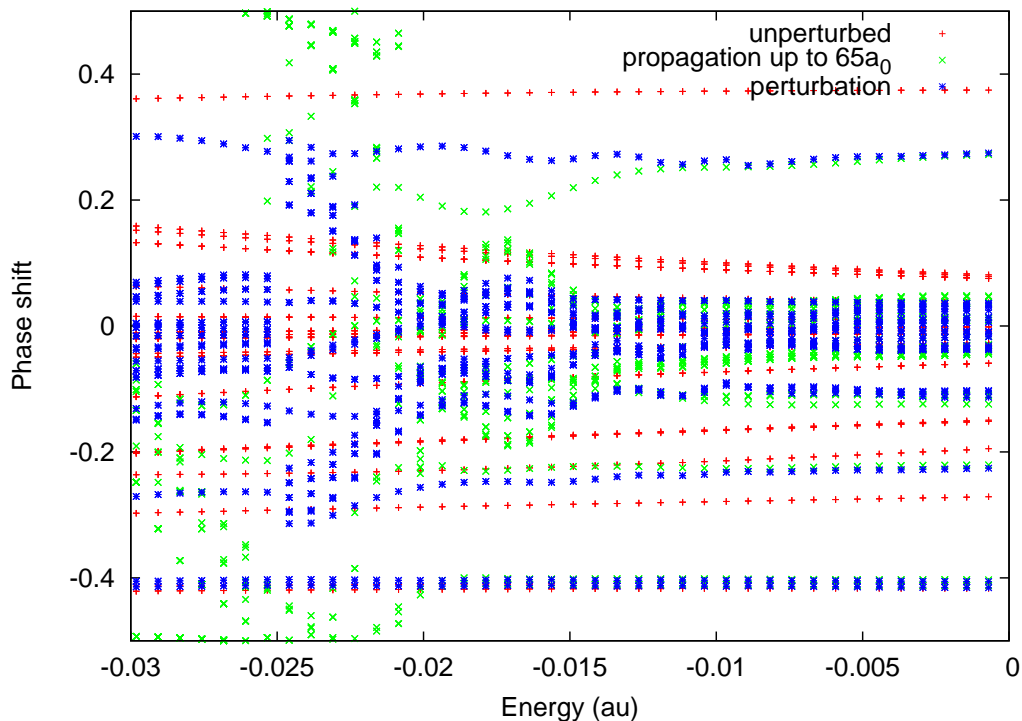
Figure 4.14: Comparison between unperturbed results (red dots) at R_0=10 a_0, perturbation theory (blue dots) with integration up to R_f=100a_0, and propagation from R_0 up to 65 a_0 (green) for quantum defects of HCO^+ plus an electron at negative energy. The perturbed values are very close to the correct ones obtained with R-matrix propagation, at low energies the effect of strongly closed channels is important. The R-matrix calculation includes up to $l = 4$, which will generate closed channels below $E = -1/(2n^2) = -0.0156$ a.u. for $n = 5$.

Chapter 5

Results: electron scattering, DNA bases

5.1   Introduction

In recent years, increasing importance has been associated with electron-induced chemical processes in biological environments, especially in relation to radiation damage to nucleic acids (DNA and RNA). These processes are initiated by the interaction of ionizing radiation with living tissue, generating possibly mutagenic and carcinogenic byproducts. A wide variety of subsequent ionization, excitation and energy transfer processes can generate possibly mutagenic and carcinogenic byproducts, which can affect many molecular species in the complex cell environment.

The important work of Sanche and coworkers [24, 111, 159] has shown that damage to nucleic acids from ionizing radiation [140] (single and double strand breaks in particular) can be generated through a mechanism involving low energy electron attachment to the nucleic acid and subsequent bond breaking due to energy transfer to a vibrational mode of the temporary anion formed in the electron capture step. The ionizing radiation produces high energy primary electrons (with energies of the order of a keV), which in turn, through electron-impact ionization, produce many low energy secondary electrons. In the electron-impact ionization process, the scattered electron

loses part of its kinetic energy, while another electron is ejected, with energy much lower than the first one. It has been shown that the secondary electrons have an energy distribution concentrated between 0 and 20 eV [34]. A schematic representation of the radiation damage process is shown in Fig. 5.1.

If the electron energy is higher than the ionization threshold for DNA (between 7.85 and 9.4 eV, as measured for the DNA bases [114]), then the nucleic acid can be ionized and damage produced through the subsequent rearrangement and dissociation of the cation [54]. If the electron energy is lower, damage can still be generated through a negative ion-mediated mechanism, that starts with the capture of the electron in a molecular resonance, followed by a transfer of energy and electron density into a weak bond that subsequently ruptures. Beyond this generally accepted framework, there are many controversial issues, such as the locus of the initial capture site, [24] the evolution of the anion produced and which bond actually ruptures.[17, 210]

In the past few years many studies have been devoted to understanding the mechanisms triggered by the low-energy electrons, including especially their capability to cause strand breaks [5, 17, 78, 121, 164]. A first general feature on which there is wide agreement is that the electron capture is mainly due to the DNA and RNA bases. These molecules have extended aromatic systems, whereby there are numerous low-lying unoccupied π^* orbitals into which an electron can be captured. The capture often occurs into a shape resonance, a temporary anion, in the range of energies between 0 and 15 eV, where experiments have found signatures of electron-induced damage to nucleic acids.

The simplest of these bases are thymine, cytosine, uracil (pyrimidines, monocyclic) and adenine and guanine (purines, bicyclic and generally larger than pyrimidines). Their structures are shown in Fig. 5.2. In this chapter we will present theoret-
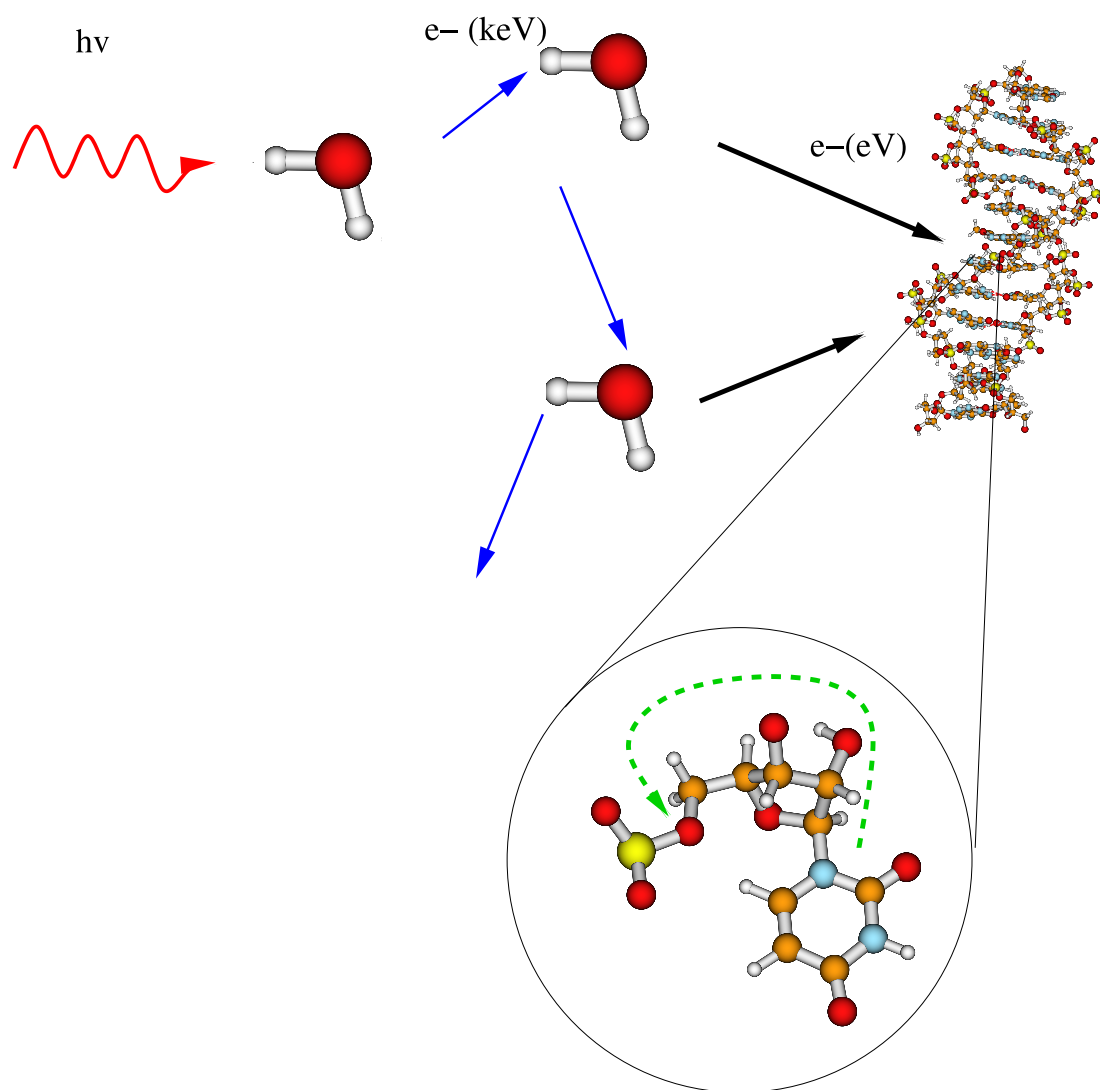
Figure 5.1: Schematics of the DNA damage from low energy electrons: highly energetic ionizing radiation (in red) impacts a molecule in the cell (water in this case) extracting keV primary electrons (in blue), which in turn extract low energy secondary electrons (in black) through electron-impact ionization. These impact DNA and are captured by the bases (shown in the inset is a uridine nucleotide, it will be replaced by thymidine in DNA), then an energy transfer through the sugar (in green) breaks a bond and generates a strand break. The B-DNA structure is taken from Ref. [83].

ical predictions of cross sections and of even greater relevance, collisional time delays, for elastic electron scattering from these large molecules. Determination of the location, width, and electronic structure of resonances for a single target molecule is an important step towards understanding and possibly modeling the complex dynamics of DNA, which consists of multiple components. Specifically, besides the bases, there are also the sugar backbone, the phosphates, and the solvation water [22], that probably plays a major role in stabilizing the temporary anions [70, 176]. No previous theoretical or experimental study of low-energy electron scattering from all of the DNA and RNA bases is available for comparison (although a study at intermediate energy has been carried out recently [140]), but our method has proven its reliability in the study of small molecules [192] and more extended systems like C_{60}, SF_6 and XeF_6, as we have shown in Sec. 4.3.2 and 4.4.2.

Much experimental work also has been carried out on dissociative electron attachment from the DNA bases [2, 66, 121], to understand what fragments are generated. We will discuss the possible connections with measured dissociation branching ratios that we can infer from the examination of the spatial shape and nodal surfaces of the resonant wavefunctions.

5.1.1   Elastic cross sections

To our knowledge there are no available experimental data or calculations of low energy electron scattering from the complete set of DNA bases. A study of electron attachment has been presented in Ref. [5] and the resonance positions are clearly marked. Compared to these results, our calculations show resonances shifted typically by about 2 eV higher in energy, but the energy spacing of the resonances is comparable
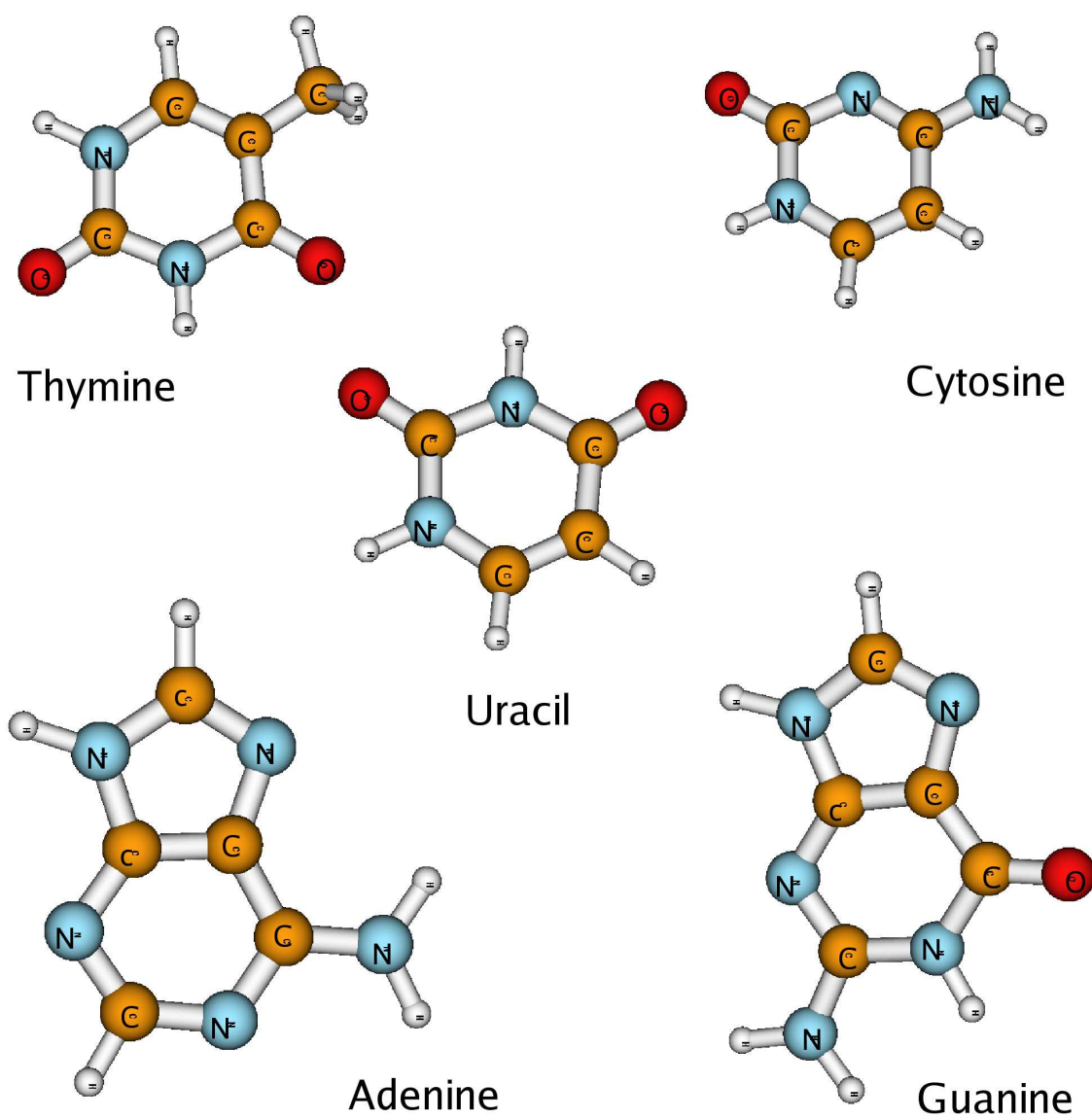
Figure 5.2: Ground state equilibrium structures of the molecules considered in this section The red atoms are oxygens, the orange circles represent carbons, the blue atoms are nitrogens while the small circles are hydrogens. From Ref. [194].
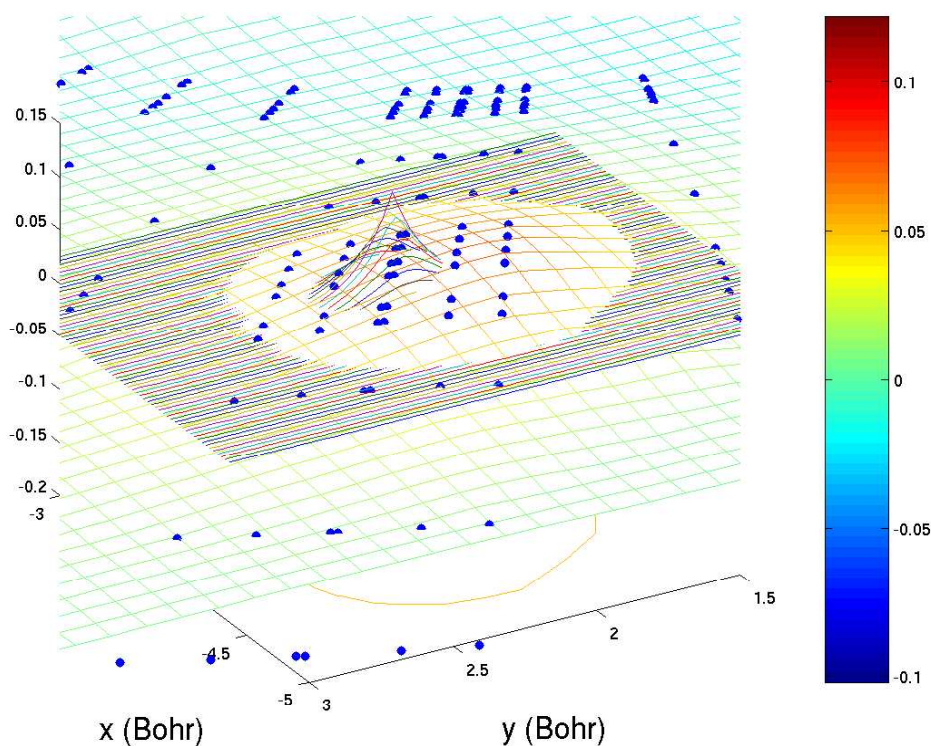
Figure 5.3: Blowup of the resonant wavefunction surface for uracil at 2.4 eV (Fig. 5) near an oxygen atom. This surface is a cut through the plane containing the nuclei, shown in the region of the oxygen atom attached to C_2. The dots are the actual grid points of our calculation, while the coarsely spaced grid is a linear interpolation of the resonant wavefunction (eigenstate of Eq. 5.1) and the finely spaced grid that shows a cusp is the K-shell orbital of oxygen, here represented to show how our grid is designed around the nuclei. The colorbar on the right side refers only to the resonant wavefunction, while the K-shell orbital is colored just to make it more visible. The K-shell orbital is shifted upward by 0.04 to make it more clearly visible, therefore its base is not a nodal surface. From Ref. [194].

to what is observed in the experiment. Moreover the relative values of the widths of successive resonances resemble the measured widths. There is also a theoretical study at intermediate energies [140], and calculations of electron scattering from uracil [60, 70]; in the following we compare these results to ours.

We have already mentioned that the heterocyclic DNA bases have many low-lying unoccupied orbitals, so it is not surprising that their elastic cross sections for electron scattering exhibit many shape resonances. These can be viewed as a capture of the scattering electron into one of these antibonding orbitals to form a short lived negative ion state [40, 116].

Since all these molecules have, in their equilibrium configuration, only one symmetry element - reflection through the molecular plane - we will characterize the resonances as being of σ type (no node in the plane) or π type (when they have instead a node in the plane) rather than using the A' and A'' labels as is customary for the C_s group.

5.1.2   Positions and widths of resonances

A general comparison of partial elastic cross sections for all five of these molecules is shown in Fig. 5.4, while in the following we give a more detailed description and compare with information available in the literature. Also, a plot of total time-delays (see also Sec. 5.1.3 for details) is provided in Fig. 5.5 to show the resonances in more detail.

Since we are dealing with polar molecules, use of the fixed-nuclei approximation as it stands makes the partial wave expansion of the forward scattering amplitude divergent. Due to the long-range nature of the dipole interaction, in fact, all partial waves would contribute to the scattering process, causing an infinite differential cross section

in the forward direction and therefore infinite integral cross sections. There is a method, extensively discussed in the literature [32, 61], to deal with this problem by means of a Born closure formula, which yields a finite integral cross section once molecular rotations are included. We will not pursue this further, since existing experiments are not likely to deal with such detailed rotational structures. Therefore our cross sections and time-delays include only up to $l_{max} = 10$ and omit all higher partial waves. The correction would be proportional to the dipole moment and inversely proportional to the smallest rotational spacing. For the DNA bases the dipole moment is large, while the rotational spacing is small. Therefore the correction can be quite large especially at very low energy. The correction would thus tend to mask the resonant structures, which are the most interesting observables and which have been measured in experiments. All of the calculated cross sections grow rapidly when the incident electron energy decreases below 1 eV, which is a signature of the role played by the dipole field in pulling in the electron and which is very common in electron scattering from polar molecules [5, 69].

A comparison of our resonance patterns with the electron transmission spectroscopy (ETS) data of Burrow and coworkers [5, 164] can be found in Figs. 5.6-5.8, for a comparison of energies, widths and spacing. All of the resonances obtained in our calculations are listed in Table 5.1.

5.1.2.1   Uracil

In the cross section of uracil we find 3 resonances, at 1.3 eV (of width 0.2 eV), at 3.5 (0.6 eV wide) and a very broad resonance at 6.3 eV. The resonance at 1.3 eV is dominated by the $l = 3$ partial wave (50%) and has contributions from $l = 1$ (35%) and $l = 2$ (11%). at 3.5 eV the main partial wave is d (66%), at 6.3 eV f-wave is the

Molecule	Energy (eV)	Width (eV)	Partial wave
Uracil	1.3	0.2	3 (50%)
	3.5	0.6	2 (66%)
	6.3	0.9	3 (64%)
Thymine	1.5	0.3	3 (53%)
	3.8	0.6	2 (62%)
	6.8	1.0	3 (61%)
Cytosine	1.6	0.3	3 (51%)
	4.0	0.7	2 (68%)
	8.1	0.8	3 (63%)
Adenine	2.4	0.2	2 (65%)
	3.2	0.2	2 (62%)
	4.4	0.3	3 (51%)
	9.0	0.5	5 (53%)
Guanine	2.4	0.2	2 (46%)
	3.8	0.25	2 (44%)
	4.8	0.35	4 (38%)
	8.9	0.6	5 (33%)
	12.0	1.0	4,5 (both 23%)

Table 5.1: Energies, widths and largest partial waves (and percentages) of the resonances discussed in the text for the DNA and RNA bases. From Ref. [194].
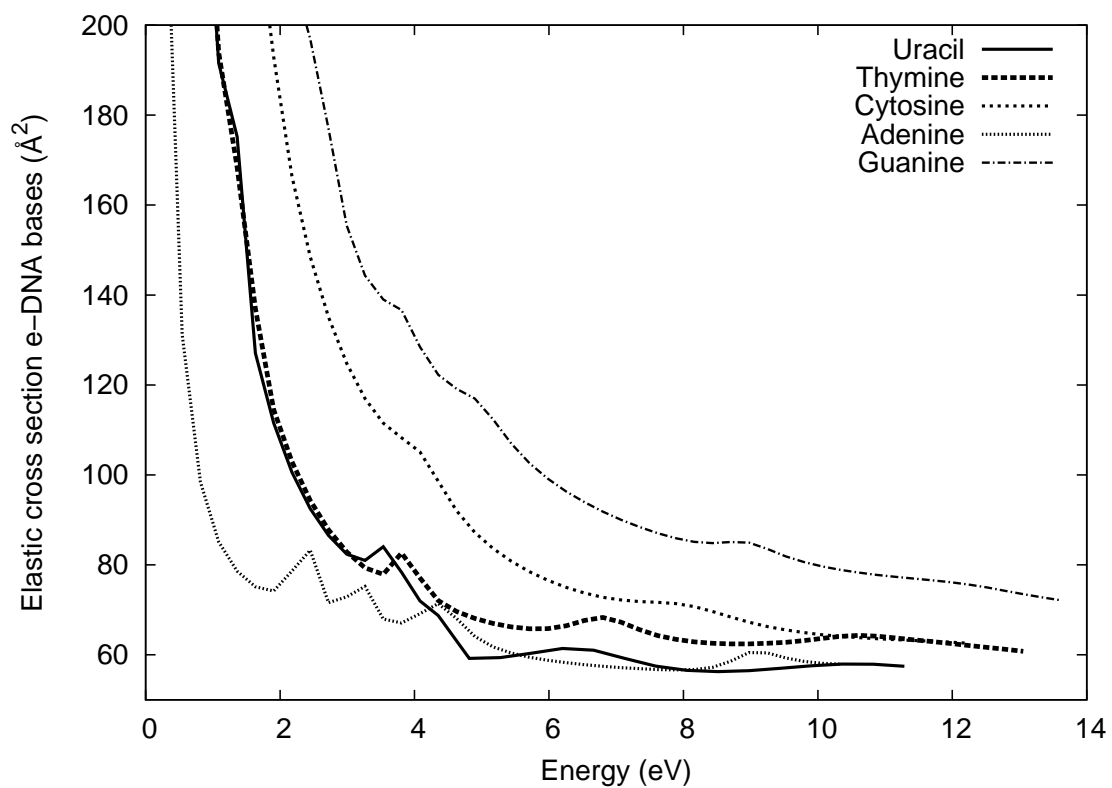
Figure 5.4: Partial elastic cross section for the 5 DNA and RNA bases described in the text. Calculations involve partial waves up to $l = 10$ and the dipole physics outside the R-matrix box is included exactly, for those partial waves. From Ref. [194].
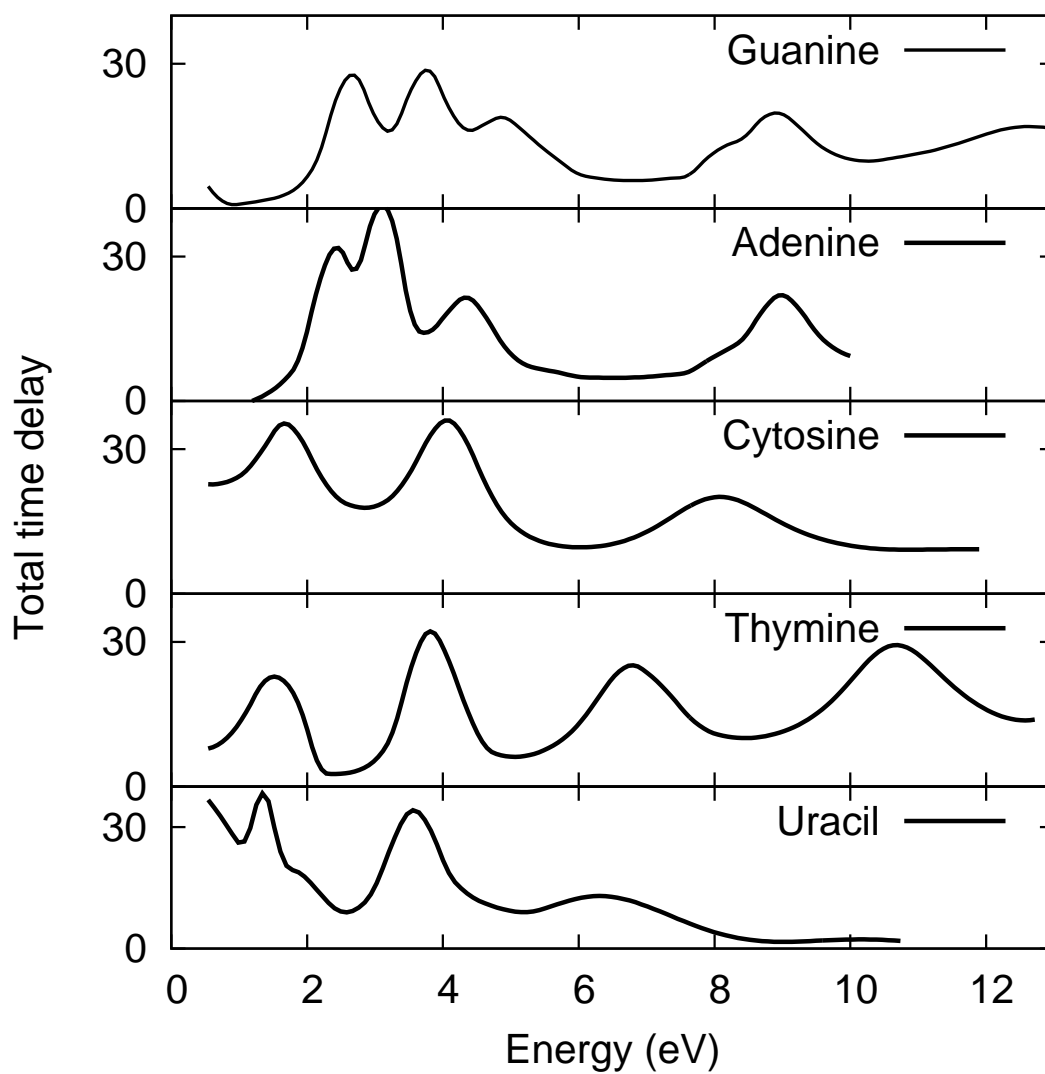
Figure 5.5: Total time-delay for the DNA bases described in the text. From Ref. [194].

dominant contribution (64%).

In the work of Gianturco *et al.* (see Ref. [60]) three π^* resonances are found at energies of 2.2, 3.5 and 6.5 eV. The second and third π^* resonances from that work fall at lower energies than ours, a somewhat surprising discrepancy since the theoretical models are very similar.

The contribution of the dipole field at distances larger than 12 Bohr is neglected in Ref. [60], but we have noticed that this influences only the overall magnitude of the cross sections (roughly an increase of 20% at very low energy, that is reduced to about 5% around 10eV), the dipole physics only weakly affects the resonance positions and widths.

Resonances are measured in Ref. [5] to occur at 0.3, 1.5 and 3.8 eV. They are all assigned as π resonances [164], so our results should be shifted by about 1.1 eV down, whereas the spacing between the resonances is larger than experiment. The relative resonance widths are similar to Ref. [164], in that the first resonance is very narrow, the second broader and the third very broad, a comparison is shown in Fig. 5.6, where an integration of the experimental data has been performed to show more clearly the resonance positions and widths.

5.1.2.2   Cytosine

For cytosine we find 3 main resonances, a very sharp one at 1.7 eV (width 0.3 eV), then at 4.0 eV (width 0.7 eV) and a third at 8.1 eV (width 0.8 eV). The dominant angular momentum character of the resonances is the same as for the three corresponding resonances of uracil. Comparing the resonance positions with the experimental data of Ref. [5] we see the same general trend already observed with uracil, namely an overall

shift higher than experiment of all resonances by about 1.4 eV. Interestingly, the first two resonances are measured to occur at an energy lower than in uracil, a trend that is not verified in our calculations. However the third resonance is at a much larger energy than in uracil and thymine, which also happens in the experiments.

5.1.2.3   Thymine

The scattering cross section for thymine is closely similar to uracil, which is not surprising in view of their close structural similarities, this applies to both the magnitude and the position of the resonances, which are slightly shifted to higher energies. Specifically, we find resonances at 1.5 eV (width 0.3 eV) at 3.8 eV (width 0.6 eV) and at 6.8 eV (width 1 eV).

5.1.2.4   Adenine

The electron scattering spectrum for adenine presents many resonances, as expected due to the complexity of the target structure. Also very interesting is the fact that the cross section drops sharply at energies below 2 eV, a behavior opposite to that found for the other molecules, if we do not consider the dipole physics outside the R-matrix box, whereas a zero-energy peak appears in the full calculation, a possible sign of a dipole bound state right below threshold.

The first resonance occurs at 2.4 eV (width 0.2 eV), the second at 3.2 eV (sharp, width 0.2 eV), then another centered at 4.4 eV (0.3 eV wide), while at 9 eV we have a broader resonance of width 0.5 eV. The dominant partial wave of the first two resonances is $l = 2$ (65% and 62% respectively). The third resonance is $l = 3$ at 51% and $l = 4$ at 33% The resonance at 9 eV is dominantly $l = 5$ (53%) with an $l = 3$ contribution

(22%).

Compared to experiment we have a shift of all resonances roughly 1.5 eV higher, as in guanine, in this case the spacings are correct (about 1 eV between the first three resonances, while the fourth falls too high in energy and it is not measured in experiment). Also the experimental widths of the first three resonances are very similar, as in our data. A comparison with the data of Ref. [5] is shown in Fig. 5.7.

5.1.2.5   Guanine

For guanine we find 4 resonances: at 2.4 eV (width 0.2 eV), at 3.8 eV (width 0.25eV), a third at 4.8 eV (width 0.35 eV), then at 8.9 eV (width 0.6 eV) and a broad resonance around 12 eV. Each of the first three resonances has strong contributions from d, f, and g-waves. At 2.4 eV the contributions are 46% for $l = 2$ and 37% for $l = 3$, for the second resonance $l = 2$ is 44% while $l = 4$ is 32%, the third is 38% of $l = 4$ character and 35% of $l = 3$. The resonance at 8.9 eV is 33% h-wave, 28% f-wave and 20% g-wave. At 12 eV the composition is: $l = 4$ and $l = 5$ equally at 23%, while $l = 6$ contributes a further 13%.

Comparison to experimental data (see Fig. 5.8) shows again a shift of 1.5 eV overall, while the resonance spacing is well reproduced, and the second and third resonances fall at higher energies with respect to adenine, as in our calculations. Also the widths seem close to experiment.

5.1.3   Resonance molecular structures

From the shapes and nodal structures of the resonant states it is possible to attempt a discussion of the dissociation patterns observed experimentally, if we consider
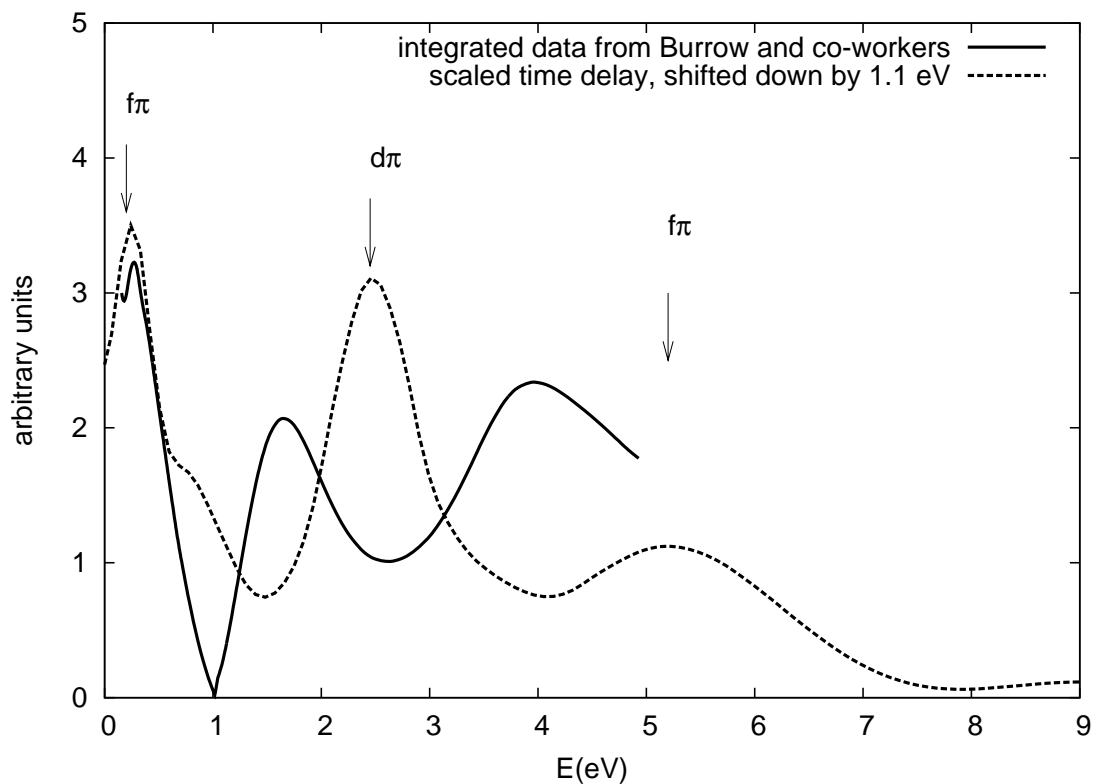
Figure 5.6: Comparison of our calculated time-delay with the experimental scattering cross section data of Burrow and co-workers [164] for uracil. The arrows indicate resonance positions from the present work, while labels show the dominant partial wave of resonance. The time-delay curve is shifted downward by 1.1 eV to have the position of the first resonance coincide with experimental data. From Ref. [194].
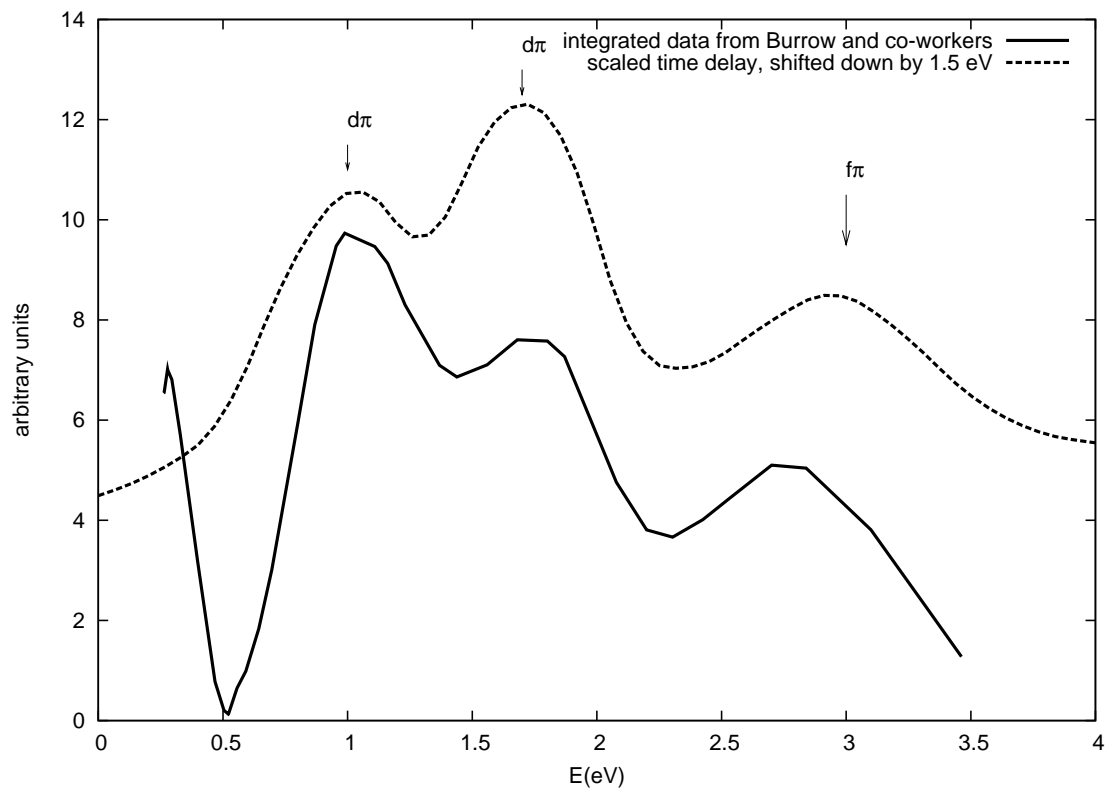
Figure 5.7: Comparison with experimental data of Burrow and co-workers [5] for adenine. The arrows indicate resonance positions from the present work, while labels show the dominant partial wave of resonance. The time-delay curve is shifted downward by 1.5 eV to have the position of the first resonance coincide with experimental data. From Ref. [194].
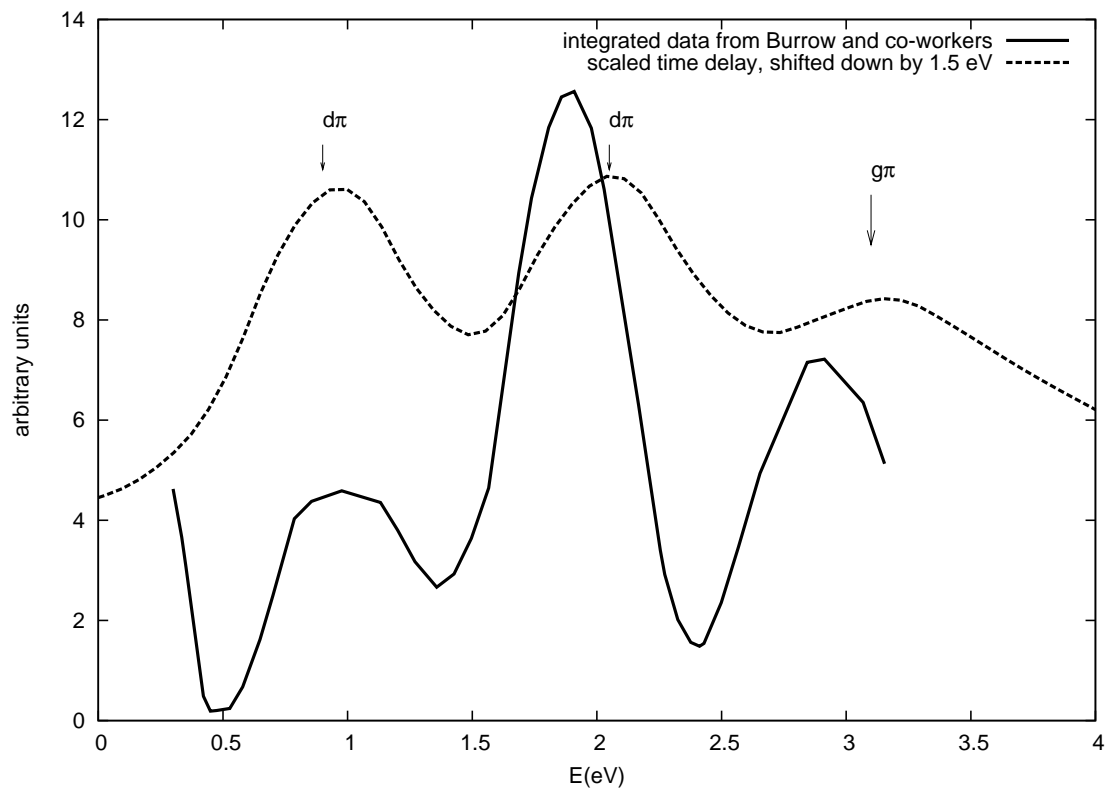
Figure 5.8: Comparison with experimental data of Burrow and co-workers [5] for guanine. The arrows indicate resonance positions from the present work, while labels show the dominant partial wave of resonance. The time-delay curve is shifted downward by 1.5 eV to have the position of the first resonance coincide with experimental data. From Ref. [194].

the resonant states as being precursors for dissociative states. Caution must be used, though, in drawing conclusions from this analysis, because this involves a certain degree of speculation. In fact, to establish once and for all the dissociation patterns of these complicated systems, scattering calculations at many different geometries would have to be carried out, and the nuclear dynamics should be included, At present this is computationally too expensive to contemplate. The first two resonances observed for uracil are shown in Fig. 5.9. The quantity plotted is a projection on the molecular plane of the eigenvector corresponding to the maximum eigenvalue of the time-delay matrix [74]

$$Q = iS\frac{dS\dagger}{dE}, \tag{5.1}$$

where S is the scattering matrix. At the energy where the time delay of the resonance is a maximum, this eigenvector constitutes the dominant contribution to the resonant structure, since it corresponds to the partial wave that experiences the maximum time delay in the scattering process. For sufficiently narrow resonances one eigenvalue is always dominant, making the resonance analysis much easier. The eigenvectors of the time-delay matrix are complex, so we adopt a phase factor such that the highest peak of the wavefunction is a purely real number. We then find that the resonance wavefunction is real everywhere, to a good approximation (the imaginary part is about 10^{-6} smaller than the value of the real part), and we plot only the real part. We analyze in detail only the cases of uracil and adenine, the other pyrimidines being very similar to the former and guanine to the latter.

The nodal patterns for uracil are very similar to the ones showed in Ref. [60], which is not surprising since the approximations made in that work are similar to ours,

as already discussed, therefore we show only the first two resonances. Incidentally, we notice the close resemblance of these resonant wavefunctions to the first virtual orbitals of uracil from a HF calculation performed with a small basis set (6-31G*), see for example Fig. 5.10. In Ref. [60] also a very low σ^* resonance is found at 0.012 eV. Our cross section grows substantially at low energy. If we plot the eigenstate corresponding to the largest eigenvalue of the time-delay matrix (as described in Sec. 5.1.3), as in Fig. 5.9, corresponding to this low energy range, it looks similar to Fig. 5 in Ref. [60], with the main differences being that in our wavefunction the N_3-H bond has a node, there is a large excess charge on N_3 and on the oxygen attached to C_4, while another nodal surface cuts diagonally from C_2 to C_5. This state anyway does not appear to be so relevant in the experimental data [164], where mainly the π^* resonances are detected.

We can also see that there is accumulation of electronic density (the peaks of the wavefunction) on the ring structure, and that many of the ring bonds have nodal surfaces cutting through them, so capture in these resonant states can be reasonably thought as leading to a fragmentation of the molecule in which the aromatic ring is broken. Experimental dissociation patterns are illustrated for Br-uracil in Ref. [2], where evidence for breaking of the ring structure lies in the peaks at 1.6 and 3.5 eV produced by $(OCN)^-$ and other fragments. These fragments can be generated by capture into shape resonances, appearing in our calculations at 1.3, 3.5 and 6.3 eV respectively. In particular there is a nodal surface in the 3.5 eV resonance that encloses the C_4-N_3 bond, which could generate a CN^- fragment.

Since our calculations do not take into account core-excited states or vibrations, our results do not include any Feshbach resonant structures. These appear to cause at least some of the patterns observed in experiment, as in the case of uracil, [164] and they

will presumably constitute the dominant trapping pathways for energies higher than 7 eV, where the number of electronic Feshbach resonances starts to become very large, as shown in Fig. 5.13.

In the case of uracil, we looked carefully for a σ^* resonance that might be similar to the state shown in Fig. 3 of Ref. [164] around 3 eV at equilibrium geometry, a dissociative state most likely responsible for N_1-H bond cleavage. The Ref. [164] calculation was performed by scaling Hartree-Fock continuum orbital energies, so no information about the width was provided. Such a state, taking into account an expected shift of 1-2 eV upward in our calculations, should have appeared at around 5-6 eV, and it was not found. This is probably due to the fact that this resonance is extremely broad, since it is also not seen even in experiment [164]. Moreover in calculations carried out using complex absorbing potentials, in connection with Green's function methods [160, 51], for similar systems (like benzene [50]), analogous σ resonances were extremely hard to detect. They became narrower (around 1eV width at equilibrium) only when the relevant hydrogen was substituted with a heavy atom like chlorine; this was also demonstrated experimentally in the case of Cl-uracil in Ref. [164].

For adenine there is less experimental information available to compare. In Ref. [66] it is stated that the dominant breakup channel for low energy (0-4eV) electron attachment leads to hydrogen atom loss, and very prominent resonant structures are present in the range 1 to 3 eV. Looking at the resonance wavefunction maps in Fig. 5.11-5.12 we can see that there is no significant buildup of electronic density on any of the hydrogens, consistently with the fact that the negative charge stays on the molecular frame, and therefore there is no H^- formation.

The first few unoccupied molecular orbitals that can be obtained from a Hartree-
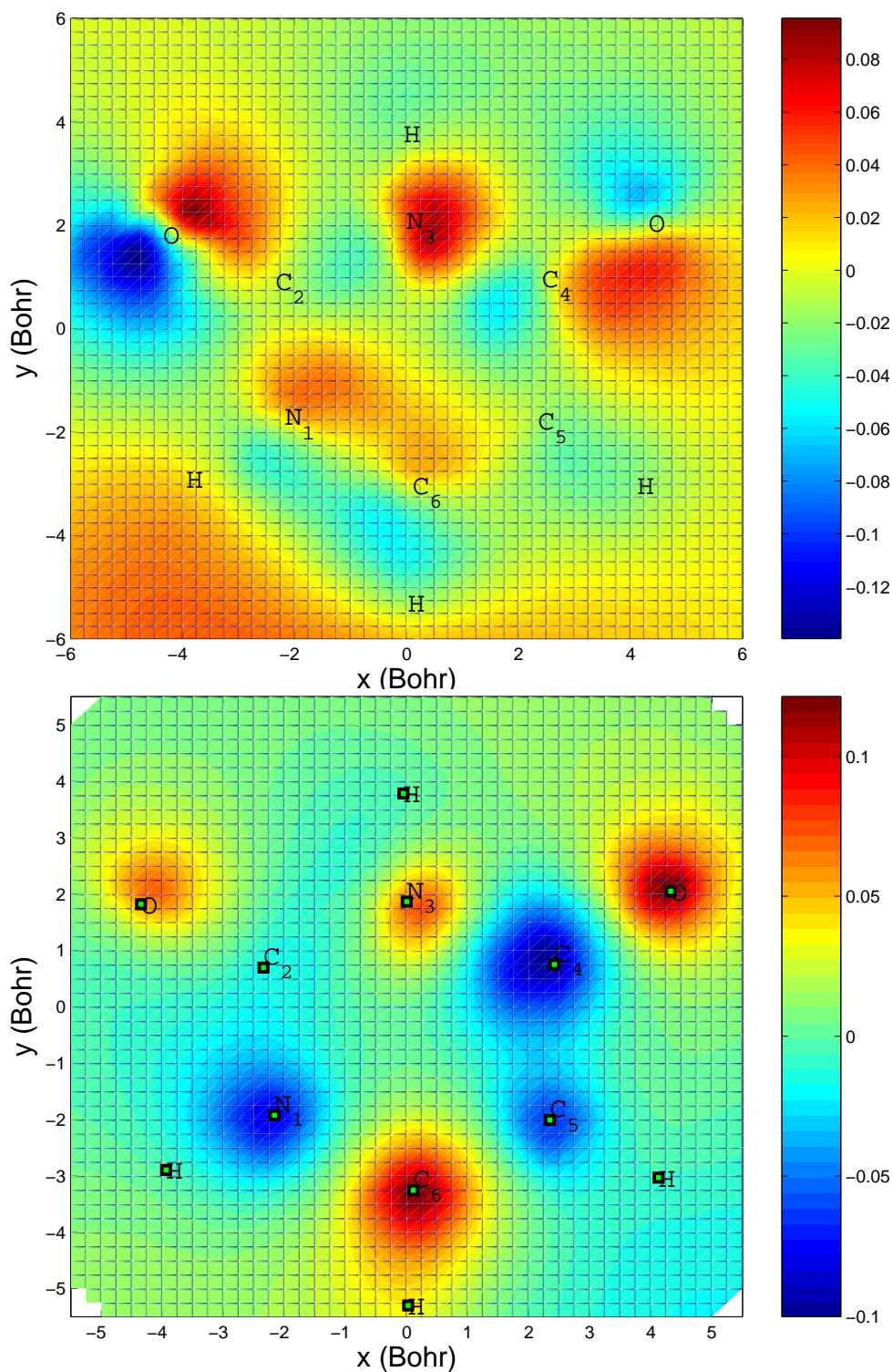
Figure 5.9: Top: Eigenvector associated with the dominant eigenvalue of the time-delay matrix in uracil at a low but nonresonant energy, as described in the text, for scattering at 0.2 eV. Bottom: first resonance wave function in uracil. Eigenvector associated with the dominant eigenvalue of the time-delay matrix, as described in the text, for the resonance at 1.3 eV. The green squares correspond to the nuclei positions. From Ref. [194].
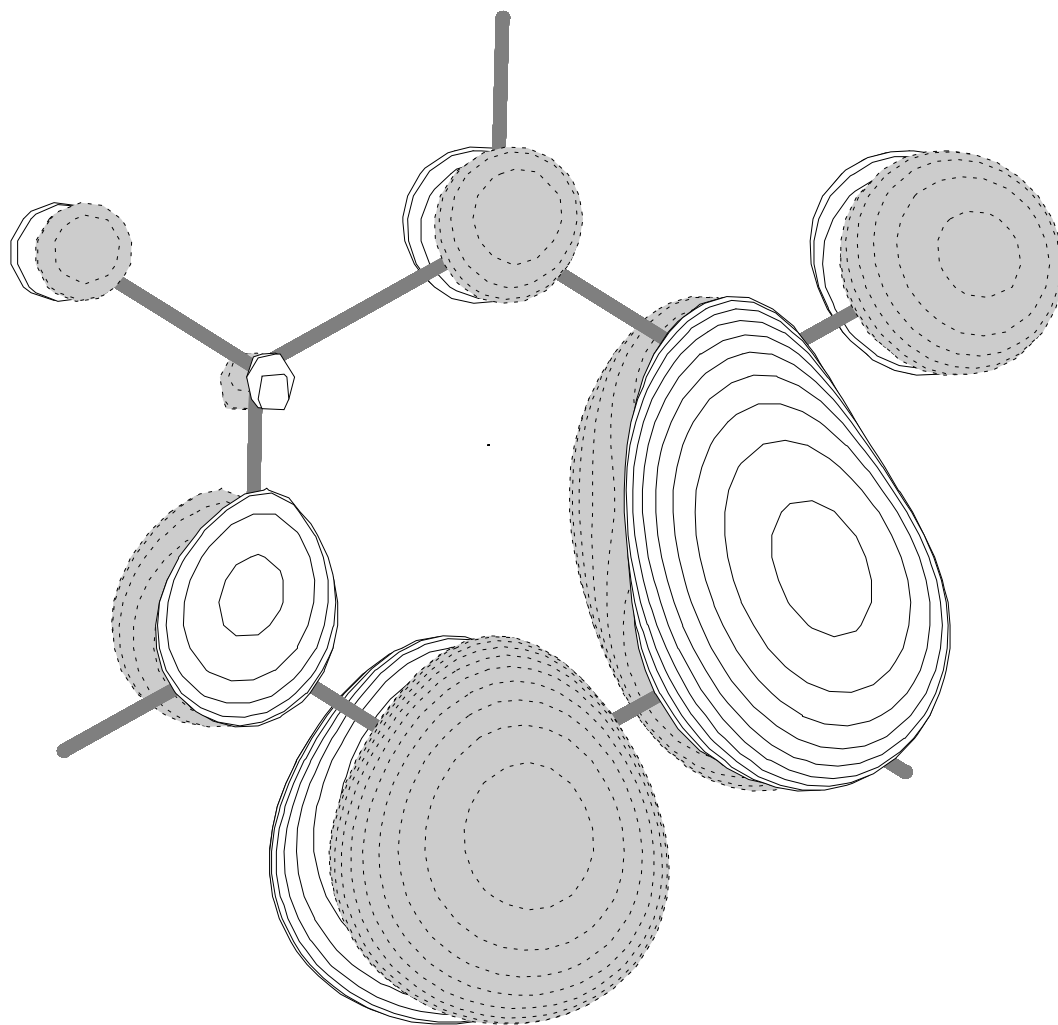
Figure 5.10: Uracil: structure of the virtual orbital associated to the resonance at 1.3 eV. The energy of this virtual orbital is 3.42 eV when using a 6-31G** basis set. The orientation of the molecule is the same as in the previous plots. The black and white lobes correspond to opposite signs. It is possible to notice the node in the molecular plane that makes this a π^* orbital. From Ref. [194].

Fock calculation for adenine, as in the case of uracil, are extremely similar in their nodal structures to our resonant wavefunctions, so these shape resonances can be viewed quite reasonably as the trapping of the scattered electron in a virtual orbital.

Most of the C-C and C-N bonds have nodal surfaces passing through them, This might suggest that other channels that involve the breakup of C-C and C-N bonds could also be available at these energies, although probably they are less important than the hydrogen loss products.

5.1.4   Uracil - Rmatrix UK

We have studied uracil in particular with the more accurate R-matrix UK code, described in Sec. 2.4.2. The aim of this study was to determine potential energy curves as a function of the N_1H bond stretching coordinate, since in a study by Burrow *et al.* [164] it has been suggested that this coordinate can lead to dissociation of the hydrogen in a simple one-dimensional picture, without the need to consider couplings with out-of-plane motion or other normal modes.

We first have performed a simple calculation for the equilibrium geometry, shown in Fig. 5.13 using the 4 lowest states of the target (two singlets and two triplets) in the close coupling expansion and a 6-31G** basis set. The CI used here is forcibly very limited, with only 8 electrons allowed to move, therefore we know that the dissociation limit will not be well described. The polarization that we allow for the target is also somewhat limited, therefore these results will be relatively similar to static exchange calculations. The results we obtain for the resonance positions are similar to our previous static exchange plus polarization calculations, see also the discussion in Sec. 5.3. In this case we can separate the different symmetry contributions in A' (symmetric with
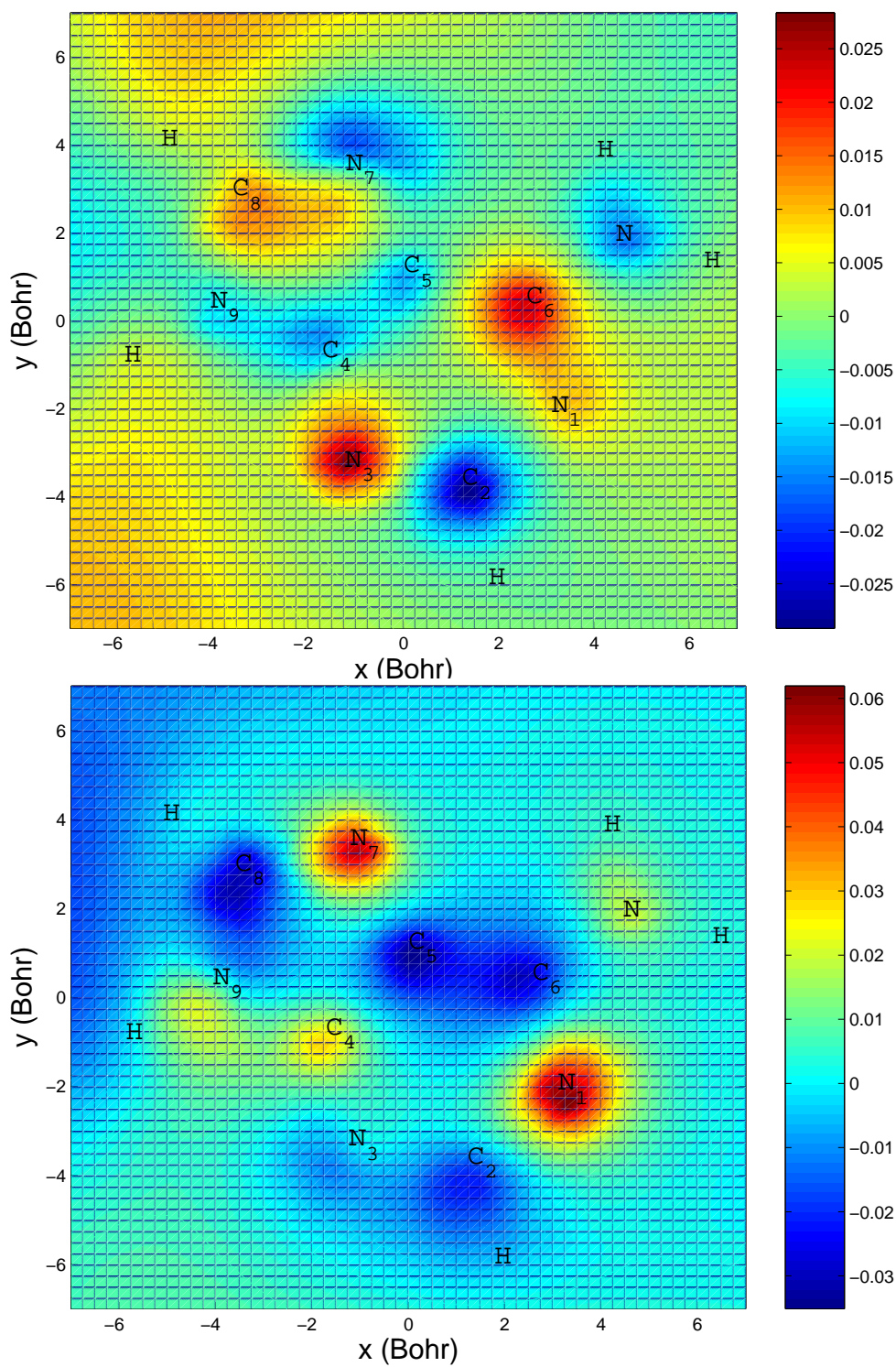
Figure 5.11: Top: 1st resonance wavefunction for adenine. Eigenvector associated with the dominant eigenvalue of the time-delay matrix, as described in the text, at 2.4 eV. Bottom: 2nd resonance wavefunction for adenine. Eigenvector associated with the dominant eigenvalue of the time-delay matrix, for the resonance at 3.2 eV. From Ref. [194].
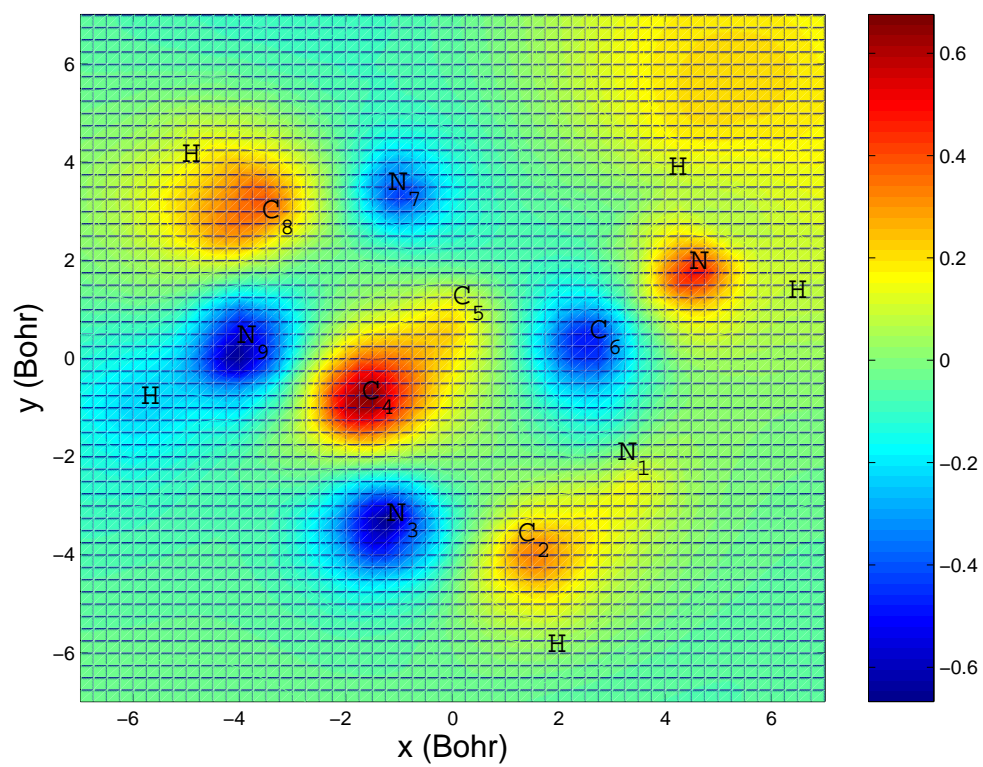
Figure 5.12: Adenine: 3nd resonance wavefunction. Eigenvector associated with the dominant eigenvalue of the time-delay matrix, as described in the text, for the resonance at 4.4 eV. From Ref. [192].

respect to the molecular plane) and A'' (antisymmetric), therefore it is possible to show easily how the resonant structures are all in the A'' (or π) channel. It is also possible to evince from the data that the first three π^* resonances are shape resonances, while the others are Feshbach type resonances. According to the results of a simple Hartree-Fock calculation, in Ref. [164] it was stated that a dissociative σ^* resonant curve should be present at low energy. Performing scattering calculations we found no indication of this resonance, which means that its width is extremely broad ($>$1eV), as stated previously. The results as a function of the N_1H stretch, shown in Fig. 5.14, are similar to the curves in Ref. [164], in that the π^* resonances are parallel to the neutral ground state. The position of the σ^* resonance, though, cannot be determined. A resonant state becomes bound roughly at the same position predicted by the HF calculations, and this is probably the σ^* state predicted in Ref. [164]. The behavior of the bound part of this curve is incorrect, and a larger configuration space (we used roughly 10000 configurations in the scattering calculation) will be needed to get a quantitative result for these potential curves. Qualitatively though, our results confirm the predictions of Ref. [164], with the exception that a direct capture in the resonant state is not possible, so the dissociation has to happen either through a coupling with the dipole bound state (of the same symmetry) through vibrational Feshbach resonances, or through an out-of-plane motion that couples it to the π^* resonances.

5.2   DNA backbone

In this section (see also Ref. [195]), we analyze the behavior of the other subunits in the macromolecule, with the aim of investigating the electron interaction with the moieties that constitute the sugar-phosphate backbone, and verify whether they could
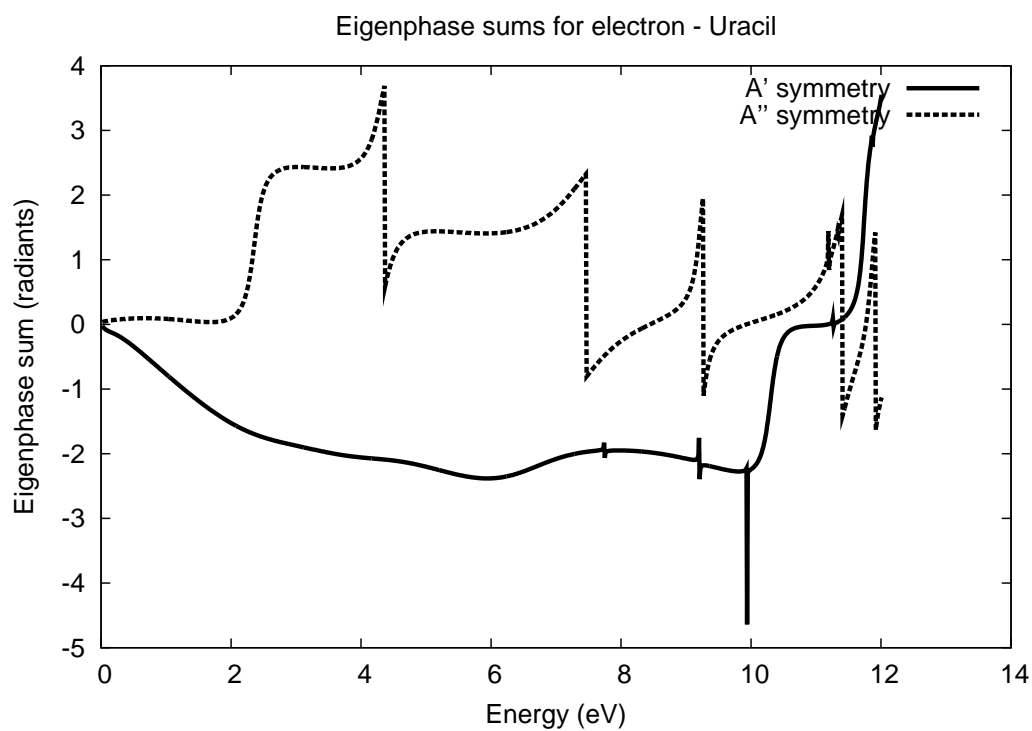
Figure 5.13: Eigenphase sums for the two symmetries (A' and A'') of the uracil molecule at the ground state equilibrium geometry as a function of energy. It is possible to notice that the A' channel has no low energy resonances, while the A'' has 3 shape resonances and many Feshbach resonances above 8eV. Note that the downward discontinuities are simply branch changes, rather than resonances.
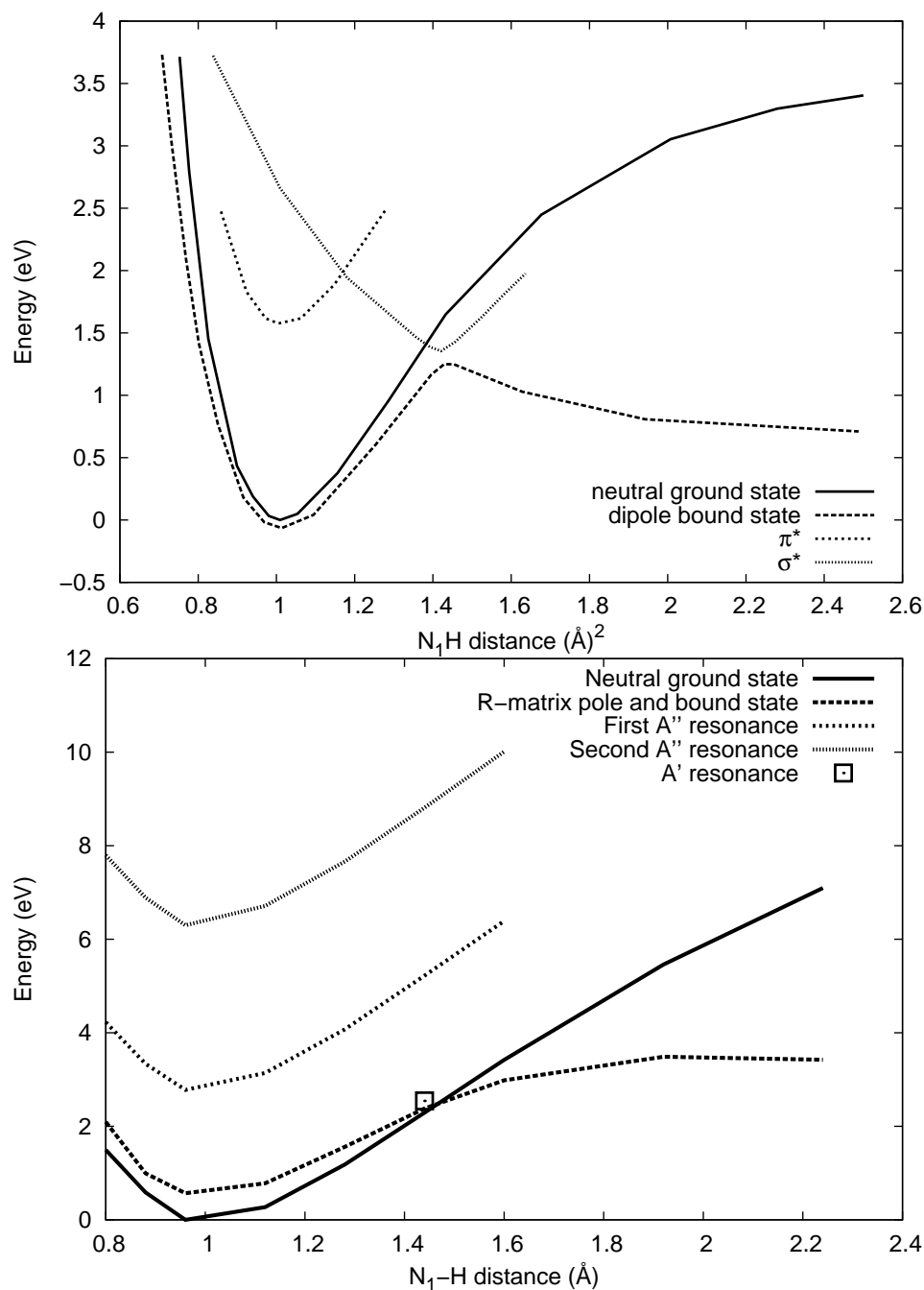
Figure 5.14: Top: potential energy curves for neutral uracil and the first few anionic states calculated at the Hartree-Fock level, based on calculations from from Ref. [164]. Bottom: energies of the ground state of the uracil molecule and its first few resonant anionic states. The π resonances are parallel to the ground state, while the σ state crosses it. Although the unbound part of the σ state is too wide to be detected as a resonance, at the N_1H distance where this state is just above the ionization threshold, a small resonance is seen, which is represented as a square in the figure. The long-dashed curve represents the first R-matrix pole when it is above the ionization threshold, whereas after it becomes bound it is the energy of the bound state.

play a role in the electron capture stage of the radiation damage process. In any case, it has been shown [153] that low energy electrons can damage the DNA sugar, deoxyribose (2-deoxy-D-ribose), and this interaction could be important in the cell environment. To model the sugar, we use tetrahydrofuran (THF, whose formula is C_4H_8O), which is similar to deoxyribose, except that the latter has -OH groups attached to the C_1 and C_3 and a CH_2OH side chain attached to the C_4 (the latter two substituents are linked to a phosphate group in the DNA molecule, while the former is linked to a base), they are substituted here by hydrogens. We use THF instead of deoxyribose because in DNA the OH groups are fundamentally modified by the phosphate and base that are attached to it (in fact the one attached to the C_1 disappears altogether), so we think that the solution would be either to consider a whole nucleotide or use THF, which mimics only the ring structure and is less affected by the rest. Another reason for this choice is that a recent study on dissociative electron attachment (DEA) from all the DNA components [6] has measured the average gas-phase DEA cross section from the bases as being very similar to the cross section *per base* for supercoiled DNA measured in Ref. [25]. This implies that the DEA cross sections for the sugar and phosphate groups are much smaller than those of the bases, which is what happens in the case of THF, but not for a hydroxy-substituted THF, where the DEA cross section is larger than for the bases. This suggests that THF could be a better molecule to model the sugar moiety in DNA. The structures of these compounds are represented schematically in Fig. 5.15. In practice, the DNA backbone can be thought of approximately as constituted by THF molecules to which the bases are attached, linked together by phosphate groups.

For the phosphate there are no previous results available for comparison, but for THF recently there have been both new experimental [131, 209] and theoretical [23]

results, with which we will compare our calculations. We will also attempt a comparison of the resonant wavefunctions to virtual orbitals from a Hartree-Fock calculation, in order to gain some more insights into the capture process and its possible consequences on the anion evolution. The conclusions suggested by this analysis lead us to draw a possible link between our calculations and experimental data on dissociative electron attachment.

5.3   Results: THF

In Fig. 5.16 our results are compared to the low-resolution experimental data of Zecca *et al.* [209] and the theoretical results of Bouchiha *et al.*, [23] obtained like ours without performing a Born closure to consider the effect of the dipole field on the higher partial waves. We also plot the data in the form of a time-delay, [194] to make the resonance position and width more evident. The total time-delay is the sum of the eigenvalues of the hermitian matrix Q of Eq. 5.1. In Fig. 5.16 we also plot the resonant channels, particular eigenvalues of the time-delay matrix that are larger than the others and show a Lorentzian behavior that sets them apart from the rest. We rescaled the total time-delay by dividing it by a factor, to show more easily everything in the same graph.

The order of magnitude of our cross section is not different from the results of Ref. [23], also calculated without Born closure. Since our calculations do not include excited states of the target, we will not be able to detect core-excited resonances (these were included in the calculations of Ref. [23]). The experimental total cross section contains also rotational and vibrational excitations and electronically inelastic channels, therefore it is to be expected to be larger than the elastic cross section. Our calculated elastic cross
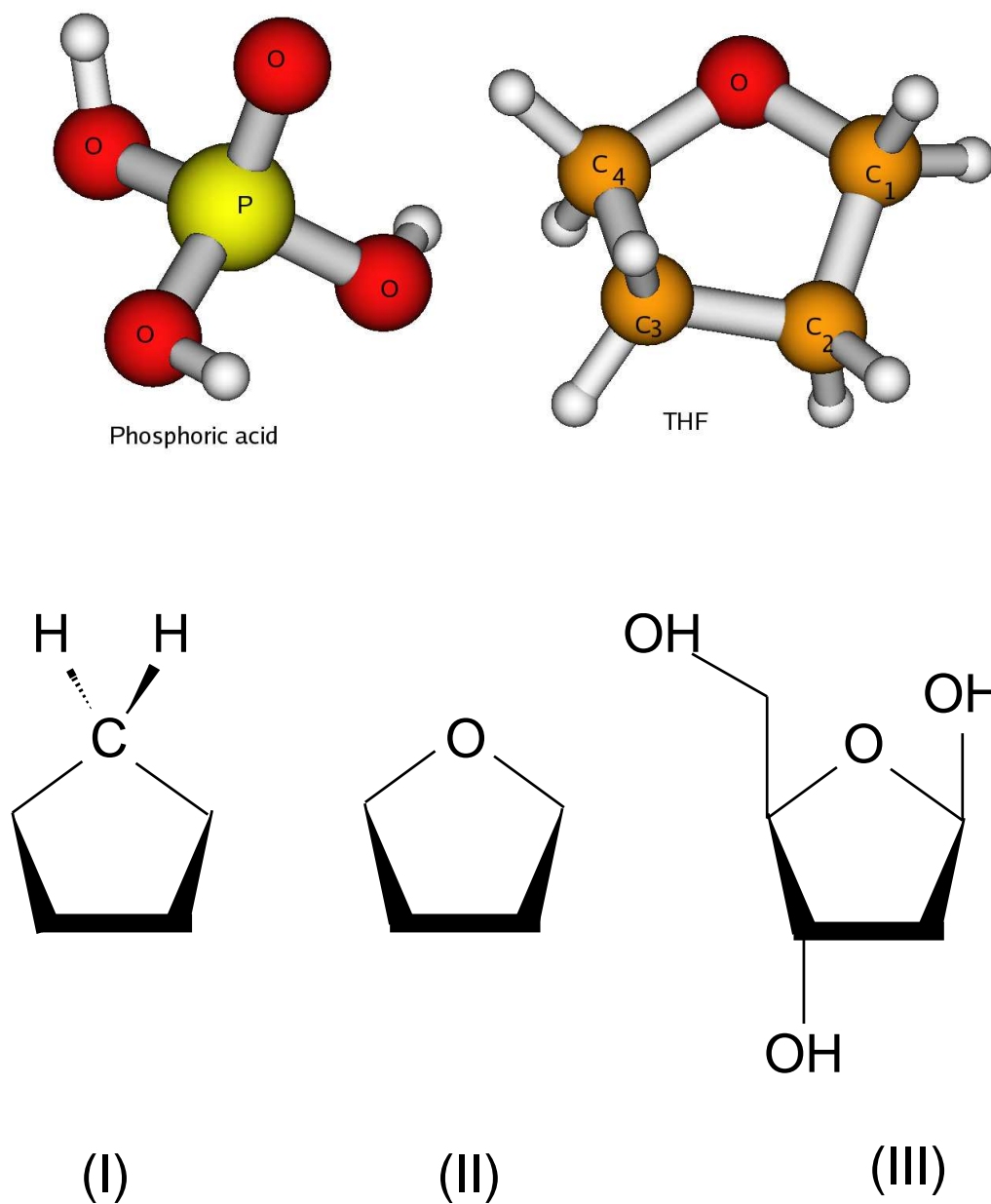
Figure 5.15: Top: Three dimensional structures of phosphoric acid and tetrahydrofuran. The small circles are hydrogen atoms. Bottom: Schematic structures of cyclopentane (1), THF (2), and the DNA sugar deoxyribose (3), that show the similarities between these compounds. The hydrogen atoms that fill the carbon valences are not shown. From Ref. [195].

sections lie instead above the experimental total cross sections of Ref. [209], and this is partly due to the approximate nature of our model. The comparison with experiment is difficult due to the effect of higher partial waves (with $l > 10$). The Born correction has been calculated in Ref. [23], and the cross section becomes higher than experiment, so we would expect a similar effect for our data. Due to the low resolution, the experimental results below 5 eV are (in the words of the authors) to be considered only indicative. The resonant structure that appears around 8.6 eV in our results looks similar to the analogous experimental feature, also taking into account that our model usually predicts resonances about 1-2 eV higher than their experimental position, as verified for the DNA bases [194] and also for molecules like carbon dioxide, benzene and SF_6 [193], because of the approximations adopted. This is due mostly to the adoption of a local exchange model, since for example, in a system like CO_2 [63, 102] this approximation causes a resonance shift of around 2 eV or so for model static-exchange, compared to all-electron static-exchange calculations, that is not possible to compensate with the polarization-correlation potential, which indeed shifts the resonance by a similar amount for this molecule (2.7 eV compared to 2 eV) with respect to correct polarization. Also the model polarization is approximate, but the model exchange constitutes the largest error in our calculations. Indeed, if we perform a purely static-exchange calculation (see Fig. 5.16) the position of the resonance (maximum of the time-delay) is at 11.2eV, 2.6 eV higher than the result including polarization, and it is composed of three overlapping resonances. For what we said above about the shifts generated by the model potential with respect to exact exchange, this resonance should be around 9 eV in an all-electron calculation; hence it should probably have been visible in the calculations of Ref. [23] that go up to 10 eV in energy. When polarization-correlation is added, this resonance

energy should fall below 10eV, and thus be clearly visible in the data of Ref. [23].

From the fact that our resonances are shifted too high in energy one might have thought that the widths would turn out to be larger than the experimental ones. We have verified in the past for many systems [193, 194] that our calculated widths are comparable to their correct values.

In fact no resonance was found in this energy range (0-10 eV) in the other published theoretical study [23]. Through a Lorentzian fit, we predict a width of about 2.3 eV for this resonance. At the static-exchange level, the resonance has a larger width, of about 3.0 eV. A higher energy resonance is found at 14.1 eV and it is even broader (about 2.5 eV). The partial wave contributions are mainly $l = 4$ (with a contribution of 70%) for the lower energy resonance, while for the higher energy resonance the largest are $l = 5$ (50%) and $l = 3$ (30%, as can be seen in Tab. 5.1). The partial wave decomposition will depend somewhat on the choice of the expansion center. We always perform the decomposition around the center of mass of the molecule, which seems a reasonable choice. The exception is the calculation of HeH^+ quantum defects in Sec. 4.3.1, where the center of charge was instead used.

To better understand the reason for the difference between our results and the ones in Ref. [23] and to make sure that our results are consistent with other known results, we have first of all performed a time-delay analysis [74, 174] of our scattering data, shown on the bottom of Fig. 5.16. This has allowed us to establish the presence of three superimposed resonances, two of which peak at 8.1 eV (with one significantly more intense than the other) while the third peaks around 9eV, and its intensity falls between the other two. Due to the large width of these resonances, the weakest of the channels in Fig. 5.16 has a time-delay eigenvalue which is not much larger than the
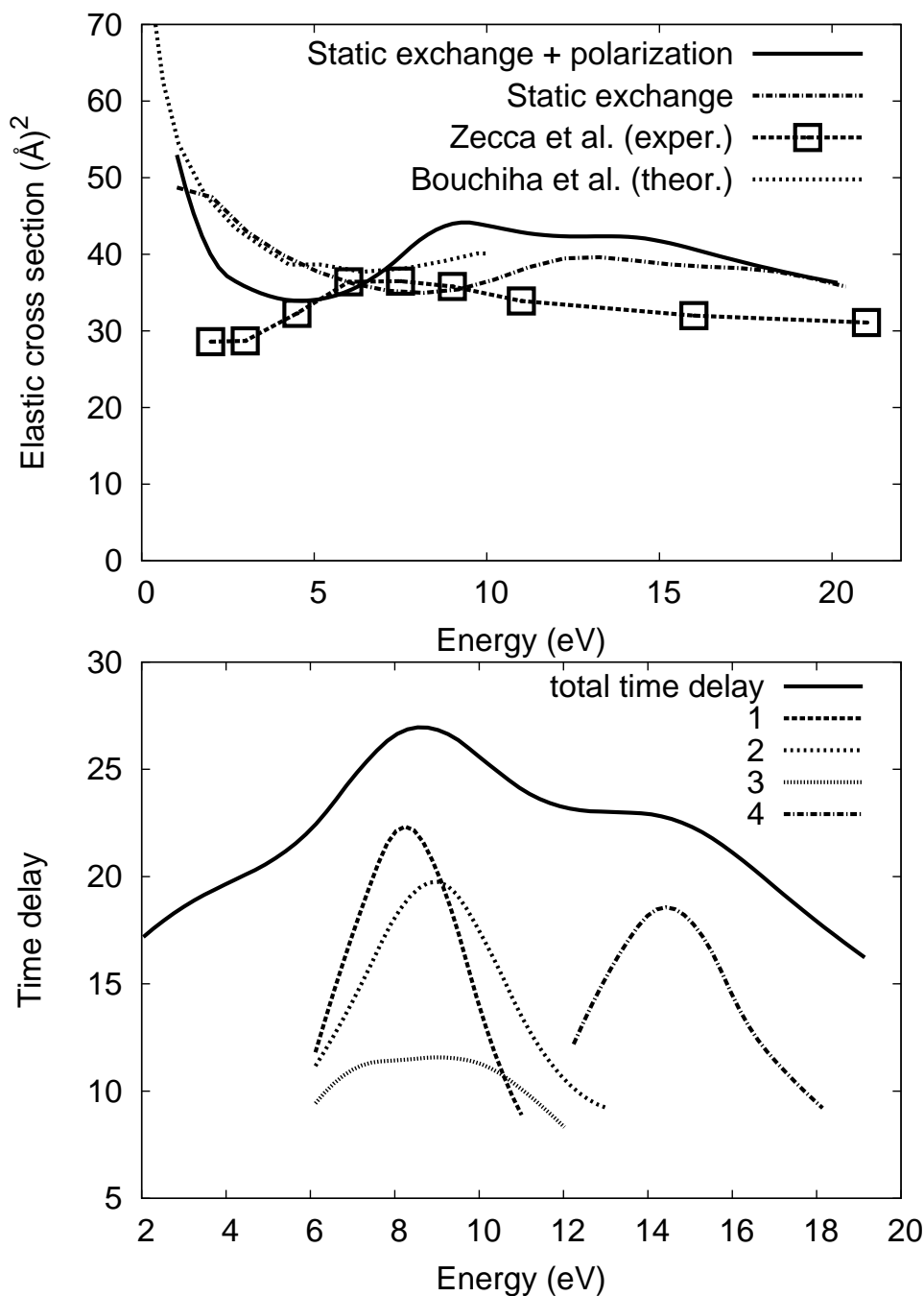
Figure 5.16: Top: partial elastic electron scattering cross sections from THF (solid line), the dot-dashed line represents the static-exchange results. Calculations involve partial waves up to l=10, for which the dipole physics outside the R-matrix box is included exactly. Comparison with theoretical (dotted) [23] and experimental (dashed) [209] results, the open squares are experimental data points. Bottom: time-delay plot to highlight the presence of resonances. The full curve is the total time delay, rescaled by a factor of 6 to show all curves on the same graph more easily, while the numbered curves correspond to the few highest eigenvalues that exhibit resonant behavior. From Ref. [195].

nonresonant eigenvalues.

An existing calculation for cyclopropane [37] (C_3H_6) shows that this cycloalkane has a cross section with a similar resonant structure at 6 eV. It is superimposed on a broader resonance at higher energy and other nonresonant contributions that give a very wide plateau, although in this case the first feature is not a composite resonance. The symmetry of the cyclopropane resonance in Ref. [37] is even with respect to the plane of the three carbon atoms, and the same occurs in THF, in the sense that although this compound is not planar, our resonance structures do not change sign above and below the ring bonds. It is plausible then that due to its larger frame and density of virtual orbitals, THF is able of supporting more quasi-degenerate resonant states at a similar energy.

Since there are no other existing experimental data on THF, we have performed calculations for cyclopentane (C_5H_{10}), which is very similar to THF except that here the oxygen atom is substituted with a -CH_2- group. For this molecule, experimental data [92] show a broad shape resonance at 8eV. The similarity of the two molecules suggests that many features of the cross section will be analogous. The results are compared to THF in Fig. 5.17. The cross section closely resembles that of THF, with a triple resonance superimposed on a broad higher energy resonance centered around 14 eV, which produces a wide plateau. The electron scattering cross sections for alkanes and cycloalkanes of different sizes have very similar behaviors, [92, 178] namely the same resonant structures and a magnitude dependent on the number of carbon atoms. Our evidence thus suggests that THF, being very similar to a cycloalkane, shares these common features, as suggested also in Ref. [209]. Also the cross section for cyclopentane is, in our calculations, larger than in THF, a trend that seems to be confirmed by the

experimental data [178, 209]. The cyclopentane cross section peak is roughly 48 Å^2 which is close to the experimental value [92] for the total cross section. Recent theoretical calculations [196], performed on a THF molecule distorted to achieve a planar geometry for the furanose ring, show results similar to ours, with a double shape resonance in a similar energy range.

As in Ref. [194] we attempt to correlate the spatial shape of the resonant wavefunction with the Hartree-Fock virtual orbitals obtained with a small (6-31G**) basis set. In this case the analysis is complicated by the fact that the molecules are not planar, so a projection on a two-dimensional surface would not pass through all the nuclei and, since the resonance is wide, different contributions mix and overlap. However, we have established that the resonant wavefunction at its peak resembles closely a virtual orbital with energy of 7 eV (orbital 23). At higher energy (around 9.5 eV, when the second resonant contribution becomes dominant), the resonance spatial structure appears similar to an orbital of 11 eV of energy (orbital 31). We show this in Fig. 5.18. Since there is a great degree of resonance overlap, the relationship of the resonant wavefunctions to the virtual orbitals we show becomes even clearer when observing the other virtual orbitals, because they are actually very different from our wavefunctions.

Recently, dissociative electron attachment (DEA) cross sections have been measured [6] for all the DNA subunits. These cross sections display two prominent resonances at 6 and 8 eV, of width around 1 eV each for THF, which could correlate with the calculated shape resonance, although clearly much complicated vibrational dynamics happens between electron capture and dissociation that we do not take into account here, and in the results of Ref. [23] there are electronically inelastic resonances in this energy region which could lead to similar outcomes in DEA.
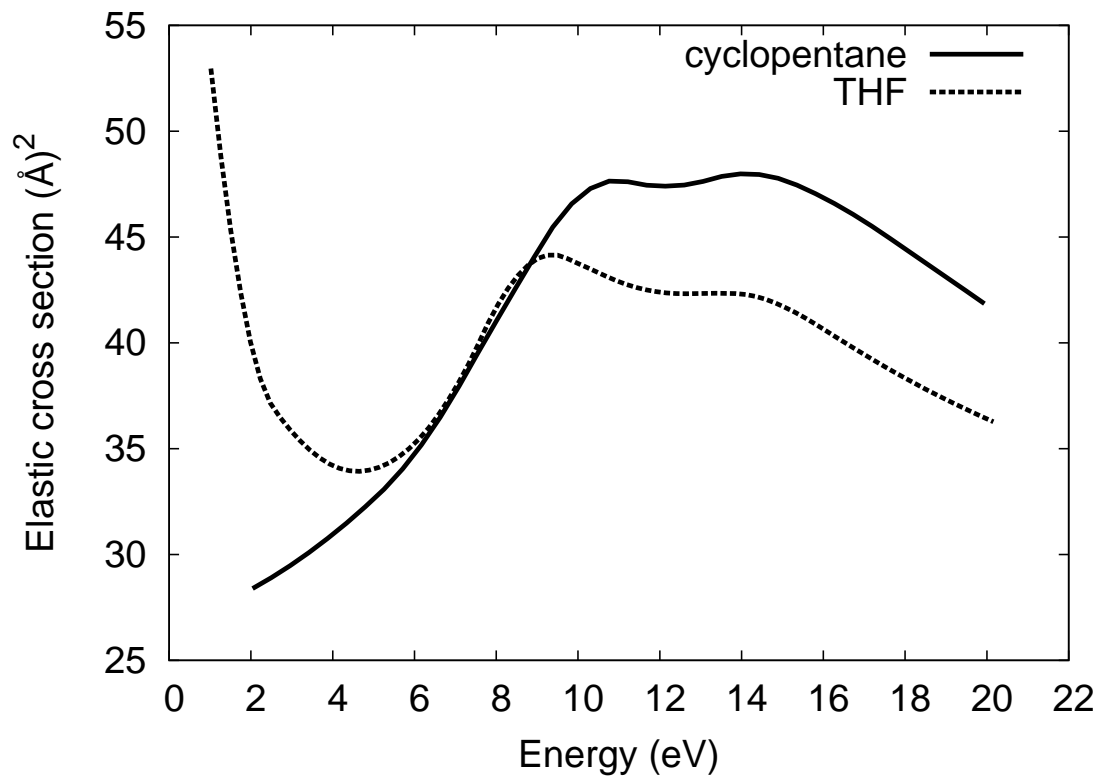
Figure 5.17: Partial fixed nuclei elastic cross sections for electron scattering by THF and cyclopentane. The two molecular structures are similar (THF has an oxygen atom instead of a -CH$_2$- group) and so are their electron scattering cross sections. Cyclopentane has essentially zero dipole moment, and therefore the low energy part of its cross section does not rise the way it does in THF. From Ref. [195].
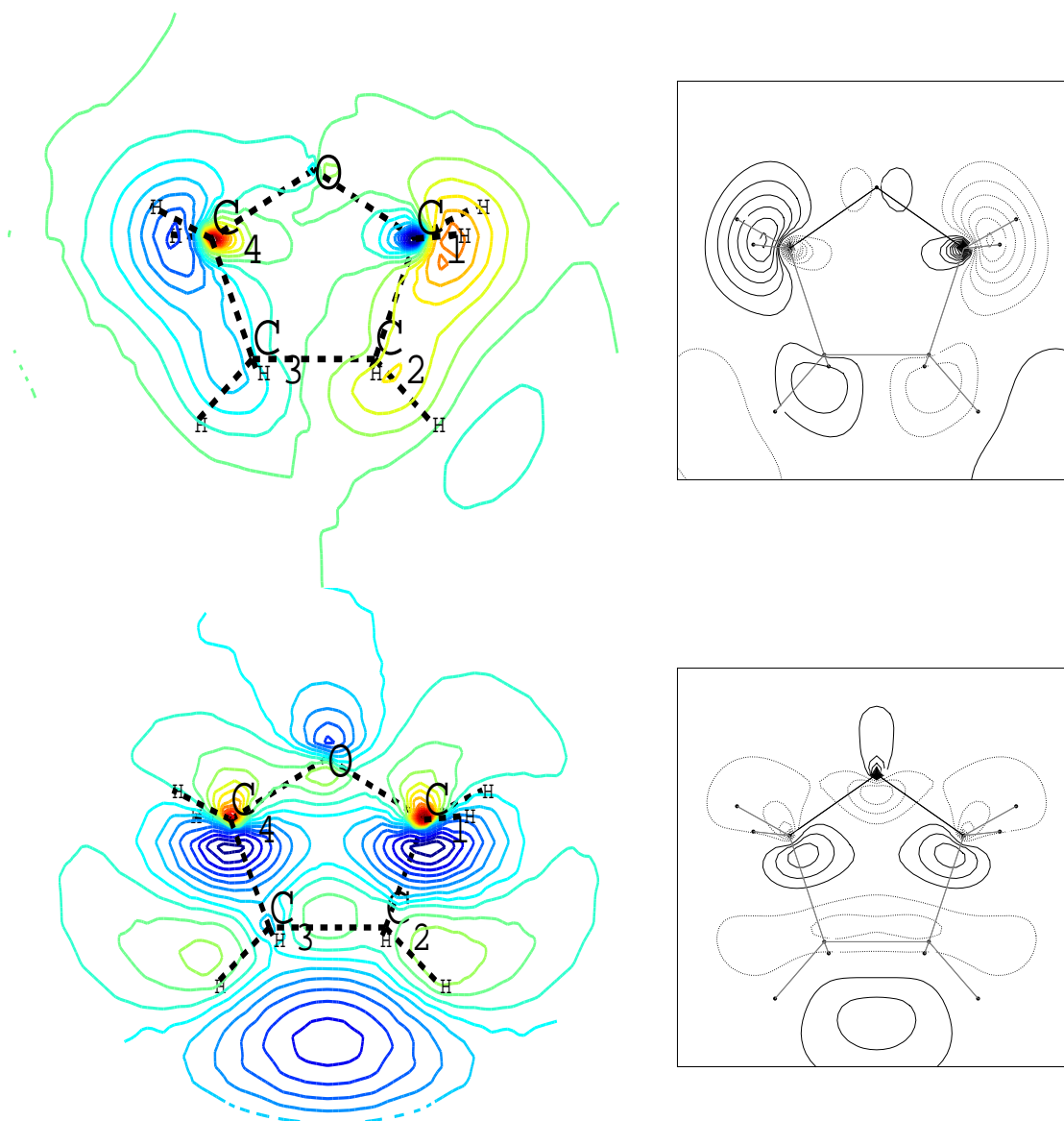
Figure 5.18: (Left: Time delay eigenfunctions for THF on resonance at 8eV (top, where the widely-spaced dotted curve (labeled "2") in Fig. 5.16 is dominant) and 9.5eV (bottom, where instead the dashed curve (labeled "1") in Fig. 5.16 dominates). A slice of the three dimensional eigenfunctions is shown, on the plane that contains OC_1C_4, while C_3 is above the plane and C_2 below. The red and yellow contours identify positive areas, while the blue are negative areas of the real part of the wavefunction. Right: virtual orbitals for energies around 7 (top) and 11 eV (bottom) from HF at the 6-31G** level. The full lines identify positive areas and the broken lines negative areas. The correspondence between the two top plots with each other and between two bottom plots is very pronounced, allowing us to identify the two main contributions to the resonance. Although the molecule is not planar this projection is much easier to read than the three dimensional structures. From Ref. [195].

Several electron-energy-loss (EEL) studies of THF [26, 108] and cyclopentane [7] have been performed, and some attempts have been made at assigning the resonances, also in relation to the position of the excited states from absorption spectroscopy. In Ref. [26] a gas-phase EEL peak for THF at 6.6 eV is assigned as a core-excited resonance with a parent ion of Rydberg character, centered on the oxygen atom. A similar experimental peak in cyclopentane in Ref. [7] is assigned as a shape resonance, on the basis of a molecular orbital argument, with the electron wavefunction distributed around the whole ring. Our calculations seem to agree with this second assignment, for two reasons: first, the resonance is very similar in character in THF and cyclopentane (see Fig. 5.17), and therefore it seems implausible that it derives from excitations on the oxygen; second, the resonant wavefunctions in Fig. 5.18 are found to be delocalized over the entire ring as had been speculated in Ref. [7] for cyclopentane. At higher energies core-excited contributions are most likely predominant, as was suggested in Ref. [108].

It is difficult to attempt a prediction of what the evolution of the resonances found in elastic scattering could be, when the nuclear dynamics is included. At present this incorporation of nuclear motion would be computationally prohibitive, but a first analysis can be attempted by inspecting our calculated results. From the spatial structures of the resonant wavefunctions it seems likely that the resonances could initiate a break-up of the ring, because of the presence of many nodal surfaces cutting through the ring bonds. For example, the experimental DEA cross sections for deoxyribose in Ref. [153] exhibit a peak at around 6 eV for production of the anion $C_3H_5O_3^-$, which could be generated by a resonant structure that shows a node cutting through the ring from C_3 to C_1, similar to the top left plot in Fig. 5.18, given that deoxyribose has side groups attached to C_4 and C_3 that could lead to production of the aforementioned

Molecule	Energy (eV)	Width (eV)	Partial wave
THF	8.6	2.3	4 (70%)
	14.1	2.5	5 (50%)
H_3PO_4	7.7	2.0	4 (42%)
	12.5	1.5	4 (41%)

Table 5.2: Energies, widths and largest partial waves of the resonances discussed in the text for the DNA backbone components. From Ref. [195].

anion.

5.4   Results: H_3PO_4

In the case of phosphoric acid there are no available theoretical or experimental data to compare with, and consequently our analysis of the results will be somewhat more limited. The cross sections show two prominent resonances, one at 7.7 eV and the other at 12.5 eV, with respective widths 2.0 eV and 1.5 eV. The main partial wave contributions are $l = 4$ and $l = 3$ at 40% and 30% respectively for both resonances, as stated in Tab. 5.2. At low energies there is a sharp rise in cross section due to the dipole moment. Cross section and total time delay are illustrated in Fig. 5.19. It is difficult to say why the second resonance is narrower than the first, since this is somewhat counterintuitive. We will limit ourselves to pointing out that in a complicated polyatomic molecule, shape resonance widths depend not only on the total energy, but also the size of the probability density near the escape regions in the multidimensional potential. It is possible, therefore, that a higher-energy resonance could be narrower than one at lower energy. Resonances broader at lower energy than the higher energy ones can be seen, for example, in C_{60} fullerene [117, 206].

In Ref. [6] the DEA cross section has been measured for trimethylphosphate ($PO_4(CH_3)_3$), and it displays a very wide and prominent resonant structure at 7.5 eV,

to which our 7.7 eV resonance could correlate. No branching ratio has been measured for this compound. The structure of phosphoric acid presents three identical -OH groups and therefore the resonances will show structures with a similar probability for the scattering electron to end up in each of these groups, making for complicated spatial profiles, which in the end have not proven to be very illuminating. For these reasons we will not attempt here an analysis of the spatial structure of the resonances.

As in THF, the shape resonances are quite broad, so the anions will be relatively short lived, and probably they will autoionize back (possibly with vibrational excitation) before having the possibility to trigger a breakup or energy transfer to another DNA subunit. However, the presence of water, a structural component in biological DNA, can act to stabilize the anions, and probably will significantly influence the lifetimes of these resonances in the cell nucleus since the backbone is in closer contact with the surrounding environment, compared to the bases that lie inside the double helix.

5.5   Outlook

The next aspect of the DNA radiation problem we want to explore is the coherent interaction of DNA subunits and their effect on the electron scattering/capture process. This can be accomplished in a multiple scattering framework (see e.g. Refs. [29, 41]) using the scattering data we gathered for the single components of the macromolecule, and it is currently under way in collaboration with Profs. L. Sanche and L. Caron at the University of Sherbrooke.
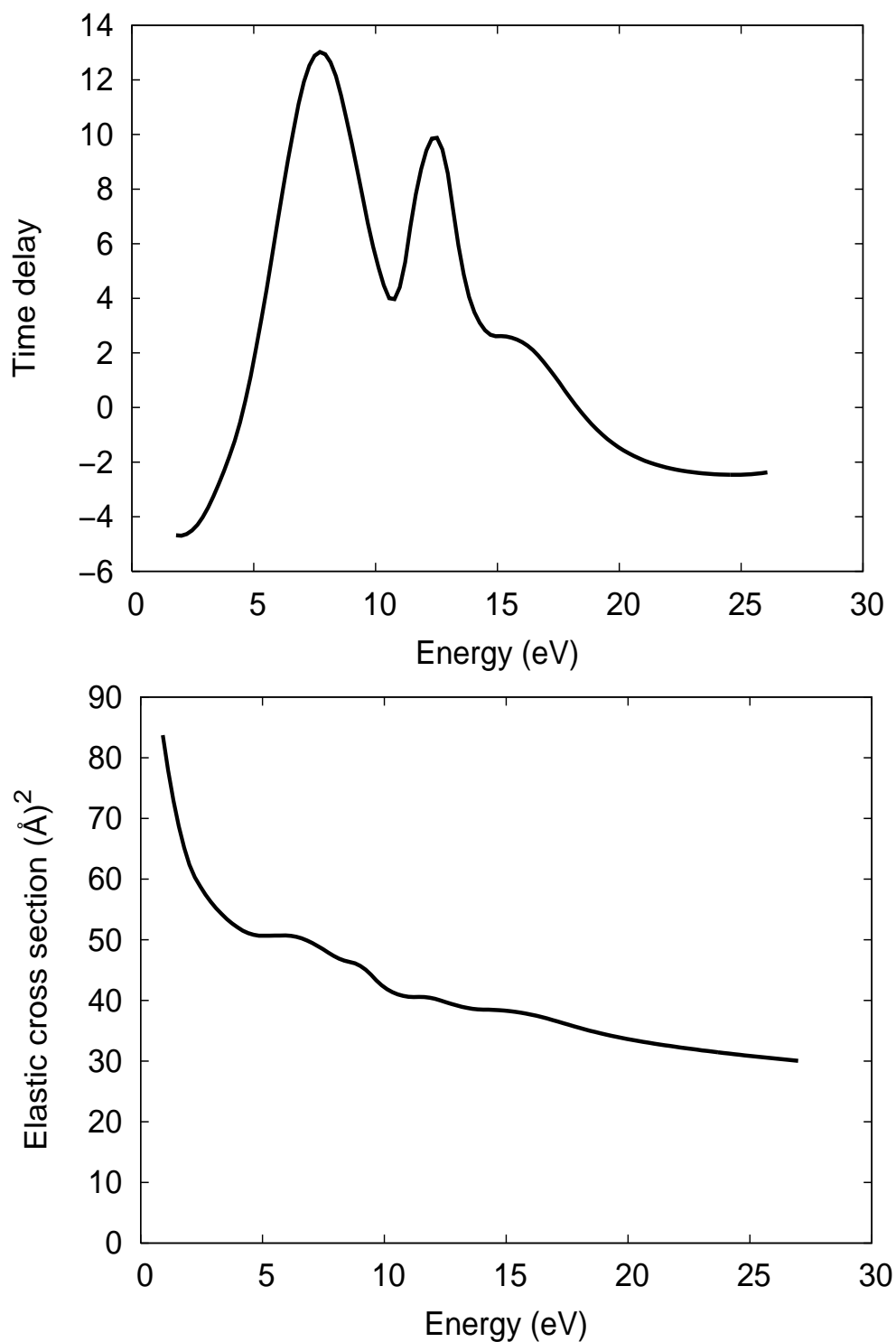
Figure 5.19: e-H_3PO_4 partial cross section (top) and time-delay analysis (bottom). Calculations again involve partial waves up to l=10 and the dipole physics outside the R-matrix box is included exactly for those partial waves. Two broad resonances are present, at 7.7 and 12.5 eV, the cross section is smaller than in the DNA bases and comparable to THF. From Ref. [195].

Chapter 6

Results: dissociative recombination

6.1 Introduction

In dissociative recombination, we have studied extensively the HCO^+ molecule, which is interesting for many reasons. In particular, it is an important astrochemical species, the ion is linear and therefore the neutral exhibits Renner-Teller coupling, it possesses conical intersections, the reaction mechanism is controversial and previous theoretical calculations of the rate coefficient are orders of magnitude lower than the experimental values. We illustrate these points more extensively below.

The HCO^+ molecular ion is one of the key ions in the chemistry of interstellar clouds. The major destruction channel of this ion is believed to be dissociative recombination (DR) by low-energy electrons. Therefore it is crucial to study electron collisions with HCO^+ ions. Numerous experimental studies have been carried out on this reaction using different techniques, such as stationary afterglows [110], flowing afterglows [3, 4, 106], a merged beam study [144] and, very recently, a storage ring experiment [56]. The thermal rate coefficient at 300 K is found in several studies to be about $2.0 \cdot 10^{-7}$ $cm^3 s^{-1}$ [106]. Its temperature dependence is stronger than the $T^{-0.5}$ dependence usually found when DR is driven by the direct mechanism where an excited neutral diabatic

state is crossing the ionic ground state close to its minimum. Therefore it has been proposed that there is no direct mechanism for DR of HCO$^+$ and instead the process is driven by electron capture into ro-vibrationally excited Rydberg states [110]. The temperature dependence of the DR rate has been measured in Ref. [144] as T$^{-1.2}$, which should be viewed as schematic, since it is not consistent with the known analytical threshold behavior. The DR cross section has been measured in the two ion-beam experiments [56, 144]. The cross section measured by Le Padellec *et al.* [144] is up to an order of magnitude smaller than that measured by Geppert *et al.* [56]. Absorption measurements [4], and recently the storage ring experiment [56], have shown a complete dominance of dissociation into H+CO. It has been long known that the CH+O channel is endothermic by 0.17 eV and could have an energy barrier, while the OH product is not observed (see Ref. [144] and references therein). Recently, branching ratios have been measured [57] for the DCO$^+$ dissociative recombination, confirming that the D+CO channel is by far the dominant one, with a ratio of 0.88.

Relevant in this context is also the series of experimental publications on autoionization of HCO Rydberg states carried out by Grant *et al.* [122, 123, 124, 157, 211], with which we will compare some of our results.

The DR mechanism of HCO$^+$ is controversial. Even though the temperature dependence of the DR rate suggests an indirect mechanism, the two existing theoretical studies predict different pathways. Kraemer and Hazi [99, 100] carried out complete active space SCF (CASSCF) calculations at linear geometry on the ground state of HCO$^+$ and some of the excited states of HCO relevant for DR. No indications were found of a neutral state crossing the ionic ground state near the minimum. However, in the studies by Talbi *et al.* [184] carried out at linear geometry, a direct mechanism for DR of

HCO$^+$ was proposed on the basis of multi-reference configuration interaction (MRCI) calculations with localized orbitals. Using a diabatization procedure, the adiabatic potential curves generated a repulsive neutral state crossing the ionic ground state near the minimum. This diabatization procedure seems questionable, as discussed for example in Ref. [18] where instead a multi-step mechanism has been proposed, in which the electron capture and dissociation proceed through a series of $\Delta v = 1$ transitions between Rydberg states of HCO.

One of the main goals of this study is to establish the reaction mechanism. To do this, accurate quantum chemistry calculations of both valence and Rydberg states of HCO have been performed. The Renner-Teller effect is strong in the ground ($\tilde{X}\,^2A'$) and first excited ($\tilde{A}\,^2A''$) states of HCO [67], so we need to assess its importance for the electron capture and predissociation in DR, as the similar Jahn-Teller effect was found to be crucial in DR of H$_3^+$ [94, 95]. Also this system shows a conical intersection [185], which in many molecules can provide a fast route towards the reaction products. Its influence on the dissociative recombination process needs to be understood as well. Conical intersections are understood now to be frequently occurring [208] rather than exceptions.

6.2   Model 1: no Renner-Teller couplings

This section illustrates the results obtained for this reaction using Model 1 as described in Sec. 3.2-3.4. The description of the *ab initio* results for the electronic potential energy surfaces is identical for the two models.

6.2.1   Ab initio surfaces

To calculate the potential energy surfaces of HCO^+ and HCO we used the MOL-PRO program package [203]. In order to calculate all the Rydberg states desired, a basis set with enough diffuse basis functions is necessary. We started with the aug-cc-VPTZ basis set [44] to which we added diffuse s-, p- and d- functions manually. For each new diffuse function, the exponent was decreased by a factor of 2.5 for the s- and p-functions, and by a factor of 3.0 for the d- functions. From Koopmans' theorem [181] we know that the virtual molecular orbitals of the HCO^+ ion with negative energies will approximately describe the Rydberg orbitals of the neutral HCO molecule. We therefore added diffuse functions to the basis set until the desired Rydberg states were converged. In the final calculation, we added up to 9s functions, 9p functions and 5d functions. From the orbital energies, we concluded that up to 12 Rydberg states of A' symmetry and 6 Rydberg states of A'' symmetry were converged. Then we calculated the potential energy surface of the ion, the 8 lowest states of A' symmetry and the 4 lowest states of A'' symmetry by starting with a HF calculation of the ion followed by a MRCI calculation. The advantage of starting with a HF calculation of the ion even when the neutral is studied, is that then we know, according to Koopmans' theorem, that the MOs will be suitable for describing the Rydberg states. The calculation may not be ideal for the valence states. The CI wavefunction is represented in a space of 4000 internal configurations and more than 1.2 million external configurations consisting of single and double excitations of the reference wavefunctions. We used the same active space for the calculations of the ion and neutral and therefore we believe that the relative energy between the charged and neutral states will be correct and the calculations

will be balanced. We need to calculate the potential energy surfaces as functions of all three internal coordinates (r_{CH}, r_{CO} and θ, the bending angle) and this would be very time-consuming using the MRCI method. We therefore once again employed Koopmans' theorem and approximated the energies of the Rydberg states using the ionic energy calculated with the MRCI method plus the orbital energy of the corresponding Rydberg state.

Since the orbital energies are negative, the Rydberg potential energy surfaces will fall at a lower energy than the ion potential. In this approach we neglect the correlation between the Rydberg electron and the ion core. The correlations among the electrons sitting on the ion are included since we use the correlated MRCI potential for the ion. Comparing the potential energy surfaces calculated using the MRCI method against those obtained from Koopmans' theorem, the MRCI results were lower in energy because they incorporate more electron correlation. Fig. 6.1 shows the calculated potential energy surfaces of HCO^+ and HCO at linear (θ=180 degrees) and bent (θ=150 degrees) geometries and $r_{CO} = 2.0877\ a_0$. The squares are the energies calculated with the MRCI method and the lines are from the approximation using Koopmans' theorem.

The ion is the curve with black squares. The filled squares (solid lines) are states of A' symmetry, while open squares (dotted lines) are states of A'' symmetry. Notice that there is no curve-crossing of a repulsive neutral state with the ionic ground state close to its minimum. The first excited neutral repulsive state crosses the ionic ground state roughly 2 eV above threshold, at an r_{CH} distance of roughly 4 a_0, well outside the region important for DR at the low energies that are of interest here, therefore we have neglected it in the following. The repulsive state is of Σ symmetry at linear geometry and lies below the ionic curve at all r_{CH} distances. We therefore conclude that DR of

HCO^+ is driven by an indirect mechanism whose initial step is electron capture into the Rydberg states. The effective quantum numbers are then calculated from the Rydberg formula, Eq. 2.35.

The agreement between the quantum defects calculated using the neutral MRCI potentials and Koopmans' theorem is remarkably good. We see that the states show Rydberg character (the effective quantum numbers in one series differ by 1) at least at small CH distances. Notice that some effective quantum numbers are close to 3.0. These are assumed to be d-states with almost zero quantum defects. The effective quantum numbers for linear and bent geometries are also shown in Fig. 6.1.

The next step was to fit the ion potential. The r_{CH} and r_{CO} dependencies were fit to Morse functions, and linear functions were used to fit the r_{CH} dependence of the Morse potential parameters. The ion-potential was fitted between 1.0 $a_0 \leq r_{CH} \leq$ 10.0 a_0, 90 degrees $\leq \theta \leq$ 180 degrees and for five r_{CO} distances (1.7877, 1.9, 2.0877, 2.3877 and 2.55 a_0). Then the quantum defects were fit to a model in which the σ levels have off-diagonal couplings, while the π part of the matrix is diagonal (Sec. 3.2). For the diagonal elements a fourth-order Taylor expansion was used, whereas the couplings were assumed to have a Gaussian form.

6.2.2   Vibrational dynamics

To calculate the vibrational frequencies of the HCO^+ ion, we have used the potential energy surface calculated by Palmieri *et al.* [154], since this was better suited to describe the ground state of the ion than the one we calculated. This is because our *ab initio* calculations are optimized for the Rydberg states energies, not just for the ground state surface. The difference between the two calculations is not very large, as
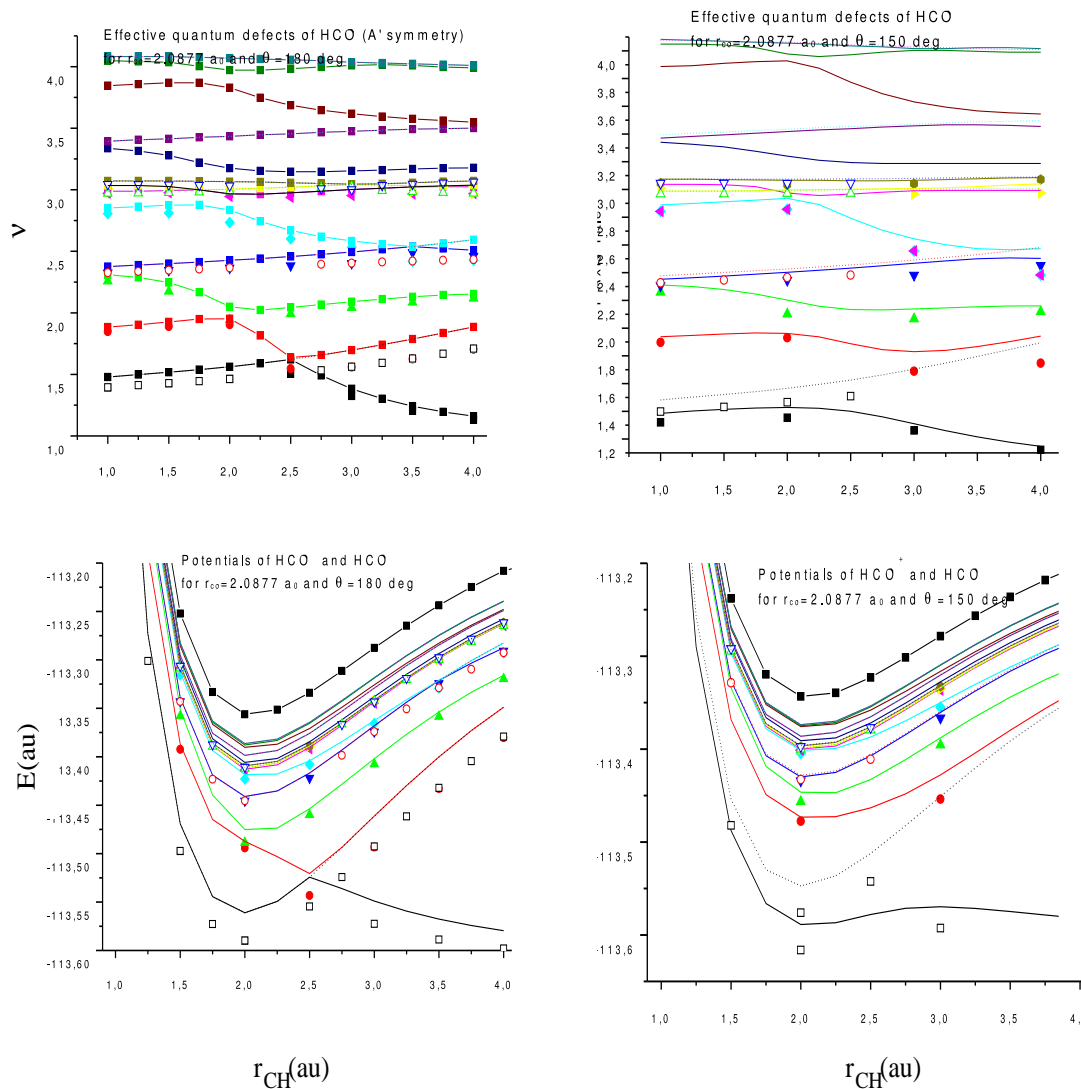
Figure 6.1: Potential energy curves (bottom) and quantum defects (top) for HCO. The dots are MRCI calculations, while the lines are calculated using Koopmans' theorem for the Rydberg states. The black line in the potential plots is the ground state of the ion. The solid lines and filled dots represent A' states, whereas the dashed lines and empty dots are A'' states. The left side of the figure has been calculated at a fixed angle $\theta = 180$ degrees (equilibrium value for the ion), while the right side has $\theta = 150$ degrees. In both cases r_{CO} is fixed at its equilibrium value of 2.0877 a_0

Table 6.1: Comparison of vibrational frequencies (in cm^{-1}) for vibrational transitions in HCO^{+}, calculated using the Palmieri ionic potential surface [154]. The second column reports values from Ref. [154], while the third is an adiabatic calculation and the fourth is a full three-dimensional diagonalization. The last column shows the frequencies obtained in an adiabatic framework using the potential we calculated, which we have used only for the Rydberg states in this work and not to obtain ionic vibrational frequencies, since the Palmieri potential was better suited for this purpose.

$(\nu_{CH}, \nu_{\theta}, \nu_{CO})$	$\nu_{Palmieri}$	$\nu_{Adiabatic}$	ν_{3D}	$\nu_{Adiab.\ Larson\ potential}$
020	1641	1630	1629	1739
001	2182	2195	2189	2299
100	3090	2930	3082	3150
040	3256	3188	3238	3460
021	3822	4087	3815	4044
002	4345	4514	4363	4678
120	4679		4658	

is shown in Tab. 6.1 where also a comparison between the adiabatic model and full three-dimensional calculations is shown. Since the coordinates mimic quite closely the normal modes of the molecules, the nonadiabatic couplings are limited and the adiabatic frequencies are largely correct for the lowest vibrational states.

As was mentioned in Ch. 3 we use Jacobi coordinates for the vibrational dynamics, and we only consider one fragmentation channel, due to the H+CO channel being largely dominant, as stated in Sec. 6.1.

6.2.3   Autoionization widths

To test the wave functions and quantum defects used in the present study we compare calculated autoionization widths with the measurements of Grant *et al.* [122, 123, 124, 157, 211] using high resolution double-resonance spectroscopy, as a function of the vibrational normal modes CO stretching and bending [123]. The vibrational wave functions for the C-H stretch have either zero boundary conditions on the left (box

Table 6.2: Calculated energies and widths of the autoionizing HCO resonances. Here n is the approximate principal quantum number and $(\nu_{CH}, \nu_\theta, \nu_{CO})$ is the ionic vibrational mode of the resonance. Γ_{box} is the width calculated using box-states, while $\Gamma_{Siegert}$ is calculated using Siegert states. The widths measured by Grant *et al.* [123] are displayed as Γ_{exp}. From Ref. [104].

Energy (H)	n	$(\nu_{CH}, \nu_\theta, \nu_{CO})$	Γ_{box} (cm^{-1})	$\Gamma_{Siegert}$ (cm^{-1})	Γ_{exp} (cm^{-1})
$8.65 \cdot 10^{-5}$	6	(1,0,0)	1	3	-
$3.13 \cdot 10^{-3}$	7	(1,0,0)	3	6	-
$2.12 \cdot 10^{-4}$	7	(0,0,1)	0.08	2	10
$2.30 \cdot 10^{-3}$	8	(0,0,1)	0.026	1	8
$6.50 \cdot 10^{-3}$	12	(1,0,0)	0.018	0.7	2.5
$2.30 \cdot 10^{-4}$	12	(0,1,0)	0.013	0.6	1.5
$7.53 \cdot 10^{-4}$	13	(0,1,0)	0.012	0.45	1.25

states, which describe only autoionization processes) or Siegert boundary conditions (the Siegert states described above, which allow for escaping flux due to predissociation). The resulting widths are displayed in Table 6.2. The measured widths are up to an order of magnitude larger than the calculated widths. The widths calculated using Siegert states are also an order of magnitude larger than those calculated with box states. This seems to indicate that predissociation is a determining factor in the autoionization dynamics. Notice also that the largest autoionization widths we calculate are for the CH stretch, for which no experimental data are available. For the other two normal modes the widths are comparable between each other (larger for CO stretching than bending, similarly to experiment), but they are very sensitive to predissociation, while this is true to a lesser extent for the CH stretching mode.

6.2.4   Electron scattering and cross section

In this first calculation, which includes no Renner-Teller coupling, we have used the Siegert states method (Sec. 3.4) for calculating the DR cross section. The results

are converged when we include 40 adiabatic states and 9 C-H Siegert states for each adiabatic potential. To converge these states, we need about 40 grid points in r and ϑ and 100 points for R. The resulting DR cross section is shown in Fig. 6.2.

It should be noted that the calculated cross section is overall smaller than the cross section measured by Le Padellec *et al.* [144], especially for $E \sim 0.01$ eV where the theoretical cross section drops several orders of magnitude. We have tried to estimate the effect of nonadiabatic couplings on the DR rate, using the complex absorbing potential [161] and complex scaling [133] methods. In both cases the effects have turned out to be quite small, therefore the adiabatic approximation is quite good for this system.

6.3   Model 2: inclusion of Renner-Teller couplings

In this section we show results for Model 2, described in Sec. 3.5-3.6. The main differences with respect to the previous model are the inclusion of Renner-Teller couplings, freezing of CO motion, and a different method to calculate the DR cross section.

We have calculated DR cross sections for two different initial vibrational states $\chi_v^+(R_{CH})$ of the ion: the ground state $v = 0$ (which can be viewed as $\{00^00\}$) and the first excited state $v = 1$ (which can be viewed as $\{01^10\}$) whose energies are represented in Fig. 3.5 with horizontal dotted lines. The energy difference between the two states is about 0.1 eV. Figure 6.3 shows the two cross sections with dot-dashed ($v = 0$) and dashed ($v = 1$) lines. Fig. 6.3 shows that the DR cross section depends strongly on the initial vibrational state. A similarly strong dependence has also been observed in experiments with other molecular ions. Assuming that the initial experimental vibrational state distribution is in thermodynamic equilibrium, it is necessary to average the
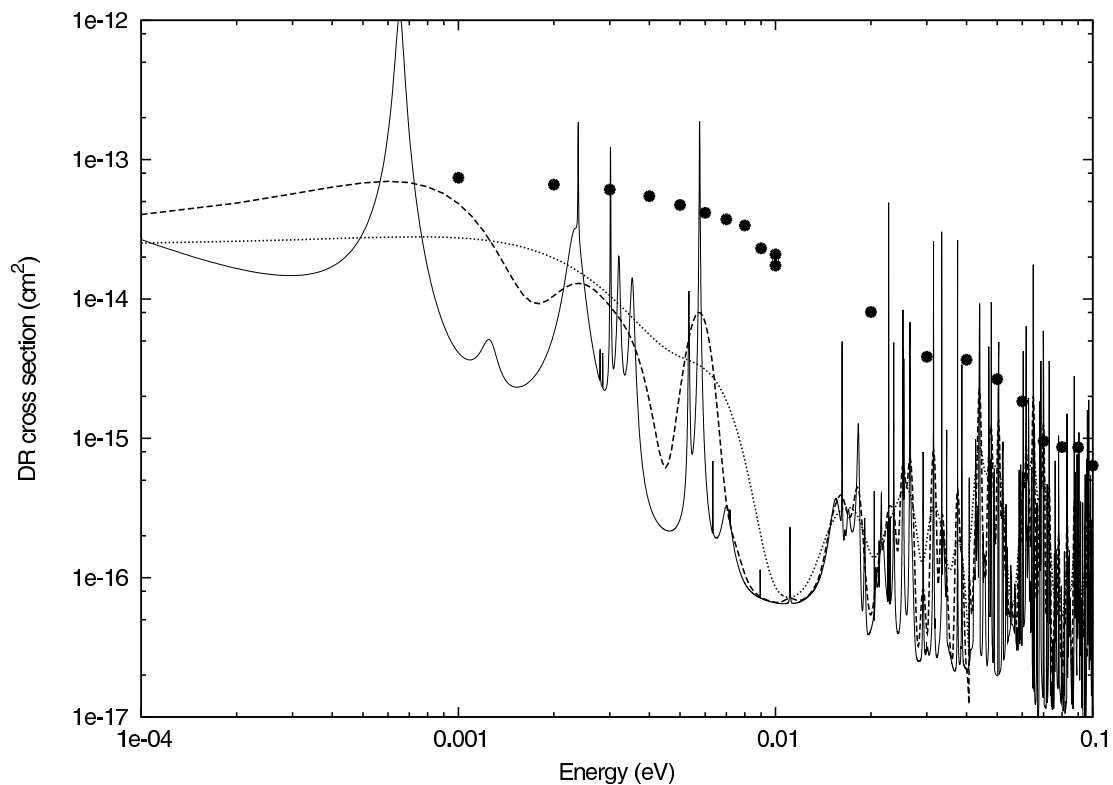
Figure 6.2: Dissociative recombination cross section obtained with the Siegert states method, using the model with no Renner-Teller couplings. Calculated (full line) and measured (circles) [144] cross sections for DR of HCO^+. To compare with the measured cross section, the calculated cross section has been convoluted with a 1 meV (dotted line) and 3 meV (dashed line) Gaussian energy distribution, this smoothes a large part of the Rydberg resonances that are not seen in experiment, since the resolution is too low. Here we do not consider rotational structure, which would increase the number of resonances. From Ref. [104].
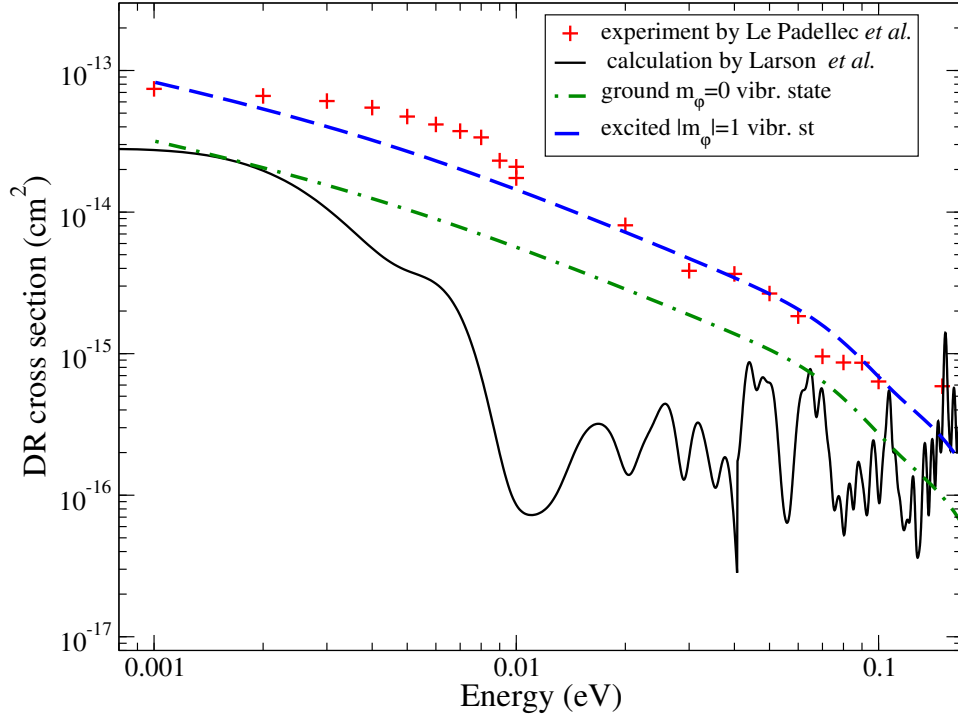
Figure 6.3: The figure shows the present theoretical DR cross section (dashed and dot-dashed lines) for HCO^+ as a function of the incident energy E. The initial vibrational state is the ionic ground state for the dot-dashed curve and the first excited state for the dashed curve. The experimental [144] (cross symbols) and previous theoretical [104] (thin solid line) cross sections are also shown for comparison. The theoretical curves include the averaging over the electron energy distribution according to the procedure described by Eq. (2) of Ref. [96] with $\Delta E_\perp = \Delta E_{||} = 3$ meV. From Ref. [130].

cross section over the thermal distribution to compare with the experiment. The first excited vibrational state has vibrational symmetry different from the ground state. The vibrational angular momenta for the states are $m_\varphi = 1$ and 0. Thus, the deexcitation process may be too slow to reach equilibrium, resulting in a vibrational temperature that is higher than the electron temperature (300K in the experiment of Ref. [144]). The vibrational temperature in the experiment of Le Padellec *et al.* [144] is not known. If it was in equilibrium with the electron temperature at 300K, the contribution from the excited vibrational states would be small. But for a larger vibrational temperature, for example 1000 K, the averaged cross section would be about a factor of 1.5 larger than the cross section for the ground vibrational state in Fig. 6.3. The fact that in several different experiments the measured DR rate ranges over values from $0.65 - 3 \times 10^{-7}$ cm^3/s at 300 K (see Ref. [3, 56, 106, 110, 158] and Fig. 6.4 below) might conceivably derive from differences in the initial vibrational populations. Determination of the actual experimental vibrational distribution and/or controlling it in HCO$^+$ could be an important step in understanding DR in small polyatomic ions.

The present theoretical DR cross section is approximately a factor of 2 smaller than the experimental data. Assuming that this reflects a limitation of the present theoretical description, this might derive from our approximation that freezes the CO bond length. However, the expected error of order 70% caused by our adiabatic approximation in the R_{CH} coordinate should also be kept in mind when assessing the implications of this discrepancy. Still, if the CO bond is allowed to vibrate, which makes the ion more floppy, the probabilities of capturing and predissociation will presumably be increased. Quantitatively, releasing the CO bond increases the density of HCO resonance states that can be populated in the electron-ion collision and, correspondingly, the sum in Eq.

3.26 is expected to increase.

In afterglow plasma experiments, the measured observable is the DR rate constant thermally averaged over the kinetic energy distribution of colliding electrons and ions, $\alpha(kT) = < v\sigma >$, where v is the velocity of the electron, is obtained from the DR cross section shown in Fig. 6.3 according to Eq. (7) of Ref. [94]. The resulting theoretical rates (thermally averaged over the electron energies, for each of the two initial vibrational states) are shown in Fig. (6.4) and compared with available experimental measurements.

Although the theoretical DR cross section is still smaller by a factor of 2 than the experimental results of Le Padellec *et al.* [144], we find that inclusion of Renner-Teller coupling significantly increases the theoretical DR cross section. The previous theoretical study by Larson *et al.* [104] that omitted Renner-Teller coupling, but which did account for the CO bond vibrations, gave a DR cross section significantly smaller than the present result. This is evidence for the important role of Renner-Teller coupling in the HCO^+ DR process.

Since the Born-Oppenheimer potential surfaces are the same for HCO (HCO^+) and DCO (DCO^+) we did a similar calculation for DR in DCO^+. The resulting DR cross sections for the ground and first excited vibrational level are very similar to the ones presented in Fig. 6.3 but smaller by a factor of 1.5. A similar dependence of the DR rate on the isotopologue masses was found in theory and experiment for the H_3^+, H_2D^+, D_2H^+, and D_3^+ ions [97]. Notice that the lifetime of the first excited vibrational state of DCO^+ is supposed to be very long, of the order of some ms [204], therefore it is even more important in this case to control the initial vibrational population.

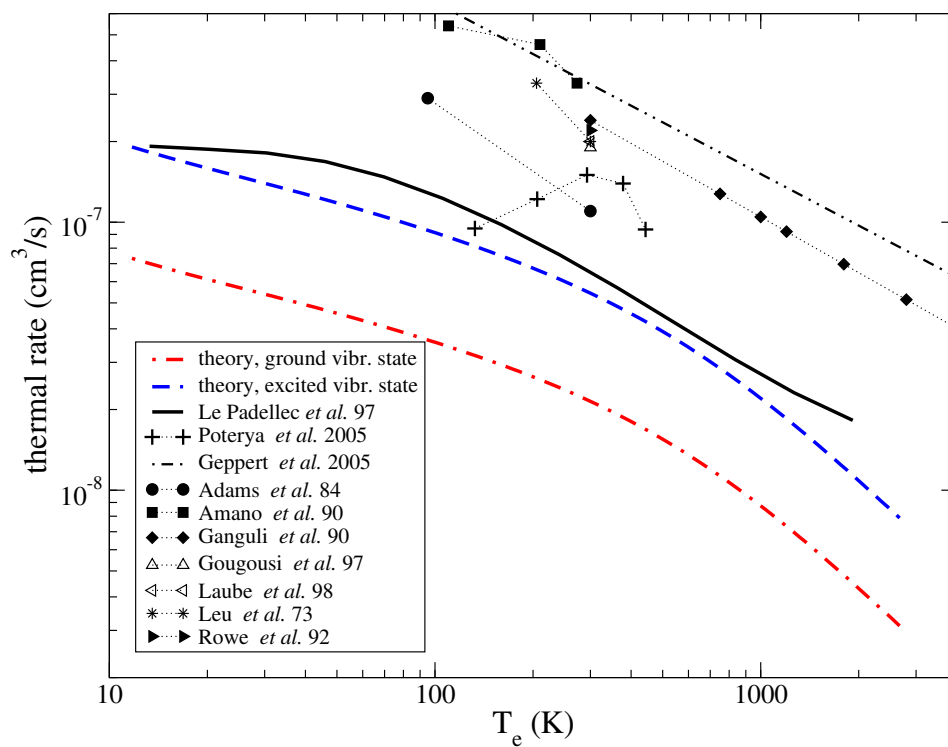Figure 6.4: Theoretical and experimental DR thermal rates for HCO^+. The dot-dashed and dashed lines are the theoretical rates obtained for the ground and first excited vibrational states of the ion. The experimental rate (solid line) is obtained from the experimental cross section, Ref. [144]. The results from a number of other experiments with HCO^+ [3, 56, 106, 110, 158] are also shown. From Ref. [130].

6.3.1 Estimation of the effect of autoionization and CO vibration on the cross section

We should mention some approximations made in the present study that can affect the theoretical DR cross section. First, our treatment has not accounted for the possible autoionization after the electron is captured by the ion, before the neutral molecule has time to predissociate: in Eq. (3.20), the survival probability $e^{-\rho(E)}$ was set to be 1. The inclusion of autoionization decreases the calculated DR cross section. The effect of autoionization on the DR cross section can be estimated as follows. Figure 6.5 shows the calculated resonance curves $U_a(R_{CH})$ as described above and in Ref. [94]. Above the lowest ionic curve each of these potential curves has in general a non-zero width $\Gamma_a(R_{CH})$, which represents the adiabatic autoionization rate. If there is more than one open ionic channel $|j\rangle$ for a given $U_a(R_{CH})$, the neutral molecule can decay into the i-th channel with a partial width $\Gamma_a^{(i)}(R_{CH})$, where $\sum_i \Gamma_a^{(i)}(R_{CH}) = \Gamma_a(R_{CH})$. Once the electron is captured, the system can evolve into two competing pathways: resulting in either autoionization or dissociation. The relative probabilities per unit of time for the two processes provide an estimate for the survival probability $e^{-\rho(E)}$.

The largest partial autoionization widths are in general the widths of the resonance curves $U_a(R_{CH})$ belonging to Rydberg series associated with a few nearest closed ionic channels. Such resonance curves are very similar in shape to their parent ion potential curves, when the principal quantum number n is high. Consequently, in the energy range of interest, these curves $U_a(R_{CH})$ are closed with respect to adiabatic dissociation. The dissociation can occur only through coupling to true dissociative states (i.e. the process denoted as predissociation in molecular spectroscopy). The predisso-
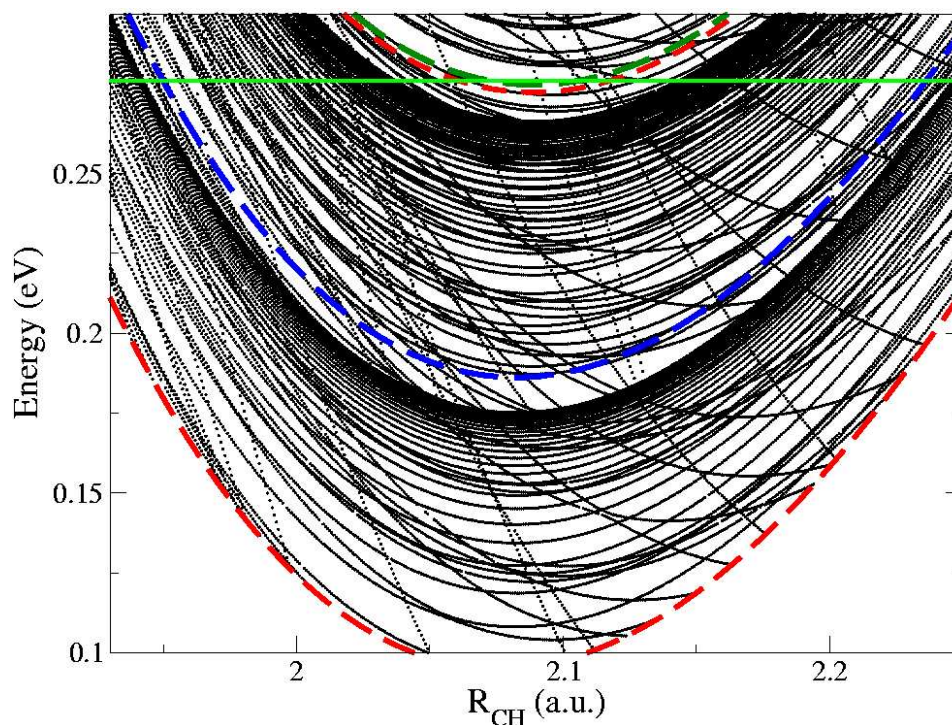
Figure 6.5: Resonance potential curves $U_a(R_{CH})$ of the neutral molecule states having magnetic quantum number $M = 1$. The potential curves were calculated in the energy range where at least one electron-ion channel $U_i^+(R_{CH})$ (for the given R_{CH}) is open. Thus, the lower bound of the calculated curves corresponds to the ground potential curve $U_{0,0}^+(R_{CH})$ of the ion. The potential curves of the ion are also shown by dashed thick lines (see also Fig. 3.5). The Rydberg series are crowded just below the ionic potential curves. For clarity, visible gaps between the Rydberg series and the ionic curves have been intentionally introduced artificially, to show the behavior of the resonance curves belonging to higher ionic channels. The horizontal line represents the energy of the ground vibrational level. From Ref. [130].

R_{CH} a.u.	Energy (eV)	α (a.u.)	ΔF (a.u.)	ΔE(a.u.)	$P_{a',a}$
2.056	0.112	1.18×10^{-5}	0.0041	0.0059	0.9×10^{-4}
2.11	0.144	2.9×10^{-5}	0.0111	0.0047	2×10^{-4}
1.93	0.34	4.0×10^{-5}	0.0036	$1\text{-}37 \times 10^{-4}$	$14 - 83 \times 10^{-4}$
2.02	0.283	1.0×10^{-5}	0.0022	$1\text{-}37 \times 10^{-4}$	$1.2 - 7.2 \times 10^{-4}$

Table 6.3: The table demonstrates Landau-Zener parameters and probabilities for typical avoided crossings. The first two examples correspond to avoided crossings situated deeply below the energy of the ground vibrational level. The third and fourth examples correspond to energies around and above the ground vibrational level. Thus, ΔE could be very different for the last two examples giving different probabilities. In general, for any total energy of the system there are always some avoided crossings with small ΔE at the corresponding turning points. From Ref. [130].

ciation probability can be estimated using the Landau-Zener model. When the neutral molecule is vibrating along the $U_a(R_{CH})$ curve, every time it passes through an avoided crossing with another curve $U_{a'}(R_{CH})$, it can jump to the corresponding state $|a'\rangle$ via an adiabatic transition. We view such an adiabatic transition as the pathway to pre-dissociation. The probability for adiabatic passage through an avoided crossing is given by the Landau-Zener formula [101]

$$P_{a',a} = 1 - \exp\left(-\frac{2\pi\alpha^2}{\Delta F}\sqrt{\frac{m}{2\Delta E}}\right) \approx \frac{2\pi\alpha^2}{\Delta F}\sqrt{\frac{m}{2\Delta E}} \tag{6.1}$$

where α is the non-diagonal coupling element between diabatic states, i.e. the states that would cross if the coupling was absent. Numerically, α is equal to half of the adiabatic potential curve splitting at the avoided crossing. ΔF is the absolute difference in slopes (net classical force) between crossing *diabatic* potential curves, ΔE is the classical kinetic energy at the avoided crossing, m is the reduced mass of the system. The resonance curves shown in Fig. 6.5 demonstrate numerous avoided crossings.

Table 6.3 indicates the order of magnitude of the parameters in Eq. 6.1. This table shows two examples of avoided crossings that lie well below the energy at which

the electron can be captured. At such large values of ΔE, the Landau-Zener probability is very small (10^{-4}) and depends only weakly on the electron energy. The other two examples are taken from the region around the left turning point where the velocity of motion can be small or large depending on the energy of the electron. In cases like this, we calculated the probability $P_{a',a}$ for a range of values of the kinetic energy ΔE. There are many such avoided crossings near left turning points and comparatively few at right turning points.

During half ($\tau_{1/2}$) of an oscillation period, the system goes through n_c avoided crossings. We estimate that n_c is about 10 for a typical resonance curve. Therefore, the total predissociation probability P_d is somewhere in the range 0.001-0.01. In the above estimation of the predissociation probability we have assumed that only two states interact at each avoided crossing. However, in reality many of the avoided crossing cannot be considered as strictly two-state ones: three or more states $|a\rangle$ can participate.

The autoionization probability P_{ion} during time $\tau_{1/2}$ is $P_{ion} \sim \tau_{1/2}\Gamma$, where Γ is the total autoionization width. The largest Γ is about 10^{-5} a.u., $\tau_{1/2} \sim \pi/\omega$, where $\omega/2$ is the frequency of oscillations in the ground vibrational level, $\hbar\omega/2 = 0.007$ a.u. Thus, $P_{ion} \sim \pi\Gamma/\omega \approx 0.002$. This is presumably an upper bound on the autoionization probability.

As one can see, the autoionization probability could be competitive with predissociation in our model if we take the smallest ratio $P_d/P_{ion} \sim 0.5$, but it is more likely that the ratio is of the order of 2-3 and therefore, more favorable to predissociation. In the previous theoretical study of DR in H_3^+ [94], the ratio was significantly larger. An important difference with the H_3^+ study is the two degrees of freedom taken into account when adiabatic potentials U_i^+ were calculated. As a result, the density of
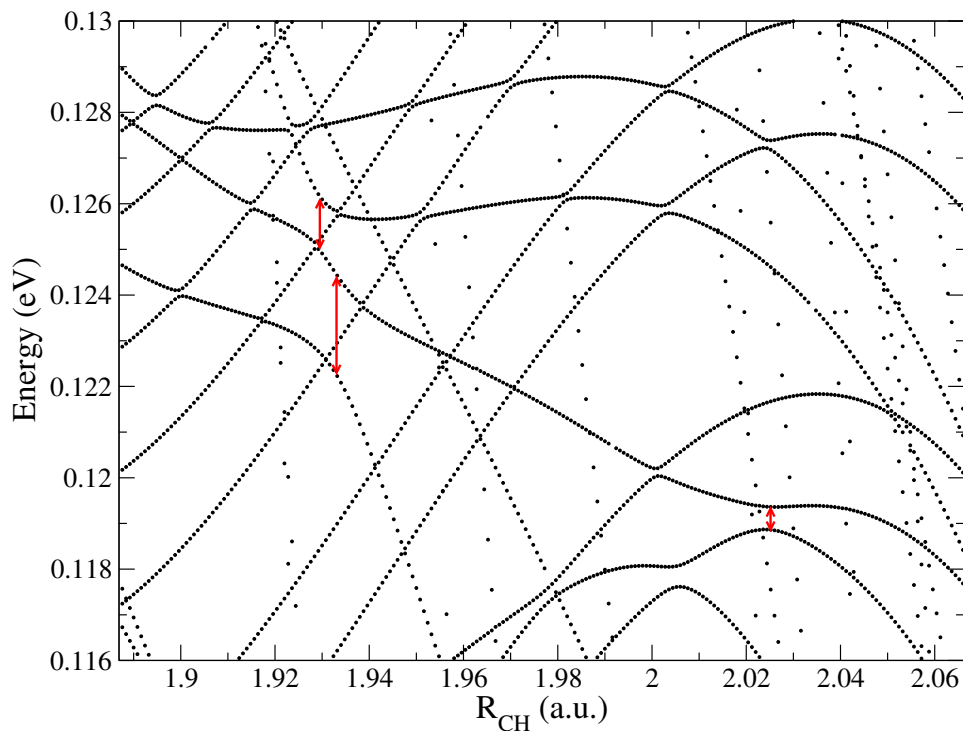
Figure 6.6: A part of the spectrum of Fig. 6.5 showing the interval of R_{CH} corresponding to the left turning point of the vibrational motion. For convenience, the energy of the ground ionic curve $U_{0,0}^+(R_{CH})$ was subtracted from all the data. In the figure, curves with positive and small negative slopes correspond to Rydberg states converging to the nearest ionic thresholds. The probability to capture the electron tends to be high for such states, diminishing however at high principal quantum numbers as n_c^{-3}. From Ref. [130].

resonance curves was much higher (factor 20-40). The main contribution to the high density of resonance curves was from the states with small principal quantum number corresponding to highly excited ionic channels. This increased significantly the probability of predissociation. In fact, in the case of HCO, the vibrating CO bond should also increase the density of steep resonance curves in Figs. 6.5 and 6.6. This is because if the vibration along CO is quantized, each of the curves shown in Fig. 3.5 will produce a series of additional ionic curves with different CO quanta. Therefore, the number of ionic potentials will be larger and, correspondingly, the density of resonance curves and avoided crossings in Figs. 6.5 and 6.6 will be increased too. This should increase the DR cross section (more states to be captured to) and the ratio P_d/P_{ion} (more avoided crossings).

Another approximation is that the $n = 2$ Rydberg states have dissociative character and are poorly described by this model. However, we believe that the dominant DR pathways are triggered by an initial capture into higher Rydberg states, rather than being directly captured into $n = 2$ states.

6.3.2 Comparison with our previous theoretical study

In our previous theoretical study of DR in HCO$^+$, published in Ref. [104], the Renner-Teller coupling was not taken into account because it appeared to have a small effect on the potential surfaces of excited molecular states of the HCO molecule. However, Renner-Teller coupling involves degenerate π states and therefore should play an important role in electron-ion scattering especially when $p\pi$ and $p\sigma$ molecular potentials approach closely to each other. Although Renner-Teller coupling was not included in the previous study, some nonadiabatic effects were considered there. The quantum

defects $\mu(\mathcal{Q})$ for $s\sigma, p\sigma, d\sigma$ states obtained from *ab initio* calculation demonstrate sharp variations at some configurations $\mathcal{Q}$ of the three HCO nuclei. Therefore, instead of using the three adiabatic defects $\mu(\mathcal{Q})$, a numerical diabatization procedure was applied to give a $\mathcal{Q}$-dependent 3x3 matrix $\mu^{(d)}(\mathcal{Q})$ of quantum defects. The $\mathcal{Q}$ dependence of the matrix is weaker and the matrix has more information about nonadiabatic effects than the diagonal matrix $\mu(\mathcal{Q})$. On the other hand the nonadiabatic effects represented by non-diagonal elements of $\mu(\mathcal{Q})$ might have a smaller effect on the dynamics of the electron compared to the nonadiabatic couplings involving degenerate π states. Indeed, the DR cross section obtained in the previous study [104] is much smaller than the cross section of the present treatment. To verify that the increase in the DR cross section is indeed due to the Renner-Teller coupling, we artificially set the non-diagonal elements in the Hamiltonian of Eq. 3.12 to zero and calculated again the cross section for $M = 0$. The resulting DR cross section is about a factor of three smaller than the cross section shown in Fig. 6.3 and on average it is close to the result of the previous study. It is worth mentioning that the calculation of Ref. [104] accounts for all three vibrational degrees of freedom but the very high vibrational levels that generate the steep Rydberg $n = 2$ curves in Fig. 6.5 (which have large widths and therefore lead to an increase in the capture probability) were omitted; these two effects would tend to balance each other, and might give roughly the same cross section as in the present study when off-diagonal couplings are switched off. We speculate that if the CO bond vibration was included in the present treatment the effect of the Renner-Teller coupling would likely be even more pronounced. To summarize our discussion of this point, we conclude that the Renner-Teller effect appears to be the most important nonadiabatic coupling in the dissociative recombination of HCO^+.

The theoretical cross section obtained in this study is inversely-proportional to the incident energy below 0.1 eV (see Fig. 6.3). Above 0.1 eV the cross section falls more rapidly with increasing energy. This is caused by the fact that at 0.1 eV an additional ionic channel becomes open. That ionic channel is responsible for the large probability to capture the electron. Above that ionization threshold, the density of Rydberg states (in which capture can occur) is much lower, as can be seen from Fig. 6.5, and therefore the capture probability drops. Moreover, resonance states above that ionization threshold have another competing decay channel for autoionization, which steals flux away from the DR observable. For the ground vibrational level $\{00^0 v_3\}$ (dot-dashed line in Fig. 6.3), that additional open channel is $\{01^1 v_3\}$, for the first excited level there are two nearby levels: $\{02^0 v_3\}$ and $\{02^2 v_3\}$. A similar behavior of the cross section was observed in DR of H_3^+ [94, 95]: the cross section drops down once a new ionic channel becomes open. The cross section from the previous theoretical study of HCO^+ (the solid line in Fig. 6.3) does not show that behavior. It behaves smoothly as the energy crosses the new ionization threshold. This is because the Renner-Teller effect was not accounted for: hence transitions of the type $\{00^0 v_3\} \longleftrightarrow \{01^1 v_3\}$ are forbidden by the different symmetries of those vibrational states.

Another difference with the previous study is the manner in which the final cross section is calculated. In Ref. [104], the scattering matrix $S_{i,i'}$ for electron-ion collisions was explicitly calculated, but only in the electron-ion subset of channel space with no channel indices explicitly referring to dissociation. All of the channels $|i\rangle$ are vibronic states. However, some of the channels $|i\rangle$ are open for dissociation, and as a result, the $S_{i,i'}$ matrix is not completely unitary. The defect from unitarity was used to calculate the dissociative flux and the corresponding DR cross section. The resulting cross section

from this method has a rich structure with many Rydberg series of resonances. The cross section was then averaged over an appropriate thermal distribution of electron energies. The averaged cross section still has a number of resonances that are not seen in the comparatively low resolution experiment. In the present paper we have employed a different averaging procedure, as was discussed above. This procedure gives a very smooth curve for the cross section.

6.4   Outlook

The framework we have developed for dissociative recombination reactions for small molecules is quite general and applicable to a wide variety of targets. It is definitely possible to improve upon these calculations, especially in the calculation of electronic parameters like Rydberg state potential energy surfaces and couplings. To this end we are currently working at calculating these quantities from R-matrix calculations, which will also allow a better understanding of the problem and avoid the ambiguities related to the choice of the model for the fit, which have plagued us at the beginning of the HCO^+ study.

Chapter 7

Summary

This thesis has dealt with the theoretical description of various chemical processes triggered by electrons in polyatomic molecules. As we have pointed out, the different reaction environments require different approaches. We have developed, in Ch. 2, a framework that, though approximate, enabled us to make inroads in the problem of scattering of an electron from a general polyatomic molecule in Ch. 4 and to give some insight on the problem of radiation damage to DNA (see Ch. 5), of interest to the biomedical community. In Chapters 4 and 5 we have shown how our approach is able to determine scattering observables for a wide variety of large polyatomic molecules, including CO_2, SF_6, the DNA bases, and tetrahydrofuran, many of which have not been tackled before by theory because they are so large.

In the part of this thesis that deals with dissociative recombination reactions, we have first developed a theoretical framework that is quite robust and able to deal with general small molecules in Ch. 3. Through the use of *ab initio* calculations, R-matrix methods, and then quantum defect theory (QDT) we deal with the vibronic interactions that arise in triatomics subject to conical intersections or Renner-Teller effect. This approach is then applied to DR of the molecular ion HCO^+ in Ch. 6 and the results are encouragingly close to available experimental data, although due to

the complication of including many degrees of freedom some have been frozen and the results can certainly be further improved.

Whenever possible we have given an outlook on the future developments that could arise from this work, for example on the description of high harmonic generation from molecules, which is well under way.

Bibliography

[1] Computer Physics Communications library. http://www.cpc.qub.ac.uk.

[2] H. Abdoul-Carime, M. A. Huels, F. Bruning, E. Illenberger, and L. Sanche. J. Chem. Phys., 113:2517, 2000.

[3] N. G. Adams and L. M. Babcock. Astrophys. J., 434:184, 1984.

[4] N. G. Adams, C. R. Herd, M. Geoghegan, D. Smith, A. Canosa, J. C. Gomet, B. R. Rowe, J. L. Queffelec, and M. Morlais. J. Chem. Phys., 94:4852, 1991.

[5] K. Aflatooni, G. A. Gallup, and P. D. Burrow. J. Phys. Chem. A, 102:6205, 1998.

[6] K. Aflatooni, A. Scheer, and P. D. Burrow. Phys. Rev. Lett., submitted, 2006.

[7] M. Allan and L. Andric. J. Chem. Phys., 105:3559, 1996.

[8] M. Allan and T. Skalicky. J. Phys. B, 36:3397, 2003.

[9] H. A. Jahn anad E. Teller. Proc. Roy. Soc. A, 161:220, 1937.

[10] A. Arthurs and A. Dalgarno. Proc. Roy. Soc. (London Ser.) A, 256:540, 1960.

[11] H. Bachau, E. Cormier, P. Decleva, J. E. Hansen, and F. Martin. Rep. Prog. Phys., 64:1815, 2001.

[12] N. R. Badnell and M. J. Seaton. J. Phys. B, 32:3955, 1999.

[13] S. Baker, J. S. Robinson, C. A. Haworth, H. Teng, R. A. Smith, C. C. Chirila, M. Lein, J. W. G. Tisch, and J. P. Marangos. Science, 312:424, 2006.

[14] R. Balog and E. Illenberger. Phys. Rev. Lett., 91:213201, 2003.

[15] K. L. Baluja, P. G. Burke, and L. A. Morgan. Comp. Phys. Comm., 27:299, 1982.

[16] J. N. Bardsley. J. Phys. B, 1:365, 1966.

[17] R. Barrios, P. Skurski, and J. Simons. J. Phys. Chem. B, 106:7991, 2002.

[18] D. R. Bates. J. Phys. B, 25:5479, 1992.

[19] K. J. Bathe. Finite Element Procedures. Prentice-Hall, Englewood Cliffs, N. J., 1996.

[20] I. B. Bersuker. Chem. Rev., 101:1067, 2001.

[21] Bioengineering Institute, The University of Auckland, New Zealand. Fem/bem notes, February 1997. http://www.bioeng.auckland.ac.nz/cmiss/fembemnotes/fembemnotes.pdf.

[22] G. M. Blackburn and M. J. Gait. Nucleic Acids In Chemistry And Biology. Oxford University Press, Oxford, 1996.

[23] D. Bouchiha, J. D. Gorfinkiel, L. G. Caron, and L. Sanche. J. Phys. B, 39:975, 2006.

[24] B. Boudaiffa, P. Cloutier, D. Hunting, M. A. Huels, and L. Sanche. Science, 287:1658, 2000.

[25] B. Boudaiffa, P. Cloutier, D. Hunting, M. A. Huels, and L. Sanche. Radiat. Res., 157:227, 2002.

[26] L. J. Bremner, M. G. Curtis, and l. C. Walker. J. Chem. Soc. Faraday Trans., 87:1049, 1991.

[27] J. P. Burke, Jr., C. H. Greene, and J. L. Bohn. Phys. Rev. Lett, 81:3355, 1998.

[28] Christian Buth, Robin Santra, and Lorenz S. Cederbaum. J. Chem. Phys., 119:7763, 2003.

[29] L. G. Caron and L. Sanche. Phys. Rev. Lett., 91:113201, 2003.

[30] CERN. Cernlib. http://wwwasd.web.cern.ch/wwwasd/cernlib/.

[31] D. M. Chase. Phys. Rev., 104:838, 1956.

[32] C. W. Clark. Phys. Rev. A, 16:1419, 1977.

[33] C. W. Clark. Phys. Rev. A, 20:1875, 1979.

[34] V. Cobut, Y. Fongillo, J. P. Patau, T. Goulet, M.-J. Fraser, and J.-P. Jay-Gerin. Radiat. Phys. Chem., 51:229243, 1998.

[35] R. Colle and A. Salvetti. J. Chem. Phys., 19:1404, 1983.

[36] P. B. Corkum. Phys. Rev. Lett., 71:1994, 1994.

[37] R. Curik and F. A. Gianturco. J. Phys, B, 35:717, 2002.

[38] M. Cek, M. Thoss, and W. Domcke. Phys. Rev. A, 70:125406, 2004.

[39] J. L. Dehmer. J. Chem. Phys., 54:4496, 1972.

[40] J. L. Dehmer. ACS Symposium Series, 263:139, 1984.

[41] D. Dill and J. L. Dehmer. J. Chem. Phys., 61:692, 1974.

[42] D. Dill and J. L. Dehmer. Phys. Rev. A, 21:85, 1980.

[43] O. Dolgounitcheva, V.G. Zakrzewski, and J.V. Ortiz. Chem. Phys. Lett., 307:220, 1999.

[44] T. H. Dunning. J. Chem. Phys., 90:1007, 1989.

[45] B. D. Esry, C. H. Greene, and J. P. Burke, Jr. Phys. Rev. Lett., 83:1751, 1999.

[46] I. I. Fabrikant and H. Hotop. Phys. Rev. Lett., 94:063201, 2005.

[47] U. Fano. J. Opt. Soc. Am., 65:979, 1975.

[48] U. Fano and C. M. Lee. Phys. Rev. Lett., 31:1573, 1973.

[49] S. Feuerbacher and R. Santra. J. Chem. Phys., 123:194310, 2005.

[50] S. Feuerbacher and R. Santra. private communication, 2005.

[51] S. Feuerbacher, T. Sommerfeld, R. Santra, and L. S. Cederbaum. J. Chem. Phys., 118:6188, 2003.

[52] G. A. Fiete and E. J. Heller. Rev. Mod. Phys., 75:933, 2003.

[53] A. I. Florescu-Mitchell and J. B. A. Mitchell. Phys. Rep., 430:277, 2006.

[54] A. F. Fuciarelli and J. D. Zimbrick, editors. Radiation Damage in DNA: Structure/Function Relationships at Early Times. Battelle, Columbus, OH, 1995.

[55] B. C. Garrett and D. A. Dixon. Chem. Rev., 105:355, 2005.

[56] W. D. Geppert. unpublished, 2005.

[57] W. D. Geppert, R. Thomas, A. Ehlerding, J. Semaniak, F. Osterdahl, M. af Ugglas, N. Djuric, A. Paald, and M. Larsson. Faraday Disc., 127:425, 2004.

[58] F. A. Gianturco and R. R. Lucchese. J. Chem. Phys., 108:6144, 1998.

[59] F. A. Gianturco and R. R. Lucchese. J. Chem. Phys., 114:3429, 2001.

[60] F. A. Gianturco and R. R. Lucchese. J. Chem. Phys., 120:7446, 2004.

[61] F. A. Gianturco, S. Meloni, P. Paioletti, R. R. Lucchese, and N. Sanna. J. Chem. Phys., 108:4002, 1998.

[62] F. A. Gianturco and J. A. Rodriguez-Ruiz. Phys. Rev. A, 47:1075, 1993.

[63] F. A. Gianturco and T. Stoecklin. J. Phys. B, 29:3933, 1996.

[64] J. C. Gibson, M. A. Green, K. W. Trantham, S. J. Buckman, P. J. O. Teubner, and M J Brunger. J. Phys. B, 32:213, 1999.

[65] A. Giusti. J. Phys. B, 13:3867, 1980.

[66] S. Gohlke, H. Abdoul-Carime, and E. Illenberger. Chem. Phys. Lett., 380:595, 2003.

[67] E. M. Goldfield, S. K. Gray, and L. B. Harding. J. Chem. Phys., 99:5812, 1993.

[68] G. H. Golub and C. F. Van Loan. Matrix Computation. Johns Hopkins University Press, Baltimore, MD, 1996.

[69] J. D. Gorfinkiel, L. A. Morgan, and J. Tennyson. J. Phys. B, 35:543, 2002.

[70] A. Grandi, F. A. Gianturco, and N. Sanna. Phys. Rev. Lett., 93:048103, 2004.

[71] A. A. Granovsky. PC GAMESS version 7.0. http://classic.chem.msu.su/gran/gamess/index.html.

[72] C. H. Greene. In J.S. Briggs, H. Kleinpoppen, and H.O. Lutz, editors, Fundamental Processes of Atomic Dynamics. Plenum, New York, 1988.

[73] C. H. Greene. private communication, 2005.

[74] C. H. Greene, M. Aymar, and E. Luc-Koenig. Rev. Mod. Phys., 68:1015, 1996.

[75] C. H. Greene, U. Fano, and G. Strinati. Phys. Rev. A, 19:1485, 1979.

[76] C. H. Greene and C. Jungen. Phys. Rev. Lett., 55:1066, 1985.

[77] C.H. Greene and C. Jungen. Adv. Atom. Mol. Phys., 21:51, 1985.

[78] J. Gu, Y. Xie, and H. F. Schaefer III. J. Am. Chem. Soc., 127:1053, 2005.

[79] S. L. Guberman and A. Giusti-Suzor. J. Chem. Phys., 95:2602, 1991.

[80] E. L. Hamilton and C. H. Greene. Phys. Rev. Lett., 89:263003, 2002.

[81] S. Hara. J. Phys. Soc. Jpn., 27:1009, 1969.

[82] N. A. Harris and C. Jungen. Phys. Rev. Lett., 70:2549, 1993.

[83] H.R.Drew, R.M.Wing, T.Takano, C.Broka, S.Tanaka, K.Itakura, and R.E.Dickerson. Proc.Natl.Acad.Sci.U.S.A., 78:2179, 1981.

[84] W. M. Huo and D. Brown. Phys. Rev. A, 60:295, 1999.

[85] W.M. Huo, M. A. P. Lima, T. L. Gibson, and V. McKoy. Phys. Rev. A, 36:1642, 1987.

[86] J. Itatani1, J. Levesque, D. Zeidler, H. Niikura, H. Pepin, J. C. Kieffer, P. B. Corkum, and D. M. Villeneuve. Nature, 432:867, 2004.

[87] J. Gilbert J. W. Demmel and X. S. Li. Superlu users' guide. Technical Report UCB/CSD-97-944, EECS Department, University of California, Berkeley, 1997.

[88] K. D. Jordan and F. Wang. Ann. Rev. Phys. Chem., 54:367, 2003.

[89] C. Jungen and S. C. Ross. Phys. Rev. A, 55:R2503, 1997.

[90] R. E. Kennerly. Phys. Rev. A, 21:1876, 1980.

[91] R. E. Kennerly, R. A. Bonham, and M. Mc Millan. J. Chem. Phys., 70:2039, 1979.

[92] M. Kimura, O. Sueoka, A. Hamada, and Y. Itikawa. Adv. Chem. Phys., 3:537, 2000.

[93] W. Kohn and L. J. Sham. Phys. Rev., 140:A1133, 1965.

[94] V. Kokoouline, B. D. Esry, and C. H. Greene. Nature, 412:891, 2001.

[95] V. Kokoouline and C. H. Greene. Phys. Rev. A, 68:012703, 2003.

[96] V. Kokoouline and C. H. Greene. J. Phys.: Confer. Ser., 4:74, 2005.

[97] V. Kokoouline and C. H. Greene. Phys. Rev. A, 72:022712, 2005.

[98] H. Koppel, W. Domcke, and L. S. Cederbaum. J. Chem. Phys., 74:2945, 1981.

[99] W. P. Kraemer and A. U. Hazi. In Molecular Astrophysics. State of Art and Future Directions. Proceedings of the NATO Advanced Research Workshop, page 575. 1985.

[100] W. P. Kraemer and A. U. Hazi. In Dissociative Recombination: Theory, Experiment and Applications, page 62. World Scientific, Singapore, 1988.

[101] L. D. Landau and E. M. Lifshitz. Quantum mechanics: non-relativistic theory. Butterworth Heinemann, Burlingto, MA, 2003.

[102] N. F. Lane. Rev. Mod. Phys., 52:29, 1980.

[103] C. M. Laperle, J. E. Mann, T. G. Clements, and R. E. Continetti. Phys. Rev. Lett., 93:153202, 2004.

[104] A. Larson, S. Tonzani, R. Santra, and C. H. Greene. J. Phys. Conf. Ser., 4:148, 2005.

[105] M. Larsson. In C. Y. Ng, editor, Photoionization and photodetachment, page 693. World Scientific, Singapore, 2000.

[106] S. Laube, A. Le Padellec, O. Sidko, C. Rebrion-Rowe, J. B. A. Mitchell, and B. R. Rowe. J. Phys. B, 31:2111, 1998.

[107] C. Lee, W. Yang, and R. G. Parr. Phys. Rev. B, 37:785, 1988.

[108] M. Lepage, S. Letarte, M. Michaud, F. Motte-Tollet, M.-J. Hubin-Franskin, D. Roy, and L. Sanche. J. Chem. Phys., 109:5980, 1998.

[109] H. LeRouzo and G. Raseev. Phys. Rev. A, 29:1214, 1984.

[110] M. T. Leu, M. A. Biondi, and R. Johnsen. Phys. Rev., 8:420, 1973.

[111] P.L. Levesque, M. Michaud, and L. Sanche. Nucl. Instr. and Meth. in Phys. Res. B, 225:230, 2003.

[112] H. J. Levinson, T. Gustafsson, and P. Soven. Phys. Rev. A, 19:1089, 1979.

[113] M. Lewenstein, Ph. Balcou, M. Yu. Ivanov, A. L'Huillier, and P. B. Corkum. Phys. Rev. A, 49:2117, 1994.

[114] S. G. Lias, R. D. Levin, and S. A. Kafafi. Ion energetics data. In P.J. Linstrom and W.G. Mallard, editors, NIST Chemistry WebBook, NIST Standard Reference Database Number 69. National Institute of Standards and Technology, Gaithersburg, MD, 2005. http://webbook.nist.gov.

[115] H. C. Longuet-Higgins. Advances in Spectroscopy, 2:429, 1961.

[116] D. Loomba, S. Wallace, D. Dill, and J. L. Dehmer. J. Chem. Phys., 75:4546, 1981.

[117] R. R. Lucchese, F. A. Gianturco, and N. Sanna. Chem. Phys. Lett., 305:413, 1999.

[118] R. R. Lucchese and V. McKoy. Phys. Rev. A, 25:1963, 1982.

[119] R. R. Lucchese and V. McKoy. Phys. Rev. A, 26:1406, 1982.

[120] M. G. Lynch, D. Dill, J. Siegel, and J. L. Dehmer. J. Chem. Phys., 71:4249, 1979.

[121] F. Martin, P. D. Burrow, Z. Cai, P. Cloutier, D. Hunting, and L. Sanche. Phys. Rev. Lett., 92:068101, 2004.

[122] E. E. Mayer and E. R. Grant. J. Chem. Phys., 103:10513, 1995.

[123] E. E. Mayer, H. G. Hedderich, and E. R. Grant. J. Chem. Phys., 108:1886, 1998.

[124] E. E. Mayer, H. G. Hedderich, and E. R. Grant. J. Chem. Phys., 108:8429, 1998.

[125] B. J. McCall and T. Oka. Science, 287:1941, 2000.

[126] C. W. McCurdy, W. A. Isaacs, H. D. Meyer, and T. N. Rescigno. Phys. Rev. A, 67:042708, 2003.

[127] N. P. Mehta, B. D. Esry, and C. H. Greene. unpublished, 2006.

[128] H. D. Meyer, S. Pal, and U. V. Riss. Phys. Rev. A, 46:186, 1992.

[129] K. W. Meyer, C. H. Greene, and B. D. Esry. Phys. Rev. Lett., 78:4902, 1997.

[130] I. A. Mikhailov, V. Kokoouline, A. Larson, S. Tonzani, and C. H. Greene. Phys. Rev. A, submitted, 2006.

[131] A. R. Milosavljevic, A. Giuliani, D. Sevic, M. J. Hubin-Franskin, and B. Marinkovic. Eur. Phys. J. D, 35:411, 2005.

[132] I. Mistrik, R. Reichle, U. Muller, H. Helm, M. Jungen, and J. A. Stephens. Phys. Rev. A, 61:033410, 2000.

[133] N. Moiseyev. Phys. Rep., 302:211, 1998.

[134] L. Morgan. Phys. Rev. Lett., 80:1873, 1998.

[135] L. A. Morgan, J. Tennyson, and C. J. Gillan. J. Phys. B, 30:4087, 1997.

[136] L. A. Morgan, J. Tennyson, and C. J. Gillan. Com. Phys. Comm., 114:120, 1998.

[137] M. Morrison, B.C. Saha, and T. L. Gibson. Phys. Rev. A, 36:3682, 1987.

[138] M. A. Morrison, N. F. Lane, and L. A. Collins. Phys. Rev. A, 15:2186, 1977.

[139] M.A. Morrison and L. A. Collins. Phys. Rev. A, 17:918, 1978.

[140] P. Mozejko and L. Sanche. Radiat. Environ. Bioohys., 42:201, 2003.

[141] V. Ngassam, A. Florescu, L. Pichl, I.F. Schneider, O. Motapon, and A. Suzor-Weiner. Eur. Phys. J. D, 26:165, 2003.

[142] T. F. O'Malley. Phys. Rev., 150:14, 1966.

[143] A. E. Orel and K. C. Kulander. Phys. Rev. Lett., 71:4315, 1993.

[144] A. Le Padellec, C. Sheehan, D. Talbi, and J. B. A. Mitchell. J. Phys. B, 30:319, 1997.

[145] R. Panajotovic, M. Kitajima, H. Tanaka, M. Jelisavcic, J. Lower, L. Campbell, M. J. Brunger, and S. J. Buckman. J. Phys. B, 36:1615, 2003.

[146] J. M. Papanikolas, V. Vorsa, M. E. Nadal, P. J. Campagnola, J. R. Gord, and W. C. Lineberger. J. Chem. Phys., 97:7002, 1992.

[147] G. A. Parker and R. T. Pack. J. Chem. Phys., 68:1585, 1978.

[148] R. G. Parr and W. Yang. Density Functional Theory of Atoms and Molecules. Oxford University Press, Oxford, 1989.

[149] K. Pfingst, H. T. Thummel, and S. D. Peyerimoff. J. Phys. B, 25:2107, 1992.

[150] J. A. Pople et al. GAUSSIAN98. Pittsburgh, 1998. http://www.gaussian.com.

[151] G. H. Press, B. P. Flannery, S. A. Teukolsky, and W. T. Vetterling. Numerical Recipes in Fortran. Cambridge University Press, Cambridge, 1995.

[152] S. Ptasinska, S. Denifl, S. Gohlke, P. Scheier, E. Illenberger, and T. D. Mark. Ang. Chem. Int. Ed., 45:1893, 2006.

[153] S. Ptasinska, S. Denifl, P. Scheier, and T. D. Mark. J. Chem. Phys., 120:8505, 2004.

[154] C. Puzzarini, R. Tarroni, P. Palmieri, S. Carter, and L. Dore. Mol. Phys., 87:879, 1996.

[155] R. Renner. Z. Phys., 92:172, 1934.

[156] T. N. Rescigno, D. A. Byrum, W. A. Isaacs, and C. W. McCurdy. Phys. Rev. A, 60:2186, 1999.

[157] J. D. Robinson and R. J. Foltynowiczand E. R. Grant. J. Chem. Phys., 112:1701, 2000.

[158] B. R. Rowe, J. C. Gomet, A. Canosa, C. Rebrion, and J. B. A. Mitchell. J. Chem. Phys., 96:1105, 1992.

[159] L. Sanche. Mass. Spectrom. Rev., 21:349, 2002.

[160] R. Santra and L. S. Cederbaum. Phys. Rep., 368:1, 2002.

[161] R. Santra and L. S. Cederbaum. Phys. Rep., 368:1, 2002.

[162] R. Santra, J. M. Shainline, and C. H. Greene. Phys. Rev. A, 71:032703, 2005.

[163] B. K. Sarpal and J. Tennyson. J. Phys. B, 25:L49, 1992.

[164] A.M. Scheer, K. Aflatooni, G. A. Gallup, and P. D. Burrow. Phys. Rev. Lett., 92:068102, 2004.

[165] L. I. Schiff. Quantum mechanics. McGraw-Hill, 1968.

[166] B. I. Schneider and T. N. Rescigno. Phys. Rev. A, 37:3749, 1988.

[167] B. I. Schneider, T. N. Rescigno, B. H. Lengsfield, and C. W. McCurdy. Phys. Rev. Lett., 66:2728, 1991.

[168] Scientific Computing Group, University of Basel. Pardiso. http://www.computational.unibas.ch/cs/scicomp/software/pardiso/.

[169] M. J. Seaton. Rep. Prog. Phys., 46:167, 1983.

[170] M. J. Seaton. Comp. Phys. Comm., 146:225, 2002.

[171] T. C. Shen, C. Wang, G. C. Abeln, J. R. Tucker, J. W. Lyding, P. Avouris, and R. E. Walkup. Science, 268:1590, 1995.

[172] J. Shertzer and J. Botero. Phys. Rev. A, 49:3673, 1994.

[173] J. C. Slater. Quantum Theory of Molecules and Solids, volume IV. McGraw-Hill, New York, 1974.

[174] F. T. Smith. Phys. Rev., 118:349, 1960.

[175] E. Snyder. unpublished, 2004.

[176] T. Sommerfeld. J. Phys. Chem. A, 108:9150, 2004.

[177] T. Sommerfeld and T. Posset. J. Chem. Phys,, 119:7714, 2003.

[178] O. Sueoka, C. Makochekanwa, H. Tanino, and M. Kimura. Phys. Rev. A, 72:042705, 2005.

[179] O. Sueoka and S. Mori. J. Phys. B, 19:4035, 1986.

[180] J. Q. Sun and C. D. Lin. Phys. Rev. A, 46:5489, 1992.

[181] A. Szabo and N. S. Ostlund. Modern Quantum Chemistry. Dover, Mineola, NY, 1996.

[182] C. Szmytkowski, A. Zecca, G. Karwasz, S. Oss, K. Maciag, B. Marinkovic, R. S. Brusa, and R. Grisenti. J. Phys. B, 20:5817, 1987.

[183] H. Takagi. In S. L. Guberman, editor, Dissociative Recombination of Molecular Ions With electrons, page 177. Kluwer Academic / Plenum Publishers, New York, 2003.

[184] D. Talbi, F. Pauzat, and Y. Ellinger. Chem. Phys., 126:291, 1988.

[185] K. Tanaka and E. R. Davidson. J. Chem. Phys., 70:2904, 1978.

[186] M. Tashiro and S. Kato. J. Chem. Phys., 117:2053, 2002.

[187] J. Tennyson, C. J. Noble, and S. Salvini. J. Phys. B, 17:905, 1984.

[188] J. Tennyson and B. T. Sutcliffe. J. Chem. Phys., 77:4061, 1982.

[189] O. I. Tolstikhin, V. N. Ostrovsky, and H. Nakamura. Phys. Rev. Lett., 79:2026, 1997.

[190] O. I. Tolstikhin, V. N. Ostrovsky, and H. Nakamura. Phys. Rev. A, 58:2077, 1998.

[191] S. Tonzani. Comp. Phys. Comm., submitted, 2006.

[192] S. Tonzani and C. H. Greene. J. Chem. Phys., 122:014111, 2005.

[193] S. Tonzani and C. H. Greene. unpublished, 2005.

[194] S. Tonzani and C. H. Greene. J. Chem. Phys., 124:054312, 2006.

[195] S. Tonzani and C. H. Greene. J. Chem. Phys., submitted.

[196] C. S. Trevisan, A. E. Orel, and T. N. Rescigno. J. Phys. B, 39:L255, 2006.

[197] V. Vorsa, S. Nandi, P. J. Campagnola, M. Larsson, and W. C. Lineberger. J. Chem. Phys., 106:1402, 1996.

[198] A. Wasserman, N. T. Maitra, and K. Burke. J. Chem. Phys., 122:144103, 2005.

[199] S. Watanabe and C. H. Greene. Phys. Rev. A, 22:158, 1980.

[200] D. K. Watson, R. R. Lucchese, V. McKoy, and T. N. Rescigno. Phys. Rev. A, 21:738, 1980.

[201] C. A. Weatherford, M. Dong, and B. C. Saha. Int. J. Quant. Chem., 65:591, 1997.

[202] C. A. Weatherford and A. Temkin. Phys. Rev. A, 49:2580, 1994.

[203] H. J. Werner, P. J. Knowles, R. Lindh, M. Schutz, et al. MOLPRO, a package of ab initio programs. Birmingham, UK, 2003. http://www.molpro.net.

[204] R. Wester, U. Hechtfischer, L. Knoll, M. Lange, J. Levin, M. Scheffel, D. Schwalm, A. Wolf, A. Baer, Z. Vager, D. Zajfman, M. Mladenovic, and S. Schmatz. J. Chem. Phys., 116:7000, 2002.

[205] C. Winstead, P.G. Hipes, M. A. P. Lima, and V. McKoy. J. Chem. Phys., 94:5455, 1991.

[206] C. Winstead and V. McKoy. Phys. Rev. A, 73:012711, 2006.

[207] L. Yang, H. Agren, V. Carravetta, O. Vahtras, L. Karlsson, B. Wannberg, D. M. P. Holland, and M. A. McDonald. J. Electr. Spectr., 94:163, 1998.

[208] D. R. Yarkony. Rev. Mod. Phys., 68:985, 1996.

[209] A. Zecca, C. Perazzolli, and M. J. Brunger. J. Phys. B, 38:2079, 2005.

[210] Y. Zheng, P. Cloutier, D. J. Hunting, J. R. Wagner, and L. Sanche. J. Chem. Phys., 124:064710, 2006.

[211] E. J. Zuckerman, E. E. Mayer, R. J. Foltynowicz, J. D. Robinson, S. H. Jen, M. C. Konopk, T. Sanford, H. G. Hedderich, I-C. Chen, and E. R. Grant. J. Chem. Phys., 113:5372, 2000.

Finite element matrices

Starting from Eq. 2.8 we define the matrices Γ and Λ in our finite element basis by transforming first to spherical coordinates (the box is spherical and the grid is also defined in spherical coordinates), and then to rescaled coordinates, which are the variables of the local polynomials. In the rescaled variables each sector is transformed to a cube, in which the range of each variable is from 0 to 1. The basis set is composed of cubic Hermite polynomials in each dimension. In the rescaled coordinates system they are:

$$\psi_1^0(\xi) = 1 - 3\xi^2 + 2\xi^3 \tag{A.1}$$

$$\psi_2^0(\xi) = \xi(\xi - 1)^2 \tag{A.2}$$

$$\psi_1^1(\xi) = \xi^2(3 - 2\xi) \tag{A.3}$$

$$\psi_2^1(\xi) = \xi^2(\xi - 1). \tag{A.4}$$

The wavefunction inside each sector can therefore be expanded as

$$u(\xi_1, \xi_2, \xi_3) = \sum_{i,j,k,l,m,n} \psi_i^l(\xi_1)\psi_j^m(\xi_2)\psi_k^n(\xi_3)C_{node}^{(lmn)} \tag{A.5}$$

where i, j, k can be 1 if the polynomial has nonzero value at some node or 2 if it has nonzero derivative, whereas l, m, n can assume values of 0 if that node is the first for
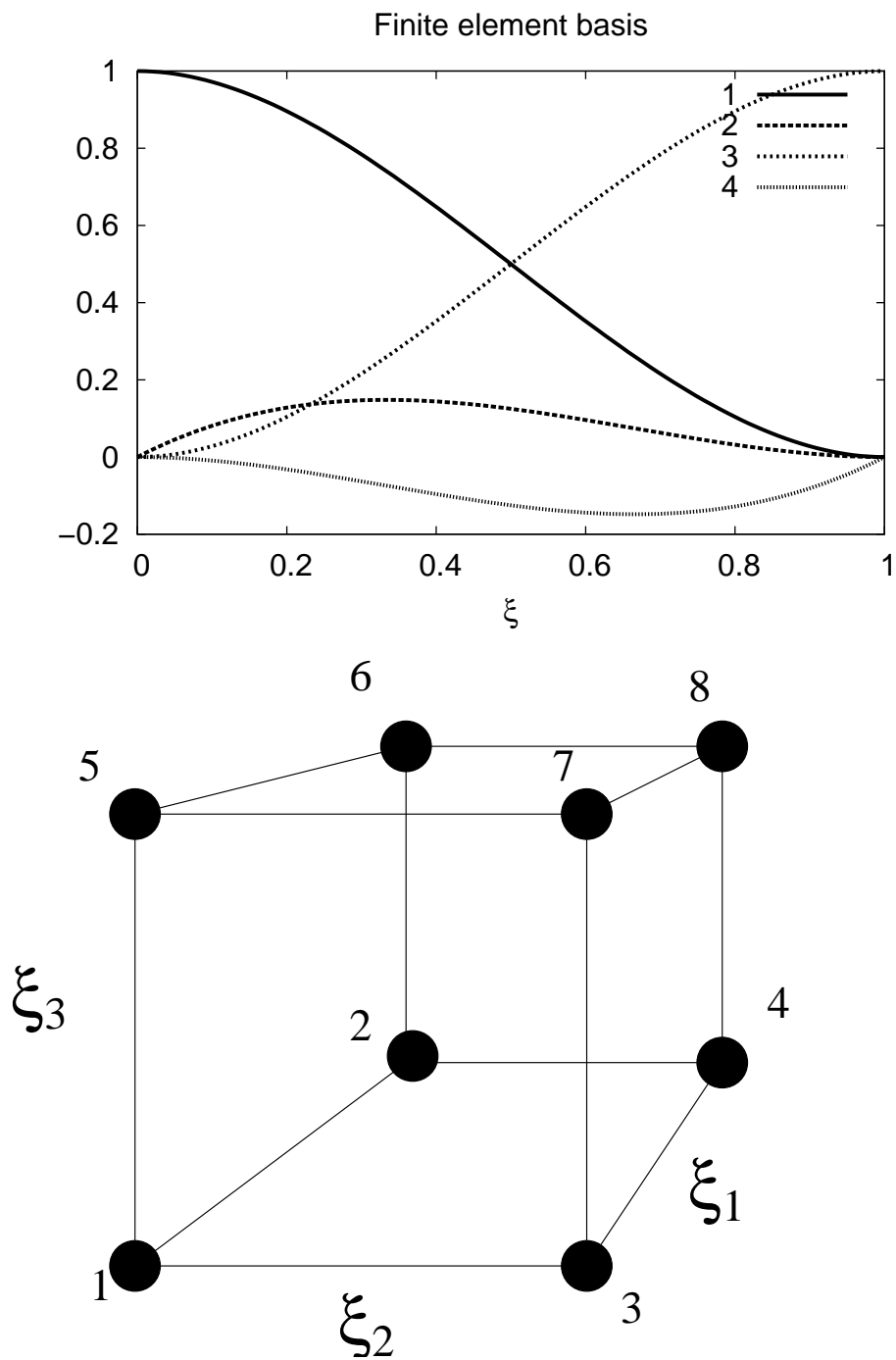
Figure A.1: Top: finite element basis functions from Eqs. A.1-A.4, the four polynomials are plotted in the same order as in the text. Bottom: nodal structure for one cubic sector in the rescaled variables.

the variable of the polynomial in the sector or 1 if it is the last; ξ_i are the local rescaled variables . The nodal structure of each element is represented in Fig. A.1, together with the basis functions. The coefficients $C_{node}^{(lmn)}$ are the values of the wavefunction and its derivatives at the node, and they are to be determined solving Eq. 2.8. If we define

$$a_{k,p} = x_{k,p,i+1} - x_{k,p,i} \tag{A.6}$$

$$x_{k,p} = a_{k,p}\,\xi_k + x_{k,p,i} \tag{A.7}$$

where k indexes the spherical coordinates and p the sectors in which they are defined, $x_{k,p,i}$ and $x_{k,p,i+1}$ are the initial and final points for the variable x_k in sector p, the expressions for the matrices become:

$$\Gamma_{ij} = \int \left[\sum_{k=1}^{3} \frac{F(x_k)}{a_k a_k} \frac{\partial u_i}{\partial \xi_k} \frac{\partial u_j}{\partial \xi_k} + 2u_i(U - E)u_j \right] a_r a_\theta a_\phi r^2 \sin^2\theta d\xi_1 d\xi_2 d\xi_3 \tag{A.8}$$

$$\Lambda_{mn} = \int Y_{lm}^*(\theta, \phi) Y_{l'm'}(\theta, \phi) \sin\theta \, d\theta \, d\phi = \delta_{ll'}\delta_{mm'} \tag{A.9}$$

where $F(x_k)$ is a spherical coordinates scale factor, and it is 1 if $x_k = r$ and $1/r^2$ and $1/(r^2 \sin^2\theta)$ for θ and ϕ respectively. Imposing function and derivative continuity for $u(\xi_1, \xi_2, \xi_3)$ amounts to require that the indices of the same node across neighboring sectors be the same. This in turn leads to having to perform a sum of the integrals in Eq. A.8 when evaluating the matrix element at a node, across all sectors that share that node. The continuity conditions we apply are very similar to the ones in Eqs. 1.16, 1.18 of Ref. [21], but adapted to a three dimensional case.

Appendix B

Related publications

- "Electron-molecule scattering calculations in a 3D finite element R-matrix approach" S. Tonzani and C. H. Greene, J. Chem. Phys., 122, 014111 (2005)

- "Dissociative recombination of HCO^+" . Larsson, S. Tonzani, R. Santra and C. H. Greene, J. Phys. Conference Series, 4, 148 (2005)

- "Low energy electron scattering from DNA and RNA bases: shape resonances and radiation damage" S. Tonzani and C. H. Greene, J. Chem. Phys., 124, 054312 (2006) and Virtual Journal of Biological Research 11 (4) (2006)

- "Renner-Teller effects in HCO^+ dissociative recombination" I. Mikhaylov, V. Kokoouline, A. Larson, S. Tonzani and C. H. Greene, Phys. Rev. A, 74, 032707 (2006).

- "FERM3D: A finite element R-matrix electron molecule scattering code" S. Tonzani, Computer Physics Communications (in press).

- "Radiation damage to DNA: electron scattering from the backbone subunits" S. Tonzani and C. H. Greene, J. Chem. Phys., 125, 094504 (2006)